Ph.D. DISSERTATION

Tailoring catalytic activities of nanostructured catalysts on silicon for solar fuels production

By

Changyeon Kim

August 2021

SEOUL NATIONAL UNIVERSITY

COLLEGE OF ENGINEERING

DEPARTMENT OF MATERIALS SCIENCE AND ENGINEERING

Tailoring catalytic activities of nanostructured catalysts on silicon for solar fuels production

Advisor: Prof. Ho Won Jang

By

Changyeon Kim

A thesis submitted to the Graduate Faculty of Seoul National University in partial fulfillment of the requirements for the Degree of Doctor of Philosophy

Department of Materials Science and Engineering

August 2021

Approved

By

Chairman of Advisory Committee: Jin Young Kim

Vise-Advisory Committee: Ho Won Jang

Advisory Committee: Jeong-Yun Sun

Advisory Committee: Soo Young Kim

Advisory Committee: Sang Hyun Ahn

Abstract

As global energy consumption increases, various environmental issues, such as climate change, and ocean acidification, due to excessive use of fossil fuels have been raised. In this situation, the development of renewable and sustainable energy production is one of the most pressing challenges today, as the transition from a fossil fuel-based energy society to a clean energy society is essential. In this regard, solar fuel production, which converts inexhaustible solar energy to chemical energy, is a promising candidate for clean energy society. Solar fuel production has been attracting a lot of attention because it is eco-friendly method using solar energy to produce hydrogen fuel through water decomposition, or carbon-based fuel through CO_2 conversion. Since this process occurs through a photoelectrochemical reaction at photoelectrodes using semiconductor materials, there have been numerous study on photoelectrodes for efficient solar fuel production. Among the various candidate semiconducting materials, silicon is well known as a promising material for photoelectrodes, because of its beneficial properties for utilization of solar energy; narrow bandgap of 1.12 eV which is well mated to the solar spectrum, long carrier diffusion length, and earth-abundance. However, silicon has some limitations that are poor kinetic and catalytic activity for photoelectrochemical reaction, and low stability when contacts to electrolyte in a photoelectrochemical system. For efficient solar fuel production, it is essential to fabricate silicon photocathodes with these limitations improved.

.

This thesis contains various engineering strategies to utilize silicon for photocathode in solar fuel production. The silicon photoelectrodes are fabricated and studied by applying engineering strategies with nanostructured catalysts suitable for solar fuel production methods of solar water splitting for hydrogen fuel production and CO_2 conversion for carbon-based fuel production. Firstly, in chapter 1, the principles of solar water splitting and CO_2 conversion are described. To design the efficient photocathode, it is essential to understand the principles of photoelectrochemical reactions.

In chapter 2, silicon photocathodes with 3D/2D nanostructured transition metal sulfides catalysts for solar water splitting are demonstrated. Nanostructured transition metal sulfides are candidates for hydrogen evolution reaction in solar water splitting, because they have an inherently large surface to volume ratios and catalytic active edge sites. In transition metal sulfides, MoS_2 are widely studied because it exhibits the highest catalytic activity at edge sites. To maximize exposed edge sites of MoS_2, the 2D vertically aligned MoS_2 thin films are synthesized in this study. Furthermore, 3D Ni-Fe sulfides nanoparticles found as catalytic active materials from DFT calculations are decorated on the vertically aligned MoS_2 thin film catalysts. It is because catalytic activity for hydrogen evolution reaction is enhanced at MoS_2/Ni-Fe sulfides interface than that on MoS_2. The transferable 2D/3D transition metal sulfide heterostructure thin film catalysts are synthesized via one-step sulfurization process on thin film metal precursors using chemical vapor deposition. Then the thin film catalysts are transferred onto silicon photocathode and performance for photoelectrochemical hydrogen evolution reaction is measured. The synthesized thin film catalyst on silicon photocathode

exhibits remarkable performance: high photocurrent density (25.44 mA cm^{-2} at -0 V vs. RHE), lower onset potential (280 mV at 1.0 mA cm^{-2}), and long-term stability (over 10 h). The improvement of photoelectrochemical properties of synthesized photocathodes is attributed to its electrochemically-benign band bending, which is revealed from spectroscopic analysis, by the introduction of Ni-Fe sulfides nanoparticles. It facilitates efficient charge transport and inhibits the charge accumulation at electrolyte interfaces. This study provides promising strategies in developing high performance TMD-based electrocatalysts for practical applications in a wide variety of photoelectrochemical energy conversion processes.

In chapter 3, silicon photocathodes with 3D nanostructured silver catalysts for CO_2 utilization are demonstrated. In the CO_2 reduction reaction, product selectivity is very important, because various products can be produced, such as CO, HCOOH, CH_4, through CO_2 reduction reactions. Therefore, it is essential to select a catalyst that can selectively produce a desired product. Most of the studies on electrocatalysts for electrochemical CO_2 reduction reaction is focused on metal catalysts. Among various metal catalysts, silver catalysts are well known to promote the electrochemical reduction reaction of CO_2 to CO. To maximize the catalytic activity of silver catalysts for CO_2 reduction reaction, nanostructuring strategies are performed on silver catalysts. Through an electrochemical oxidation-reduction process, Ag catalysts are turned into nanostructured Ag catalysts with tuned morphology, active sites, and electronic structure. However, because Ag catalysts decorated on silicon photocathode inhibit the light absorption onto silicon photocathode, an appropriate structure for photocathode design is needed. In this study, a novel structure for photocathode using SiO_2 patterning is proposed for

photoelectrochemical CO_2 reduction on silicon photocathodes. The synthesized photocathode with the novel photocathode structure exhibits a low onset-potential of -0.16 V vs. RHE, a large saturated photocurrent density of -9 mA/cm^2 at -1.23 V vs. RHE, and faradaic efficiency for CO of 47 % at -0.6 V vs. RHE. This photocathode can produce syngas in the ratio from 1:1 to 1:3, which is an appropriate proportion for practical application. This work presents a new approach for designing photocathodes with a balanced catalytic activity and light absorption to improve the photoelectrochemical application for not only CO_2 reduction reactions, but also water splitting or N_2 reduction reactions.

Keywords: Solar fuel production, Water splitting, CO_2 utilization, Photoelectrochemical, Silicon photocathode, Nanostructured catalysts

Student Number: 2016-23688

Changyeon Kim

Table of Contents

List of Figures

List of Tables

Chapter 1

1.1. Introduction

Since the industrial revolution in the 19th century, mankind has been using fossil fuels as the main energy source and has achieved explosive industrial developments through this vast energy source. With this explosive development, energy consumption has also increased exponentially. Global energy consumption, which has been gradually increasing, reached about 600 EJ per year in 2019.[1] As shown in Figure 1.1, fossil fuels including oil, natural gas, and coal account for more than 80% of this energy consumption. Fossil fuels have made it possible to use so much energy, but now, such excessive use of fossil fuels has caused many environmental problems. Fossil fuels emit CO_2 as they combust, consequently, the concentration of CO_2 in the atmosphere is increasing due to the excessive use of fossil fuels, as depicted in Figure 1.2(a). CO_2 is one of the greenhouse gases and have been considered a majority contributor to the global warming and climate change.[2, 3] In addition, fossil fuels emit more than just CO_2 when burned. Harmful chemicals like sulfur dioxide and nitrogen oxide are also released, causing many environmental problems such as air pollution and ocean acidification. To solve these environmental issues, numerous researches have focused on the development of renewable and sustainable energy to replace fossil fuels. The most attractive method for renewable and sustainable energy is solar fuel production, which is sunlight-to-chemical energy conversion.[4-6] Solar fuel production, also called artificial photosynthesis, can be realized by the photoelectrochemical (PEC) reduction of water to hydrogen fuels (solar water splitting) or CO_2 to useful hydrocarbons (CO_2 utilization).[7-8]

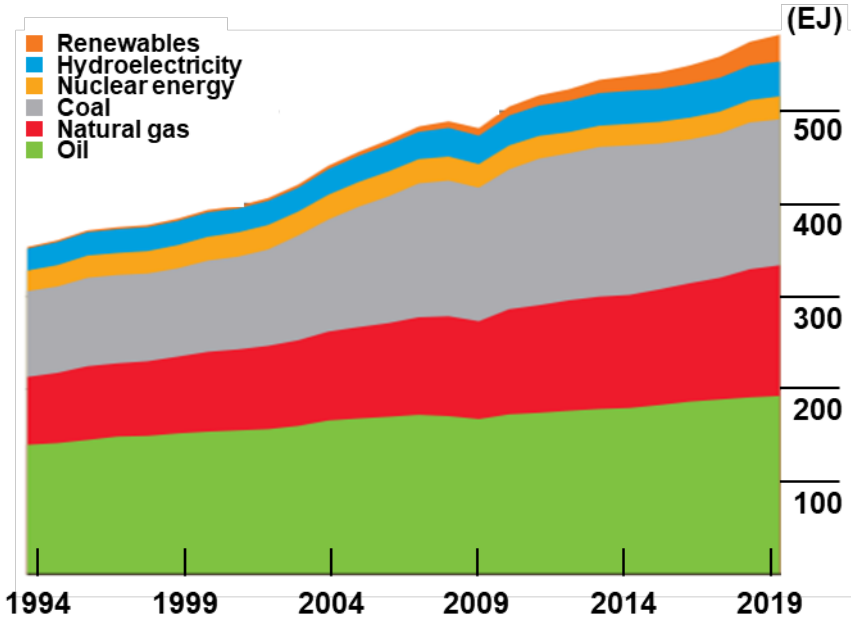

Figure 1.1 Primary energy consumption over the world.[1]

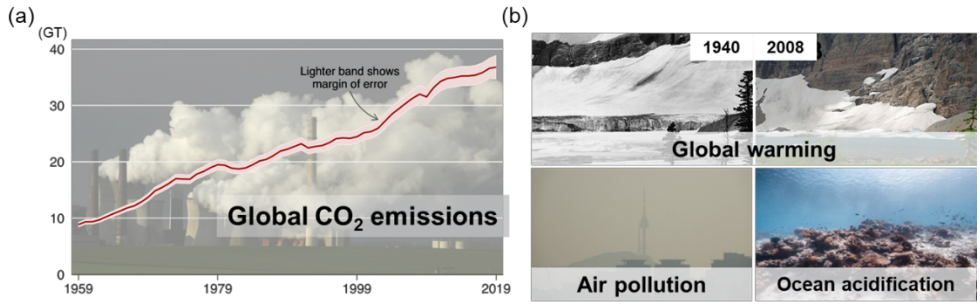

Figure 1.2 (a) Global CO_2 emissions. (b) environmental issues caused by the use of fossil fuels.

1.2. Solar water splitting

1.2.1. Solar water splitting

For researches to develop a renewable and sustainable energy source, hydrogen fuel has received a lot of attention since it is clean energy source when it combusts generates no carbon-based by-products. Also, hydrogen has a high energy density of 142 kJ/g, which is higher than fossil fuels.[9] Because of these advantages, hydrogen fuel is emerging as a next-generation energy source. However, the most used method for producing hydrogen fuel currently is the steam reforming process, which uses steam on fossil fuels.[10] Steam reforming process consumes massive amounts of fossil fuels, and emits a corresponding amount of CO_2. Therefore, it is essential to develop an eco-friendly way to produce hydrogen. In this respect, solar water splitting is the most attractive method for eco-friendly hydrogen fuel production, which can convert solar energy into storable hydrogen fuel without CO_2 emission.

1.2.2. Basics of solar water splitting

Photoelectrochemical cells for solar water splitting consists of three main components: photocathode(cathode), photoanode(anode), and electrolyte. Hydrogen is generated at the photocathode through proton reduction reaction, which is hydrogen evolution reaction (HER). On the other side, oxidation reaction, called oxygen evolution reaction, occurs at the photoanode, evolving oxygen. Schematic diagram of solar water splitting is shown in Figure 1.3. At least one of the electrodes must be a semiconductor for absorbing sunlight. The Gibbs free energy change (ΔG) for conversion of one molecule of H_2O into H_2 and O_2 under standard conditions, is 237.2 kJ/mol, and corresponds to $\Delta E^0 = 1.23$ V per electron transferred according to the Nernst equation. The overall water reaction can be expressed as follows:

Hydrogen evolution reaction (HER): $2\ H^+ + 2\ e^- \rightarrow H_2$

Oxygen evolution reaction (OER): $H_2O + 2\ h^+ \rightarrow 1/2\ O_2(g) + 2\ H^+$

Overall water splitting: $H_2O \rightarrow H_2(g) + 1/2\ O_2(g)$

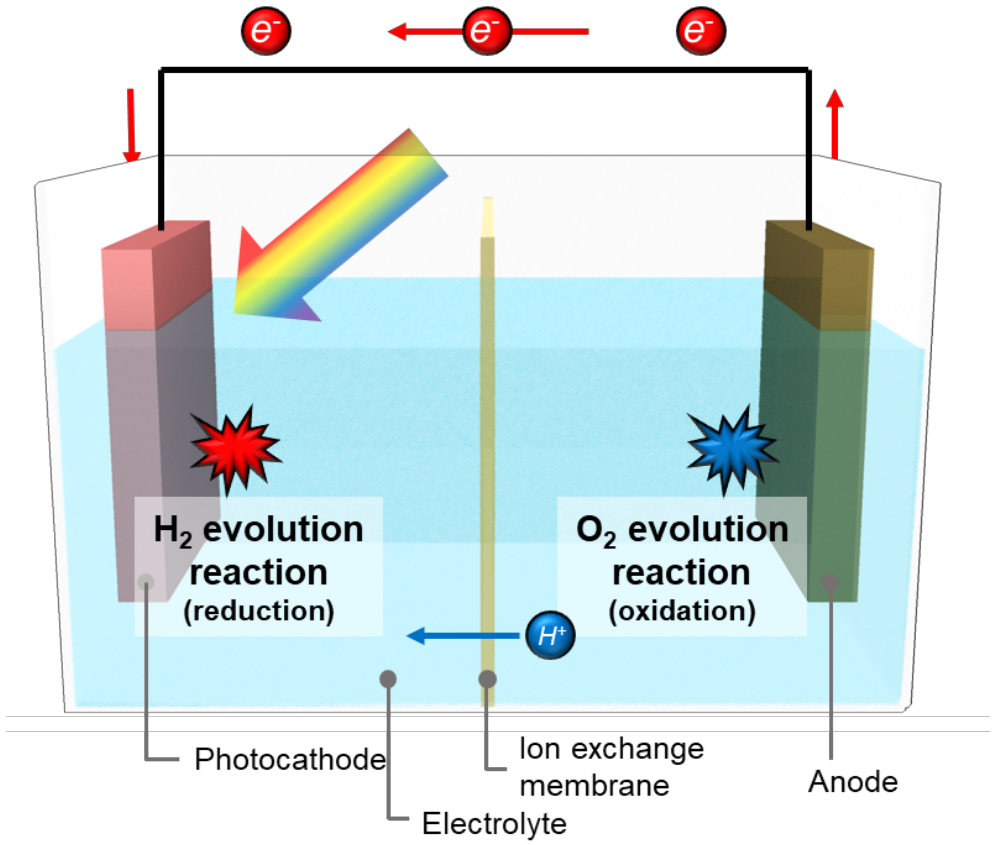

Figure 1.3. Schematic diagram of solar water splitting

1.3. CO_2 utilization

1.3.1. photoelectrochemical CO_2 reduction

The production of renewable and sustainable hydrogen fuel from water is attractive in terms of minimizing environmental crisis. Not only solar water splitting, but CO_2 utilization is also the most promising approach for resolving energy crisis. CO_2 utilization can store renewable energy, such as solar energy, as chemicals and fuels, by converting renewable energy to electronic energy and then on to chemical energy as shown in Figure 1.4. This can be realized through photoelectrochemical (PEC) CO_2 reduction, which could produce valuable fuels (alcohols or hydrocarbons) and fuel precursors for industrial process from CO_2 and water. Two major aspects of CO_2 utilization are to reduce the atmospheric CO_2 and to generate fuels from renewable and sustainable energy source.

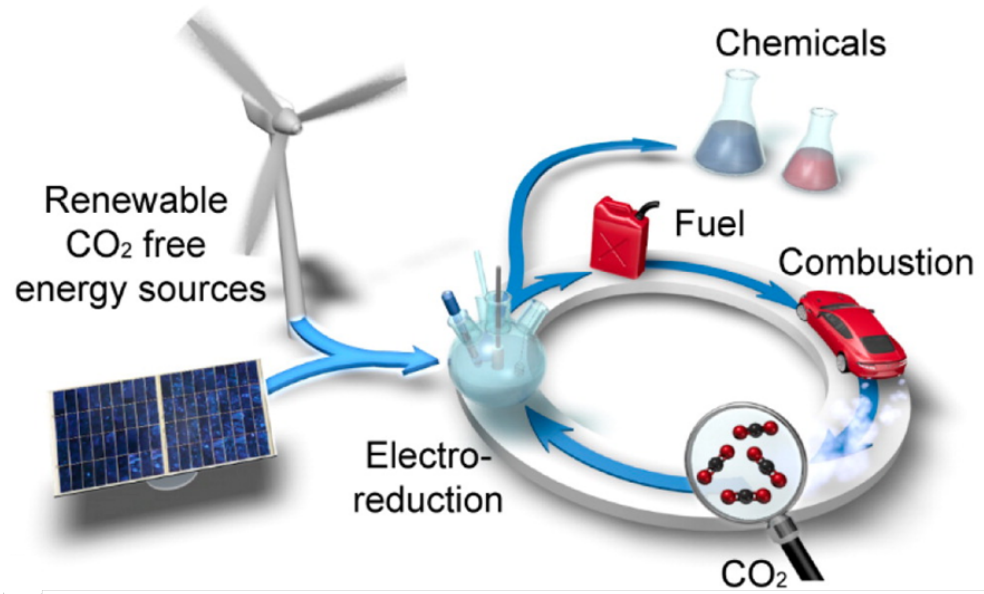

Figure 1.4. CO_2 utilization using renewable energy sources.[11]

1.3.2. Basics of PEC CO_2 reduction

Photoelectrochemical cells for PEC CO_2 reduction is very similar to that for solar water splitting. The three main components of cathode, anode, and electrolyte also used in PEC CO_2 reduction. However, different from solar water splitting, the reduction reaction occurring at the cathode is a CO_2 reduction reaction, not a hydrogen evolution reaction. The corresponding oxidation half-reaction is OER, as in the case of water splitting. When CO_2 is reduced, many products, such as carbon monoxide, formic acid, and methane, can be produced through CO_2 reduction reaction. Table 1.1 shows the formal redox potentials (E^0) for various CO_2 reduction reaction that is obtained from thermodynamic data.[12] All potentials are referenced to the standard hydrogen electrode (SHE). Because CO_2 can be reduced into the various form of products, the selective production to target product is very essential in CO_2 reduction reaction.

Table 1.1. Formal electrochemical redox potentials for the reduction of CO_2 and related compounds in aqueous media

Reaction	*E^0 vs. SHE (V)*
$CO_2 + e^- \rightarrow CO_2^{\bullet-}$	-1.85
$CO_2 + H_2O + 2\ e^- \rightarrow HCOO^- + OH^-$	-0.665
$CO_2 + H_2O + 2\ e^- \rightarrow CO + 2\ OH^-$	-0.521
$CO_2 + H_2O + 2\ e^- \rightarrow CH_3OH + 6\ OH^-$	-0.399
$CO_2 + H_2O + 2\ e^- \rightarrow CH_4 + 8\ OH^-$	-0.246
$H_2O + 2\ e^- \rightarrow H_2 + 2\ OH^-$	-0.414

1.4. Photocathode for solar fuel production

When conducting research for efficient photoelectrode design, generally, the photocathode and photoanode are each studied separately as a half-cell system. In half cell system, if photocathode is studied, anode material is used a conductive material having high catalytic activity and stability for oxidation reaction to judge the PEC performance of a fabricated photocathode. This thesis focuses on the reduction reaction (hydrogen evolution reaction and CO_2 reduction reaction) so, materials used as photocathode are designed.

1.4.1. Semiconductor/liquid junction

For designing materials for photocathode, semiconductor materials must be used because photocathode should absorb UV or visible light radiation from sunlight. Specifically, p-type semiconducting materials should be used for photocathode. It can be explained by the semiconductor/liquid junction, shown in Figure 1.5.

Once the p-type photocathode contact to electrolyte, the major carriers, holes, flow from the photocathode to the electrolyte, causing an electric field in the photocathode near the interface until equilibrium. At equilibrium state, the depletion region is formed, and the band of the p-type semiconductor bends downward. This band bending facilitates transportation of electron to the photocathode/electrolyte interface. When illuminated on the photocathode, electron-hole pairs generated, and the electrons can be transported toward the

interface due to the formed band bending. Then, reduction reactions can occur at the photocathode/electrolyte interface.

Likewise, in the case of n-type semiconductors, in which the major carrier is the electron, oppositely, upward band bending is formed. Therefore, the minor carrier, hole, generates oxidation reaction at electrode/electrolyte interface. Because of this phenomenon, in order to study a photocathode in which a reduction reaction occurs, p-type semiconductors should be used as photocathode materials.

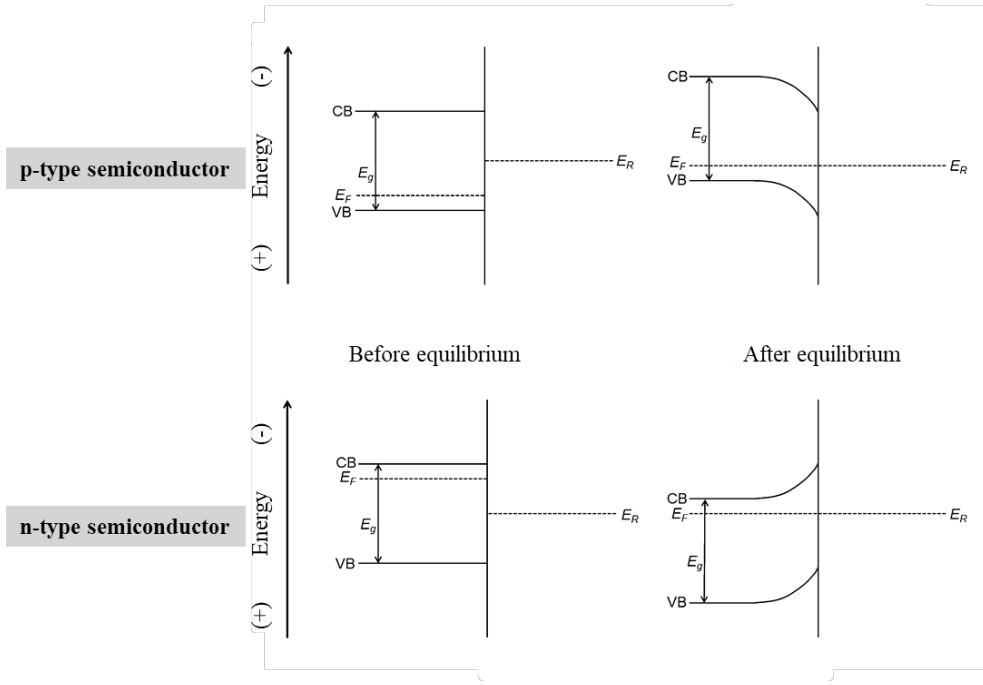

Figure 1.5. Semiconductor/liquid junction

1.4.2. PEC reduction reaction on photocathode

It is worth looking at how the PEC reduction reactions occur on a photocathode under illumination of sunlight. Figure 1.6 shows the schematic of PEC reduction reaction on a photocathode. Note that conduction band (E_C) potential of the p-type semiconductor photocathode should be more negative than desired redox potentials, H^+/H_2O, or CO_2 reduction reaction.

First of all, photogenerated charge carriers, electron-hole pairs, can be generated when the light is irradiated to the photocathode and is absorbed on photocathode. The number of photogenerated charge carriers depends on the bandgap of the photocathode materials, because semiconductors can absorb light that has higher energy than bandgap of materials. In non-equilibrium, steady-state illumination, the photogenerated charge carriers are formed near the photocathode surface, which can be represented using the concept called quasi-Fermi level. The quasi-Fermi level is indicative of the distribution of electron ($E_{F,n}$) and hole ($E_{F,p}$) under non-equilibrium. It formed an electric field in the photocathode, and corresponding voltage is called photovoltage or open-circuit voltage (V_{oc}).

Secondly, the photogenerated charge carriers are separated and transported to each electrode surface. Electrons move to cathode/electrolyte interface, and holes move to anode/electrolyte interface through the connected circuit. The electrons and holes are the source for reduction and oxidation reactions, it is need to minimize loss of the charge carriers, such as the charge recombination. Charge separation and transportation kinetics are related to characteristic of semiconductor materials, for example, carrier diffusion length, crystallinity, and carrier mobility.

Thirdly, the transported charge carriers are consumed for reduction and oxidation reaction at each electrode surface. To facilitate reaction, charge trap sites and the resistance between the electrodes and electrolyte should be minimized. Finally, when a reaction occurs, selectivity towards the desired reaction is important to avoid the formation of undesirable side products. Therefore, it is required to figure out mechanisms of reactions can be occurred, and to design the photocathode for selectively production of target products.

With these four key factors in mind, it is essential to select the appropriate materials and use a variety of engineering strategies to design photocathodes for efficient solar fuel productions.

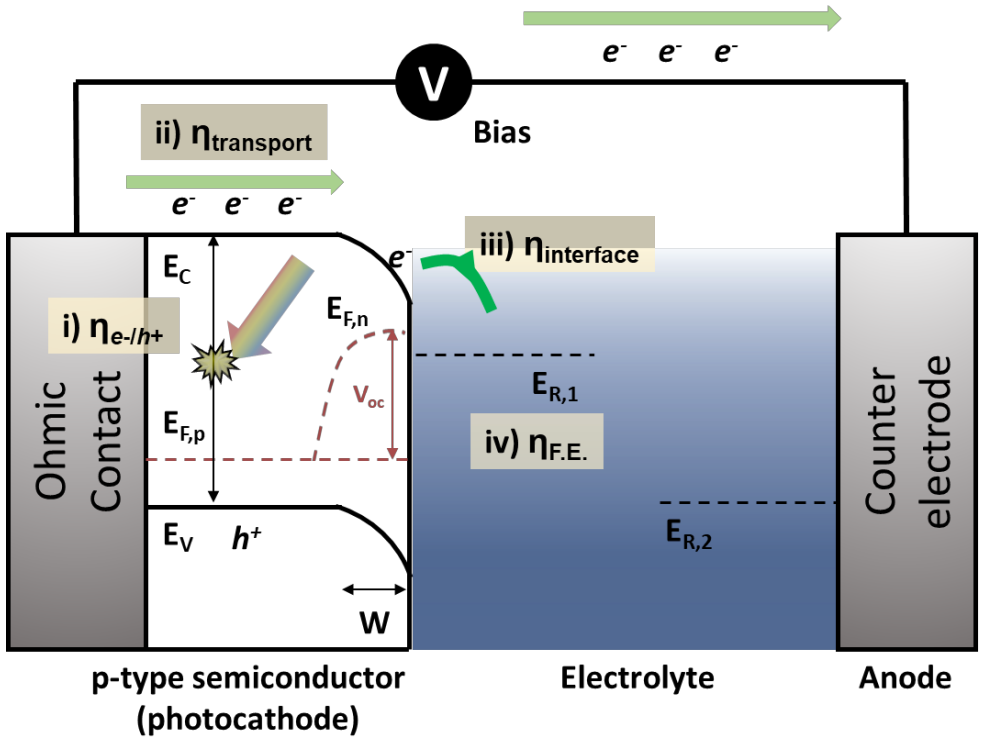

Figure 1.6. Schematic diagram of a simple PEC cell based on an p-type semiconductor photocathode under an external bias.

1.4.3. Candidate materials for photocathode

As mentioned in previous section, conduction band of semiconductor for photocathode should be more negative than the redox potential of desired reduction reaction. Band edge positions of some candidate materials for photocathode are depicted in Figure 1.7, which is referenced from the prominent recent review article.[13]

Among the candidate semiconductor for photocathode shown in Figure 1.7, silicon is an attractive material for photocathode in solar fuel production. Above all, silicon has a narrow bandgap of 1.12 eV that can absorb a larger portion of the solar spectrum from UV to near-infrared, giving it a high theoretical solar-to-fuel (STF) efficiency. Also, silicon is one of the most abundant elements in the Earth's crust, and technology for fabricating silicon wafers is well developed, which makes it to applied for photocathode to a relatively low cost.

However, silicon has several major drawbacks that make it difficult to use in photocathode. First is instability of silicon in electrolyte.[14] When silicon is exposed to air or electrolyte, insulating native silicon oxide layers are formed due to the thermodynamic oxidation potential. It causes Fermi level to be pinned, interrupting the band bending in photocathode and increasing charge transfer resistance at the photocathode/electrolyte interface. Secondly, reaction kinetics of either the CO_2 reduction reaction or hydrogen evolution reaction are normally multi-electron processes, which are generally sluggish on silicon surfaces.[15] Therefore, the kinetically difficult reduction reactions efficiency is lowered on silicon photocathode.

Despite these limitations, due to the advantages of silicon, many studies are being conducted to improve the properties of silicon photocathodes using various engineering strategies. In this thesis, the studies are conducted to improve the properties of silicon photocathode for each hydrogen evolution reaction and CO_2 reduction reaction by using appropriate strategies that introducing nanostructured catalysts on silicon photocathode. Since the hydrogen evolution reaction and the CO_2 reduction reaction have different reaction mechanisms, nanostructure catalysts specialized for each reaction was studied.

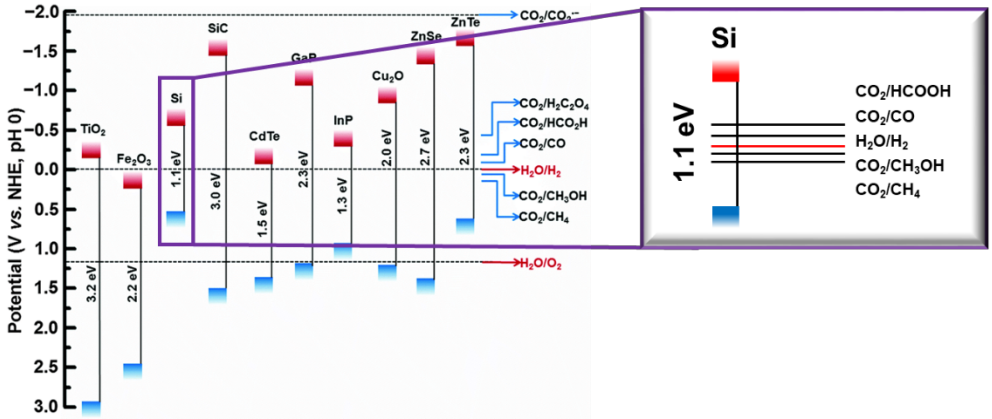

Figure 1.7. Conduction band and valence band positions of some candidate semiconductor photocathode and the redox potentials vs. NHE of hydrogen reduction and CO_2 reduction.

1.5. References

[1] British Petroleum Company, 1981. *BP statistical review of world energy*. London: British Petroleum Co.

[2] E. Alper, O. Y. Orhan, *Petroleum* **2017**, *3*, 109.

[3] W. E. Schiesser, A. J. Mchugh, G. W. Griffiths. Introductory Global CO2 Model, An (With Companion Media Pack). World Scientific Publishing Company, **2015**.

[4] A. Fujishima, K. Honda, *Nature* **1972**, *238*, 37.

[5] M. G. Walter, E. L. Warren, J. R. McKone, S. W. Boettcher, Q. Mi, E. A. Santori, N. S. Lewis, *Chemical reviews* **2010**, *110*, 6446.

[6] Z. Li, J. Feng, S. Yan, Z. Zou, *Nano Today* **2015**, *10*, 468.

[7] W. Tu, Y. Zhou, Z. Zou, *Advanced Materials* **2014**, *26*, 4607.

[8] R. Liu, Z. Zheng, J. Spurgeon, X. Yang, *Energy & Environmental Science* **2014**, *7*, 2504-2517.

[9] C. Jiang, S. J. A. Moniz, A. Wang, T. Zhang, J. Tang, *Chemical Society Reviews* **2017**, *46*, 4645.

[10] N. R. Council, *The hydrogen economy: opportunities, costs, barriers, and R&D needs*. National Academies Press: 2004

[11] K. P. Kuhl, T. Hatsukade, E. R. Cave, D. N. Abram, J. Kibsgaard, T. F. Jaramillo, *Journal of the American Chemical Society* **2014**, *136*, 14107.

[12] J. L. White, M. F. Baruch, J. E. Pander III, Y. Hu, I. C. Fortmeyer, J. Eujin Park, T. Zhang, K. Liao, J. Gu, Y. Yan, T. W. Shaw, E. Abelev, A. B. Bocarsly, *Chemical reviews* **2015**, *115*, 12888.

[13] X. Chang, T. Wang, J. Gong, *Energy & Environmental Science* **2016**, *9*,

2177.

[14] J. Zhao, T. M. Gill, X. Zheng, *Nano Research* **2018**, *11*, 3499.

[15] K. Sun, S. Shen, Y. Liang, P. E. Burrows, S. S. Mao, D. Wang, *Chemical reviews* **2014**, *114*, 8662.

Chapter 2

Water splitting on 3D/2D nanostructured TMDs catalysts

2.1. Introduction

Sustainable hydrogen production via photoelectrochemical (PEC) water splitting has been widely investigated as a promising alternative route to meet the substantial hydrogen demand over the world.[1] Various semiconductor materials, such as GaAs,[2] CuO,[3] CdTe[4] and Si,[5] have been explored as light absorbers for PEC hydrogen evolution reaction (HER). Silicon (*p*-Si) is a promising candidate for photocathodes because it is highly abundant and has an ideal band gap (1.12 eV) for absorbing a wide range of incident solar spectrum and band alignment for driving HER. However, *p*-Si suffers from sluggish surface kinetics due to its high hydrogen adsorption Gibbs free energy (ΔG_H). This induces a high surface overpotential between the *p*-Si/electrolyte interface.[6] Although precious metals such as Pt, Pd and Rh are widely used as HER catalysts to resolve such a problem of *p*-Si,[7-9] their scarcity and high costs limit their practical applications. Besides, *p*-Si is thermodynamically vulnerable to drive solar water splitting in an acidic electrolyte. The surface of *p*-Si exposed to an acidic medium rapidly forms oxides (SiO_2) or silicic acid (H_2SiO_3)[10]. Hence, integrating efficient non-noble-metal-based electrocatalysts with *p*-Si photoelectrodes, while protecting the vulnerable surfaces of silicon, may be a promising solution for making PEC water splitting practical.

Two-dimensional transition metal disulfides (2D TMDs), in particular MoS_2, are promising candidates for replacing precious metal catalysts, because they have inherently large surface to volume ratios and catalytically active edge sites for HER.[11-13] It has been reported theoretically and experimentally that the ΔG_H of sulfur at the edge of MoS_2 approaches near zero, whereas the ΔG_H at the basal plane reaches 2 eV.[14] Therefore, substantial studies have been performed to activate the catalytically inert basal planes[15, 16] or maximize the exposure of the active edge site[17, 18] of MoS_2 as an electrocatalyst. Interestingly, because the charge transfer along the in-plane direction of the MoS_2 layer is superior to that through the out-of-plane direction, the ideal structure of MoS_2 as an efficient HER electrocatalyst is to vertically align all domains inside MoS_2. The vertically aligned MoS_2 (VMS) thin film with maximally exposed active edge sites can be preferably grown by the kinetically controlled process.[19] Moreover, the dangling-bonds-mediated strong bonding produced by the vertically aligned domains in VMS can improve the adhesion and charge transfer between the MoS_2 thin film and *p*-Si photocathodes, whereas the horizontally grown MoS_2 may show poor those properties due to their weak van der Waals forces.

Not only 2D layered TMDs but also 3D TMDs (MxSy, M = Co, Fe, Ni, etc.) compounds, particularly bimetal compounds, have drawn significant

attention owing to their outstanding catalytic activity for both HER and OER.[20-23] Therefore, integration of 3D bimetal sulfides with 2D MoS_2 to build novel heterostructures has been a plausible approach and widely explored by many research groups.[24-26] However, most studies have grown 2D layered TMDs on Ni-based substrates to fabricate 2D TMD/3D Ni_3S_2 or directly synthesize 3D/2D TMD heterostructure catalysts in the powder form. These approaches make it difficult to exquisitely control the physical properties of TMD-based heterostructure catalysts with respect to the possible variation in substrates and to use these catalysts in various applications. The transferrable thin film catalysts are advantageous in that they can be attached to any arbitrary substrate and have extensive applicability compared with directly grown catalysts. To the best of our knowledge, 3D bimetal sulfides/2D MoS_2 heterojunction thin film catalysts for PEC water splitting have not been demonstrated yet.

In this chapter, we demonstrate large-area (12 cm × 12 cm) and transferable 3D transition metal sulfide nanoparticles/2D vertically aligned MoS_2 thin film catalysts for Si-based PEC hydrogen production for the first time. Heterojunction thin films of VMS and the iron-nickel sulfide nanoparticles (FNS NPs) are obtained via facile one-step process. The use of transferable 3D/2D TMD heterostructure thin film catalysts leads to drastic improvement in the PEC performance, especially in stability. The tailored

FNS NPs on VMS induce favorable band alignment which facilitates an efficient charge transport and inhibits the charge accumulation at the VMS/electrolyte interface, which is visualized by scanning photoelectrochemical microscopy (SPECM).

2.2. Experimental procedures

DFT-calculations. The density functional theory (DFT) calculations was conducted using the Vienna Ab initio Simulation Package (VASP) code based on the projector augmented wave (PAW) pseudopotential.[27, 28] We selected 400 eV for the cutoff energy for the plane-wave basis set. For supercells, k-space meshes of 4 × 4 × 1, 4 × 4 × 1, and 2 × 1 × 1 were used for Fe-doped Ni_3S_2, MoS_2 basal plane, and MoS_2 edge, respectively. The ionic configurations were relaxed until the atomic forces were decreased to within 0.02 eV $Å^{-1}$. The entropy of H_2 gas was taken from a thermodynamic table, and the zero-point energy of the H atom was included

FNS NPs/VMS thin film synthesis. SiO_2 (300 nm)/Si wafers (1–10 Ω-cm, <100> plane, DASOM RMS Co., Ltd) were cleaned with conventional cleaning procedures using a standard piranha solution (1:3 volume ratio of H_2O_2, 30% grade and H_2SO_4, 95% grade) followed by ultrasonication in acetone, isopropyl alcohol, and deionized (DI) water. A water purification system (Human Power, Human Co, Ltd., 18.3 MΩ-cm) was used to purify the DI water. The Mo (2 - 5 nm), Ni (0 – 1 nm), and Fe (0 – 1 nm) thin films with various Ni/Fe ratios were deposited by using an electron beam evaporator (Korea Vacuum Tech Co, Ltd). To synthesize the VMS thin films, we used the simple sulfurization process as follow. The N_2 and H_2 (99.9999% high purity) gases were used for the sulfurization process in a thermal chemical vapor deposition system (CVD). First, the CVD furnace was heated to 550 °C and was maintained at this temperature for 30 min under flow of N_2 and H_2. By using mass flow controllers (MKS Co., Ltd, Type 1479A), the flow

rates of N_2 and H_2 were set at 500 and 100 cm^3 min^{-1}, respectively, at which time the pressure was 1 Torr. Subsequently, the sulfur powder (99.998%, Sigma-Aldrich, 213292) precursor was sublimated in the other heating zone with the temperature set to 250 °C. The sulfurization process of Mo/Ni/Fe thin films took 15 min to finish. After the sulfurization process, the CVD-grown thin films were coated with the [poly(methyl methacrylate)] (PMMA) layer using a spin-coater. The PMMA precursor was prepared by dissolving PMMA (GPC 10000, Sigma-Aldrich, 81497) in chlorobenzene (99.5% purity, Sigma-Aldrich, 319996) with a concentration of 2 g/50 ml. The PMMA/thin films/SiO_2/Si substrates were immersed in a buffered oxide etchant to separate the thin films from the Si substrate by etching away the SiO_2 layers. The separated thin films were washed with DI water seven times to clear away the residual etchants and were transferred onto arbitrary substrates. After the PMMA/thin film membranes had completely adhered to the substrates, the PMMA layers were removed using a hot acetone bath.

(Photo)electrochemical measurement. For the PEC measurements (Ivium Technologies, Model: Nstat), a three-electrode system with a saturated calomel electrode (SCE) as the reference electrode and a graphite rod (WonATech Co., Ltd) as the counter electrode was used in a 0.5 M H_2SO_4 standard electrolyte solution. We used a graphite rod counter electrode instead of a Pt electrode to prevent the deposition of Pt on the working electrode. The three-electrode system was set up inside a quartz vessel, which protected the samples from UV absorption. The conversion equation of potentials vs. RHE is expressed as the following equation:

$$E_{RHE} = E_{SCE} + E^{\circ}_{SCE} + 0.059 \times pH \quad (E^{\circ}_{SCE} = 0.242 \text{ vs. SHE})$$

where E_{SCE} is the experimentally measured potential vs. the saturated calomel electrode, E°_{SCE} is the potential of the saturated calomel electrode with respect to the standard hydrogen potential (SHE), and the pH of 0.5 M H_2SO_4 is 0.27. A Xe arc lamp (Abet Technologies, LS150) calibrated to an output of 100 mW cm^{-2} (AM 1.5 G condition) was used. The linear sweep with cathodic direction was carried out with a scan rate of 10 mV s^{-1}. The incident-photon-to-current conversion efficiency (ICPE) was measured with a light source and a monochromator (DONGWOO OPTRON, MAC150), and the efficiency was calculated by the following equation:

$$IPCE\ \ (\lambda) = EQE\ \ (\lambda) = \frac{|j_{ph}(mA/cm^2)| \times 1239.8\ (V \times nm)}{P_{mono}\ \ (mW\ /\ cm^2) \times \lambda\ (nm)}$$

where j_{ph} is the photocurrent of the sample, λ is the wavelength and P_{mono} is the power of the monochromator. The external quantum efficiency was measured with a standard Si photodiode. EIS measurement was performed by applying a constant potential of 0.27 V vs. RHE near the open-circuit potential, and the sweeping frequency range was from 250 kHz to 1 Hz using a 10 mV AC dither.

The Faradaic efficiencies were measured in a two-compartment photoelectrochemical cell separated by the Nafion 117 membrane. Before reaction, the two compartments of the reactor were degassed by bubbling with Ar gas for 30 min. During the reaction, the Ar gas was continuously flowed into the electrolyte in the cathodic compartment with a rate of 20.0 sccm and vented directly into a gas-sampling loop of a gas chromatography measurement system (Agilent GC 7890B), which is equipped with a thermal conductivity detector and a micro-packed column

(ShinCarbon ST 100/120). The Ar gas was used as the carrier gas and the evolved H2 was detected by a thermal conductivity detector (TCD). A gas sample was analyzed automatically every 8 min. The IMPS measurements were performed using the PEC measurements (Ivium Technologies, Model: Nstat) combined with a programmable light sources (Ivium Technologies, Model: ModuLight) in the identical three-electrode system described above. A white LED with a wavelength of 425~660 nm was used at a power of 5 mW cm^{-2}. A modulation intensity of 10% was used, and the frequency of the modulation was swept from 1 MHz down to 0.1 Hz.

SPECM measurement. The SPECM measurements were performed by an Ivium potentiostat (Ivium Technologies, Compact-stat) with a three-electrode system using a Pt wire counter electrode, saturated calomel reference electrode and working electrode in a 0.5 M H_2SO_4 standard electrolyte solution. The three-electrode system was built inside a home-designed reaction bath. A 532-nm laser was focused on the surface by a long-working-distance objective lens (Mitutoyo, M Plan Apo 5×, N.A. = 0.14, W.D. = 34 mm). The incident laser power was ~200 μW, measured using a power meter (Newport, Ophir 7Z01500 Nava), and the focused laser spot size was ~5 μm in diameter. The focused laser spot was scanned using a microstage or Galvano mirrors. Photocurrent was measured at constant voltage (-0.1 V vs. RHE) and converted to voltage signal using a break-out box (Ivium Technologies, Peripheral Port Expender) and a lock-in amplifier (Stanford Research Systems, SR380) at an optical chopping frequency of ~100 Hz.

Characterization. The Raman spectra of the synthesized MoS_2 thin films were

obtained with a Lab RAM HR (Horiba JobinYvon, Japan) at an excitation wavelength of 532 nm. The structural study of synthesized MoS_2 thin films was confirmed by a Bruker D8 advance diffractometer, equipped with a Cu Kα source. AFM (XE-100, Park Systems) measurements were performed using non-contact-mode with a scan rate of 0.5 Hz to identify the surface morphologies and thicknesses of the synthesized MoS_2 thin films. Synchrotron radiation photoelectron spectroscopy experiments were performed in an ultrahigh vacuum chamber (base pressure of ca. 10^{-10} Torr) with a 4D beam line, equipped with an electron analyzer and a heating element, at the Pohang Acceleration Laboratory. The onset of photoemission, which corresponds to the vacuum level at the surface of the MoS_2 thin film, was measured using an incident photon energy of 350 eV with a negative bias on the sample. The results were corrected for charging effects using Au 4*f* as an internal reference. To investigate the microstructures of the synthesized MoS_2 thin films, TEM (JEOL JEM-2100F, 200 kV) was used. UV-Visible spectroscopy (JASCO-670) was used to measure the transmittance and absorption spectra of the synthesized MoS_2 thin films.

2.3. Results and discussion

It is well known that the chemisorption energy between protons and the electrocatalyst surface is closely correlated to the hydrogen evolution performance of electrocatalysts. To elucidate the catalytic activity of the designed 3D/2D TMD heterostructure electrocatalysts, we used DFT to calculate the ΔG_H on the surface of each catalyst. In Figure 2.1(a), the edge site of MoS_2 has a ΔG_H significantly lower than the H-basal plane of MoS_2, which is close to zero. As reported by Sabatier's principle, a near-zero value of hydrogen binding energy is known as optimal for catalysts because H can be likely attached to and desorb from the catalyst surface to hydrogen evolution reaction. Thus, it can be concluded that the vertically aligned MoS_2, as illustrated in Figure 2.1(c), is advantageous in terms of ΔG_H compared with the pristine MoS_2, shown in Figure 2.1(b). In addition, in such a domain arrangement, the in-plane electron conductivity, which is characteristic of 2D layered MoS_2, can be fully used. Furthermore, Ni_3S_2 and Fe-doped Ni_3S_2 are also found to have significantly lower ΔG_H than the H-basal plane of MoS_2. These results clearly show that these catalysts could exhibit better catalytic activity than the basal plane of MoS_2, though showing slightly high ΔG_H than the edge-site of MoS_2. According to recent studies,[24, 29] however, the significantly decreased Gibbs free energy at the interface between MoS_2 and Ni_3S_2 or Fe-doped Ni_3S_2 (FNS) was predicted, promoting robust proton reduction at the interface. Therefore, if a 3D/2D TMD heterostructure is implemented, the HER may be preferentially concentrated at this active interface, suppressing the dissolution of MoS_2 during the HER, as shown in Figure 2.1(d).

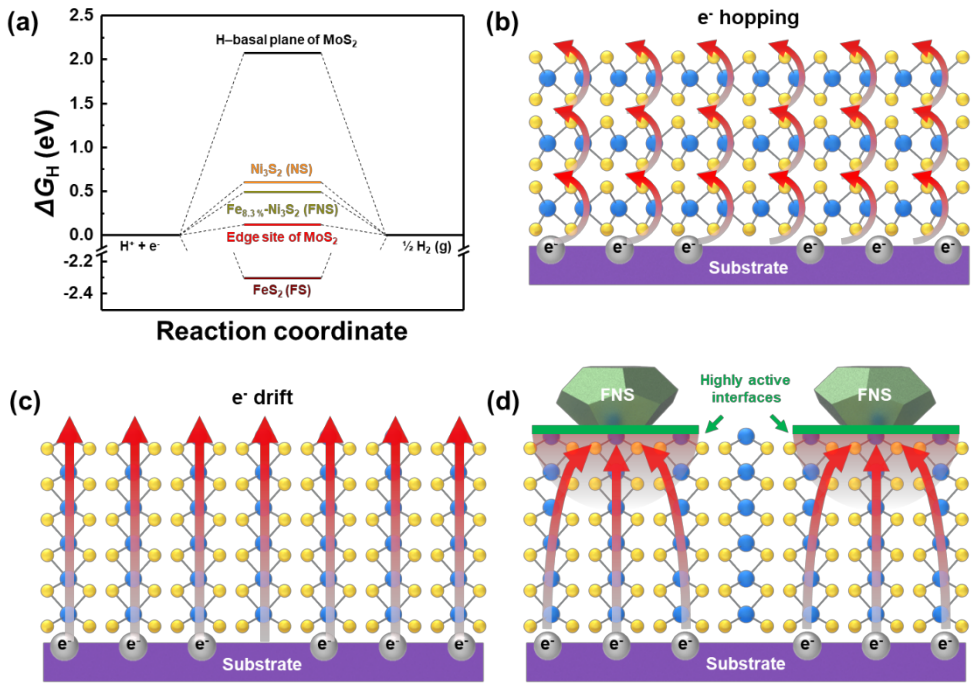

Figure 2.1. (a) Free-energy diagram of H adsorption on the site of each catalyst from DFT calculation. (b-d) Schematics of pristine MoS_2 (PMS), vertically aligned MoS_2 (VMS), and Fe-doped Ni_3S_2/VMS heterostructure.

The FNS/VMS thin films were synthesized by a simple one-step sulfurization method of Fe/Ni/Mo-metal thin film precursors on SiO_2/Si substrates. Figure 2.2(a) presents a schematic of the CVD method used in this study. The 2 nm Mo layer and subsequent Ni or Fe layers of various thicknesses were deposited onto a SiO_2/Si substrate using an e-beam evaporator. The total thickness of the Ni and Fe layer with various combinations (Ni only, Ni:Fe = 9/1, 5/5, Fe only) is fixed to 1 nm. The VMS thin films were successfully synthesized by rapid sulfurization in a CVD chamber at 550 °C for 15 min, whereas pristine MoS_2 (PMS) thin film was synthesized at 900 °C for 30 min in a CVD chamber, similar to other reports.[30, 31] While the Mo layer becomes VMS, by changing the thickness ratio of the Ni/Fe layer, the Ni/Fe layers are agglomerated to Ni_3S_2 (Ni only, NS), Fe:Ni_3S_2 (Ni/Fe=9, F1N9S), Ni:FeS_2 (Ni/Fe=1, F5N5S) and FeS_2 (Fe only, FS) nanoparticles on the top of VMS, resulting in Ni_3S_2/VMS (NS/VMS), Fe:Ni_3S_2/VMS (F1N9S/VMS), Ni:FeS_2/VMS (F5N5S/VMS) and FeS_2/VMS (FS/VMS), respectively. As shown in Figure 2.2(b-c), the agglomerated nanoparticles have sizes ranging from a few nanometers to one hundred nanometers. For the various characterizations of the synthesized thin films and their application as HER catalysts, they had to be transferred to a designated substrate. Glass, *p*-Si and SiO_2/Si are extensively utilized as substrates for such characterizations. Poly [methyl methacrylate] (PMMA), the supporting polymer, was spin coated onto the synthesized thin films for the typical wet transfer process. The PMMA/thin films were separated from the SiO_2/Si substrate by etching the SiO_2 layer in a bath of buffered oxide etchant. Subsequently, the separated films were transferred onto arbitrary substrates. Figure 2.3 shows the photographs of the synthesized large-area (12 cm × 12 cm) thin films

on glass substrates and corresponding Raman spectra at nine different positions, respectively. The synthesized MoS_2 thin film was greenish yellow.

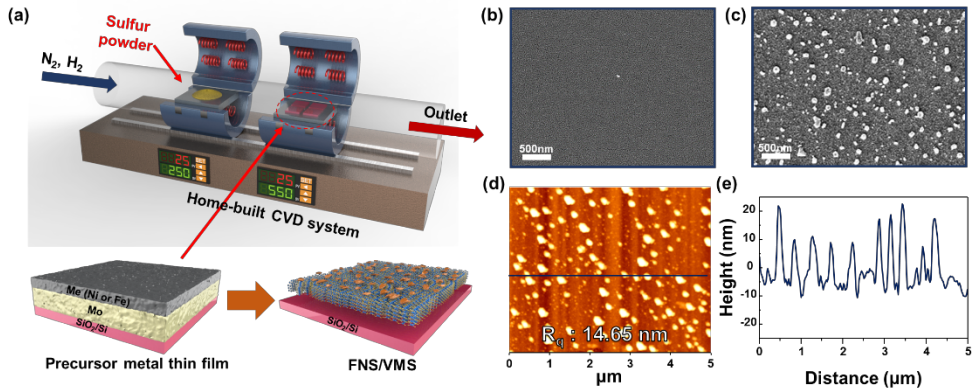

Figure 2.2. (a) Schematic of experimental procedures and characterization of synthesized 3D metal sulfide decorated VMS. SEM images of (b) Fe/Ni/Mo metal precursors on SiO_2 substrate and (c) synthesized metal sulfide on VMS. (d) AFM image of synthesized metal sulfide on VMS. (e) Corresponding line profiles of height along the blue line in (d).

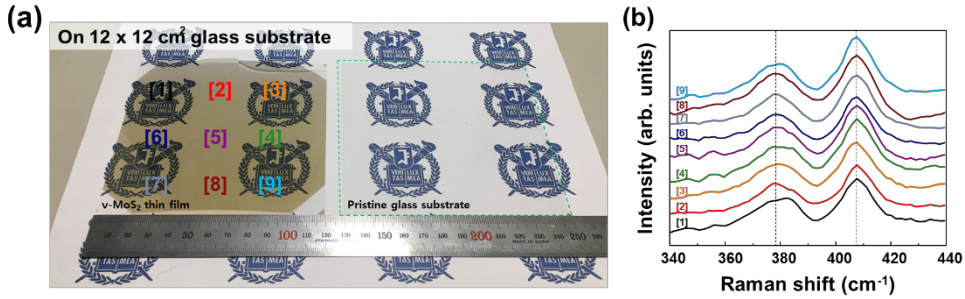

Figure 2.3. (a) Photograph of synthesized VMS thin films on flexible and bare flexible glass substrate. (b) Raman spectra of synthesized VMS thin films on flexible glass substrate at each site.

The atomic vibration modes of TMD thin films were inspected by Raman spectroscopy.[32] The Raman spectra of the PMS, VMS and FNS NPs/VMS thin films synthesized with various Ni/Fe precursor ratios are shown in Figure 2.4(a). Two characteristic peaks, E^1_{2g} (in-plane vibration) and A_{1g} (out-of-plane vibration), appeared around 378 and 405 cm^{-1}, respectively. The peak gap between these two Raman modes (E^1_{2g} and A_{1g}) of the MoS_2 layer strongly depends on the number of stacked layers and indicates the overall thickness of MoS_2 thin films.[32] The peak gap between the E^1_{2g} and A_{1g} modes was approximately 27 cm^{-1}, indicating that the synthesized thin films consist of multilayers. The Raman spectrum of the PMS shows partially reduced peak widths than other VMS-based thin films, which is attributed to the phonon confinement effect.[33] Figure 2.2(d) and Figure 2.5 shows the AFM images of PMS, VMS and F1N9S/VMS thin films for the study of their surface morphologies. The very flat MoS_2 thin film with a root-mean-square roughness of 0.52 nm was synthesized for the PMS thin film. The AFM image of the VMS also shows that there is some wrinkle, but the flat film was obtained with the root-mean-square roughness of 4.72 nm. However, the morphology of F1N9S/VMS was different from those of the other two thin films. FNS NPs were appeared on the VMS. Due to these particles, this thin film showed root-mean-square roughness of 14.65 nm, which is more than that of PMS and VMS. The crystalline structure of the synthesized TMD thin films was studied by X-ray diffraction (XRD). Figure 2.6 presented the XRD patterns of the PMS, VMS, FNS/VMS thin films. All the XRD patterns of synthesized thin films exhibited a diffraction peak at $2\theta = 14°$, which can be assigned to the (002) plane of 2H-MoS_2. Therefore, it can be confirmed that both PMS and VMS have a 2H-MoS_2 phase.

However, unfortunately, no diffraction peaks were found for FNS nanoparticles, it is because the FNS nanoparticles is very small in size and have poor crystallinity. The crystal structure of FNS was studied in TEM analysis, which will be described later.

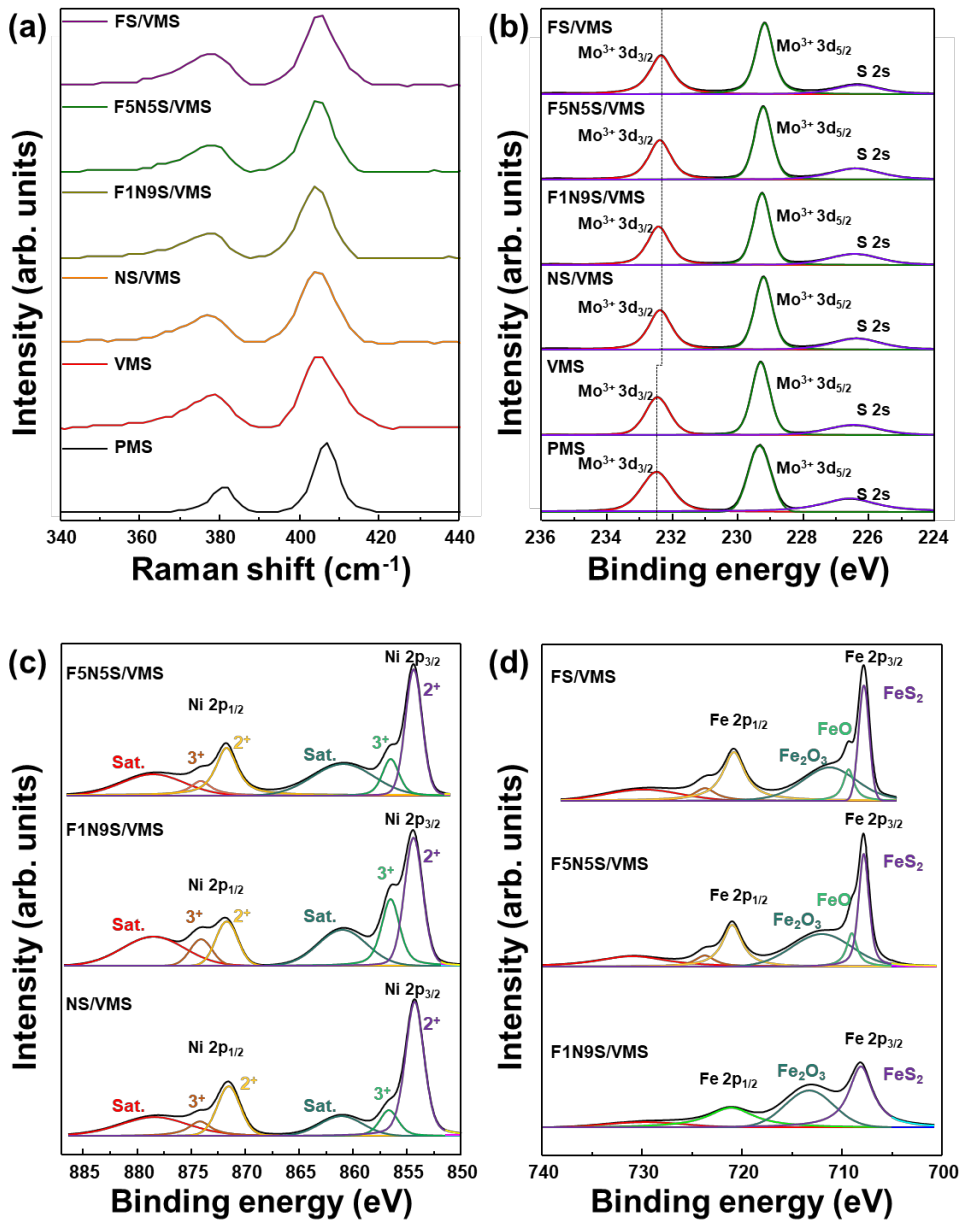

Figure 2. 4 . (a) Raman spectra of the synthesized thin films. XPS analysis of the synthesized thin films for (b) Mo 3d, (c) Ni 2p, (d) Fe 2p.

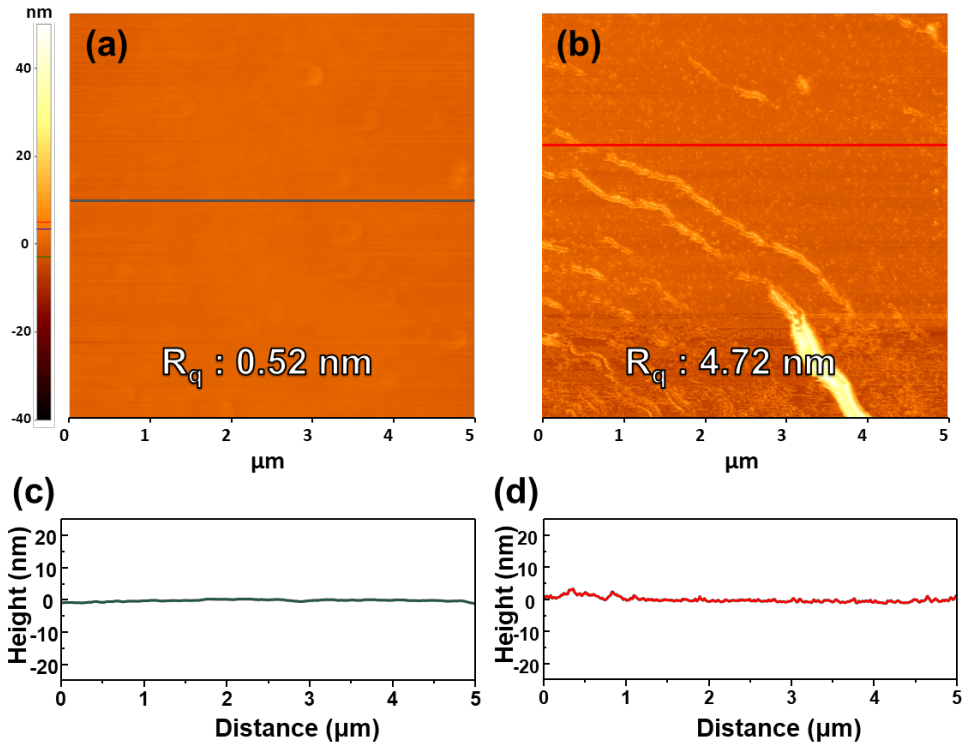

Figure 2.5. AFM images of (a) PMS and (b) VMS. (c) corresponding line profiles of height along the green line in (a). (d) Corresponding line profiles of height along the red line in (b).

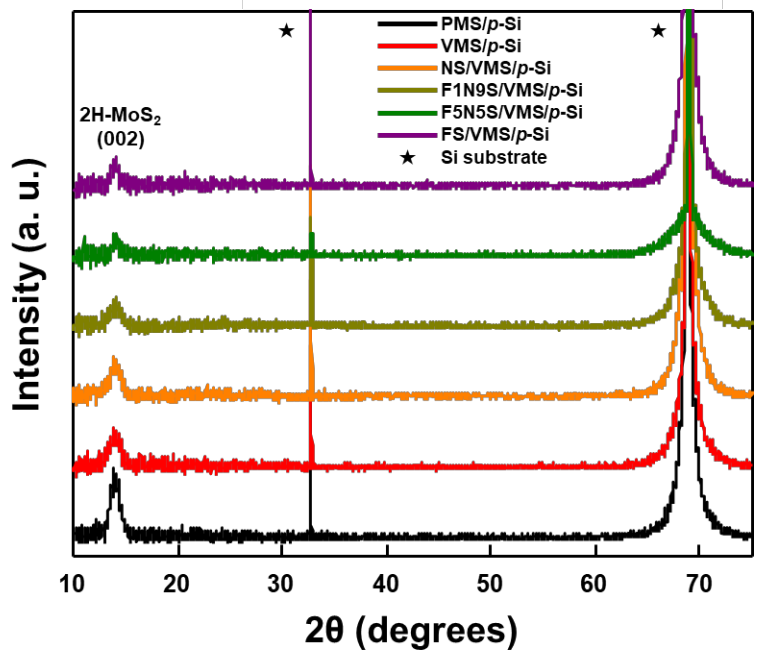

Figure 2.6. X-ray diffraction patterns of synthesized thin films.

The chemical components and atomic ratios of the synthesized thin films were investigated using X-ray photoemission spectroscopy (XPS). The core level spectra of Mo 3*d*, Ni 2*p* and Fe 2*p* were plotted (Figure 2.4(b-d)). In the Mo 3*d* core level spectra, the Mo^{4+} $3d_{3/2}$ and Mo^{4+} $3d_{5/2}$ peaks of the FNS NPs/VMS thin films slightly shifted to lower binding energies than the Mo^{4+} $3d_{3/2}$ and Mo^{4+} $3d_{5/2}$ peaks of the PMS and VMS, which implies there is an electronic interaction between FNS NPs and VMS.[29] The Ni 2*p* spectra in Figure 2.4(c) can be deconvoluted to two spin-orbit doublets and two satellites. The binding energies at 854.4 eV for Ni $2p_{3/2}$ and 871.6 eV for Ni $2p_{1/2}$ are spin-orbit characteristics of Ni^{2+}, whereas the binding energies at 856.5 eV for Ni $2p_{3/2}$ and 874.1 eV for Ni $2p_{1/2}$ are spin-orbit characteristics of Ni^{3+}.[34] The slight increase in the Ni^{3+} peak in F1N9S/VMS is inferred to be due to the rarely found Ni_2FeS_4 phase (Figure 2.7). Figure 2.4(d) displays the XPS spectra of the Fe 2*p* region, which shows two major peaks centered at 720.9 and 707.8 eV assigned to Fe $2p_{1/2}$ and Fe $2p_{3/2}$ peaks, respectively. Moreover, the spin energy separation between these two peaks is approximately 13 eV, implying the typical characteristic of FeS_2 spectra.[35, 36]

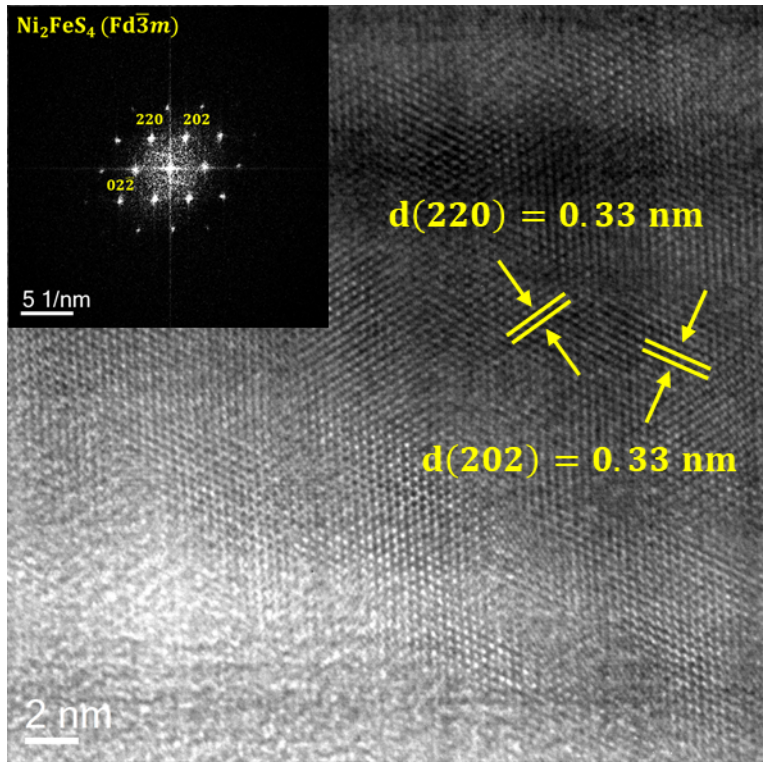

Figure 2.7. The rarely found Ni_2FeS_4 phase in high-resolution TEM images of F1N9S/VMS thin film.

The nanostructures of the synthesized thin film catalysts were investigated by transmission electron microscopy (TEM). A high-resolution TEM (HRTEM) image (Figure 2.8(a)) shows that the VMS thin film consists of highly dense, vertically aligned domains which is comparable to former studies.[37-39] Figure 2.8(b-c) depict the cross-sectional TEM images after the introduction of the Ni layer onto the Mo precursor. The VMS thin films synthesized together with Ni only layers showed a nano-particulate surface, particle sizes ranging from a few nanometers to one hundred nanometers. It can be seen that horizontally aligned MoS_2 regions with the thickness of a few atomic layers exist on vertically aligned MoS_2 underneath the nanoparticle, which indicates that the VMS thin film is not fully vertically aligned due to the nanoparticle. The HRTEM image and electron diffraction pattern achieved by the fast fourier transform in Figure 2.8(d) indicate that the nanoparticles on the VMS thin film were the heazlewoodite Ni_3S_2 (R32, PDF Number 00-044-1418) with the *d*-spacings of 0.41 and 0.29 nm corresponding to the (101) and (110) planes, respectively. The HRTEM images of the VMS thin film synthesized with the Fe only layer as a precursor are shown in Figure 2.8(e-f). Based on the HRTEM and the SAED, the nanoparticles on the VMS thin film were identified as the marcasite FeS_2 (Pnnm, PDF Number 00-037-0475) with the *d*-spacings of 0.22 and 0.17 nm corresponding to the (200) and (002) planes, respectively. In addition, HRTEM images of the F1N9S/VMS and F5N5S/VMS are acquired to identify their crystal structure. According to Figure 2.9(a-b), it is clearly shown that the F1N9S/VMS has the same crystal structure with Ni_3S_2, while F5N5S has FeS_2 crystal structure. The TEM analysis indicates that when the sulfurization process is conducted using the Ni/Fe/Mo precursor layer, Mo is

converted to the 2D VMS layer, whereas the Ni/Fe layer becomes a particular-shaped FNS NPs. Energy-dispersive X-ray spectrometry (EDS) mapping results of the F1N9S/VMS/*p*-Si and F5N5S/VMS/*p*-Si are shown in Figure 2.8(g) and Figure 2.9(c). Based on the elemental distribution, Ni, Fe and S elements are homogeneously distributed on the top 3D FNS NPs. Even though the precursor layers were subsequently deposited in order of Fe, Ni and Mo, it is reasonable to speculate that the top Fe and Ni layers are well alloyed and agglomerated to FNS NPs on the VMS thin film.

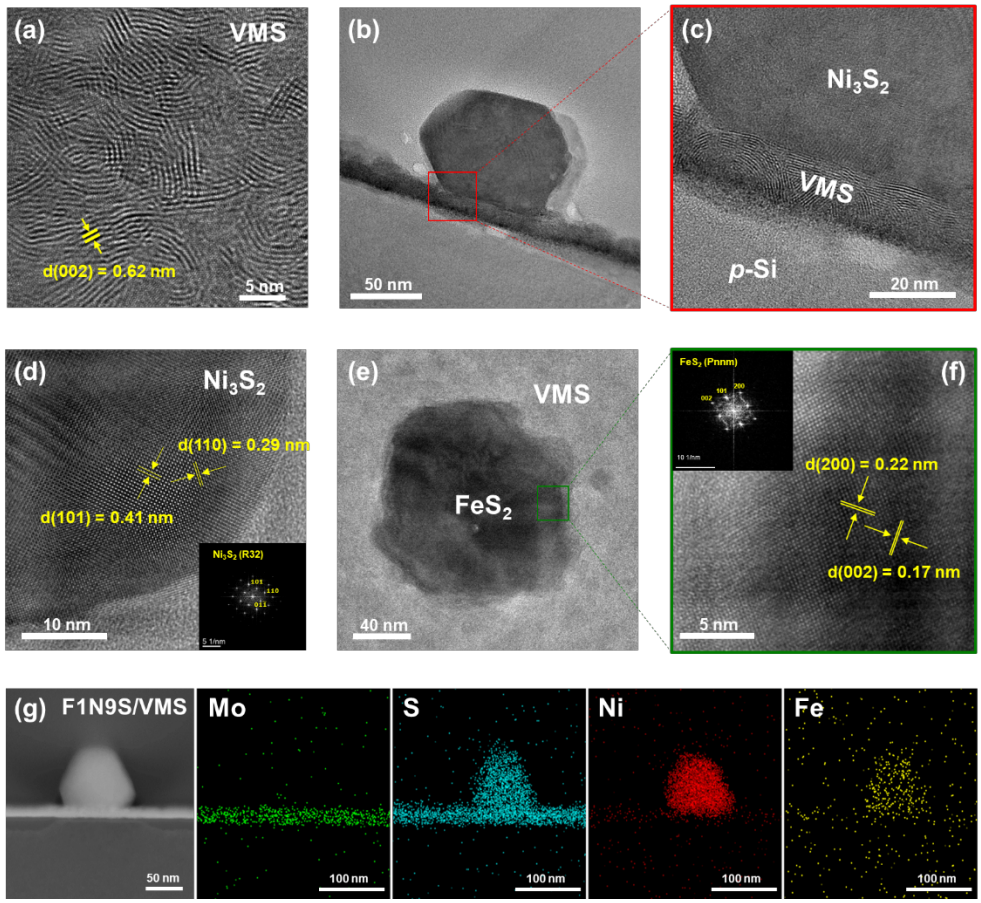

Figure 2.8. TEM images of the synthesized thin films. (a) VMS, (b–d) cross-sectional high-resolution TEM images of Ni_3S_2 NPs/VMS thin film, (e and f) high-resolution TEM images of FeS_2 NPs/VMS thin film. (g) Cross-sectional HAADF-STEM image and EDS mapping of F1N9S/VMS thin films on *p*-Si.

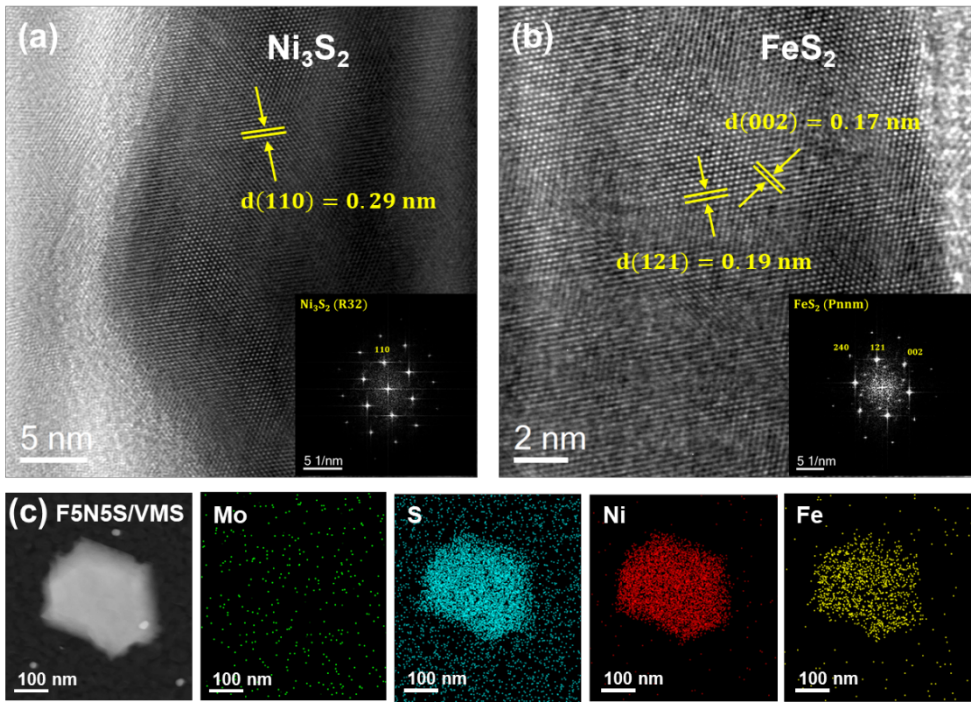

Figure 2.9. High resolution TEM images of (a) F1N9S/VMS and (b) F5N5S/VMS thin films. (c) HAADF-STEM image and EDS mapping of F5N5S/VMS thin film.

Because the MoS_2-based thin film catalysts in this study are semitransparent, most of the incident light is absorbed by underlying *p*-Si. Hence, it is imperative to identify whether the photogenerated electrons at the surface of *p*-Si efficiently transported toward the thin film catalyst/electrolyte interface for reducing protons (H^+). Band bending of the FNS NPs/VMS/*p*-Si heterostructures was explored by ultraviolet photoemission spectroscopy (UPS) and XPS valence band spectra. The secondary electron cut-off (SEC) spectra of bare *p*-Si, PMS/*p*-Si, VMS/*p*-Si, FNS NPs/*p*-Si and reference Au foil electrodes are shown in Figure 2.10(a). All SEC spectra were calibrated by the work function of the Au reference (5.1 eV). Given that the photoelectrons have the escape depth of ~5 nm, shorter than the thickness of thin film catalysts, the work functions of the *p*-Si and thin film catalysts can be determined from the SEC as 4.7 eV, 4.3 eV and 4.4 eV for *p*-Si, PMS and VMS respectively (see Figure 2.10(a), 2.11 and Table 2.1). Furthermore, the work function of FNS NPs in Figure 2.10(a) was measured by transferring the separately grown FNS NPs on *p*-Si to exclude the overlapping effect in SEC spectra between FNS NPs and VMS. The work function values of FNS NPs are also summarized in Figure 2.11 and Table 2.1. According to the XPS valence-band spectra plotted in Figure 2.10(b), the energy differences between the Fermi level and valence band maximum (E_F - E_V) were obtained for bare *p*-Si (0.4 eV), PMS/*p*-Si (1.4 eV), VMS/*p*-Si (1.1 eV) and Au reference electrode (0 eV). For the same reason as the UPS measurements to rule out the overlapping effect, the E_F - E_V values of FNS NPs were measured separately, as shown in Figure 2.10(b) and Table 2.1. From the absorbance spectra in Figure 2.12, the optical band gaps of PMS and VMS were calculated to be around 1.7 eV and 1.68 eV by the Tauc plot, whereas the reported

values were utilized as the optical band gap of FNS NPs. Considering that the VMS has the E_F - E_V value of 1.12 eV, the transferred VMS thin film is an n-type semiconductor, as in our previous study.[17] Interestingly, as illustrated in Figure 2.10(c), the E_F - E_V value of the heazlewoodite Ni_3S_2 NPs (Ni only), which is known to have metallic nature, was almost 0 eV.[40] As the content of Fe in FNS NPs increases, the E_F - E_V values were gradually increased. The marcasite FeS_2 NPs (Fe only) showed the E_F - E_V value of 0.42 eV with the optical band gap of 1.17 eV.[41]

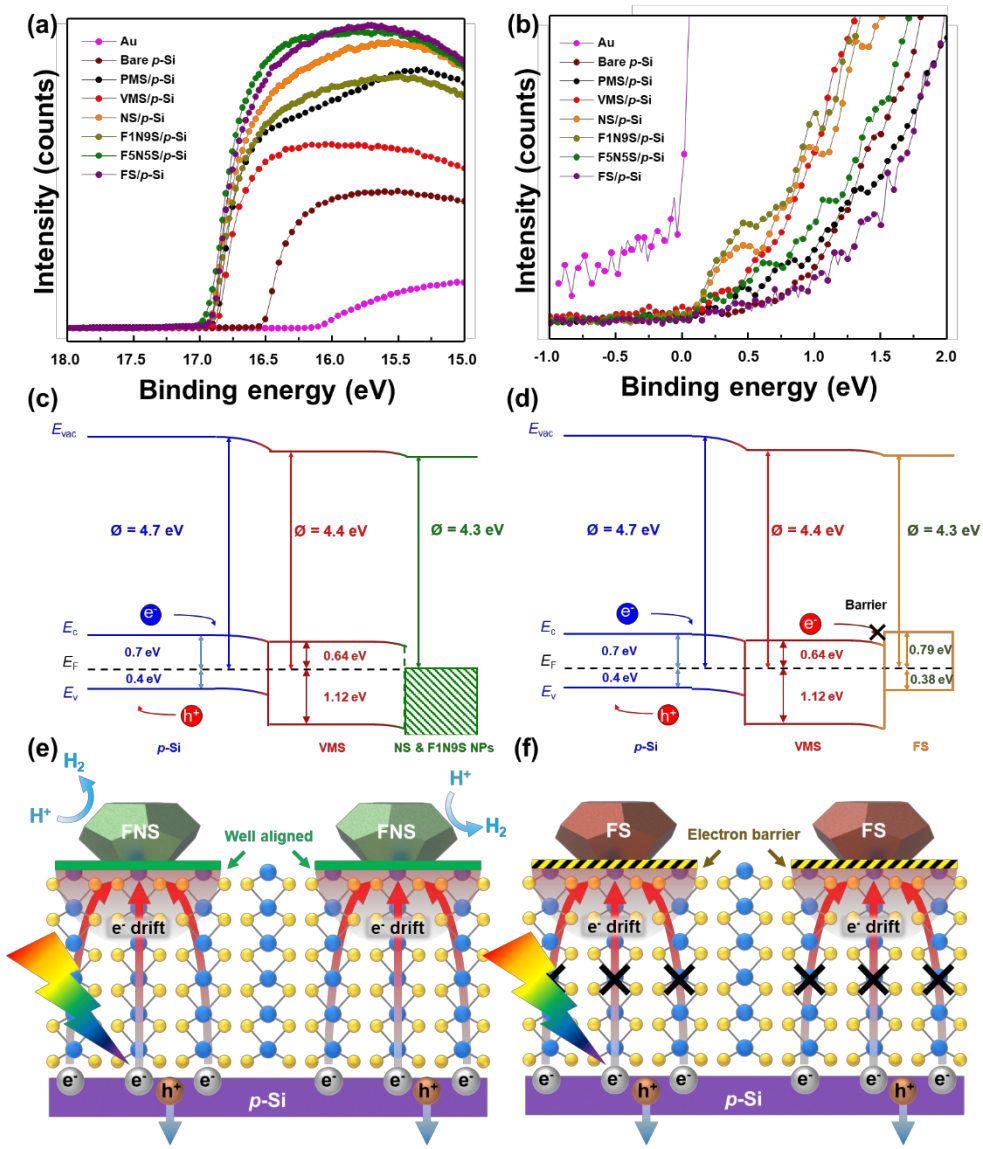

Figure 2. 10 . (a) Ultraviolet photoemission spectroscopy (UPS) and (b) X-ray photoemission valence spectra of bare *p*-Si, PMS/*p*-Si, VMS/*p*-Si, NS/*p*-Si, F1N9S/*p*-Si, F5N5S/*p*-Si and FS/*p*-Si. Each measured value was corrected with Au reference. Energy band diagrams of (c) NS or F1N9S/VMS/*p*-Si and (d) FS/VMS/*p*-Si heterojunction photocathodes. (e) and (f) Schematics of the charge transfer for FNS/VMS/*p*-Si and FS/VMS/*p*-Si photocathodes, respectively.

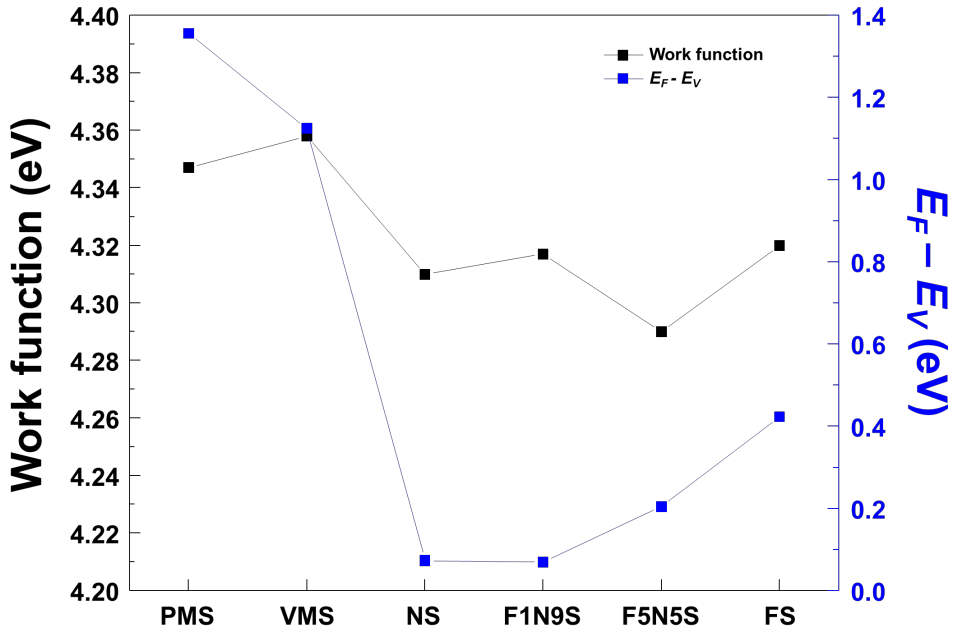

Figure 2.11. Calculated work function and E_F - E_V values of PMS/*p*-Si, VMS/*p*-Si, and FNS NPs/*p*-Si photocathodes.

Table 2.1. Calculated work function and $E_V - E_F$ values of PMS/*p*-Si, VMS/*p*-Si, and FNS NPs/*p*-Si photocathodes.

Photocathode	Work function (eV)	E_F – VBM (eV)
Au	5.10	0
***p*-Si**	4.70	0.40
PMS	4.34	1.36
VMS	4.36	1.12
NS (Ni_3S_2)	4.31	0.033
F1N9S	4.32	0.030
F5N5S	4.29	0.17
FS (FeS_2)	4.32	0.38

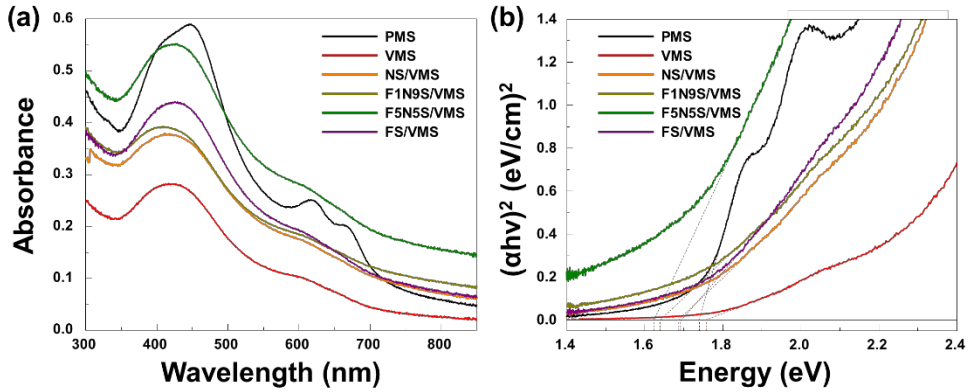

	PMS	VMS	NS/VMS	F1N9S/VMS	F5N5S/VMS	FS/VMS
Optical band gap (eV)	1.736	1.756	1.686	1.638	1.623	1.694

Figure 2. 12 . (a) Absorbance spectra and (b) Tauc plots of PMS, VMS, NS/VMS, F1N9S/VMS, F5N5S/VMS, and FS/VMS thin film catalysts.

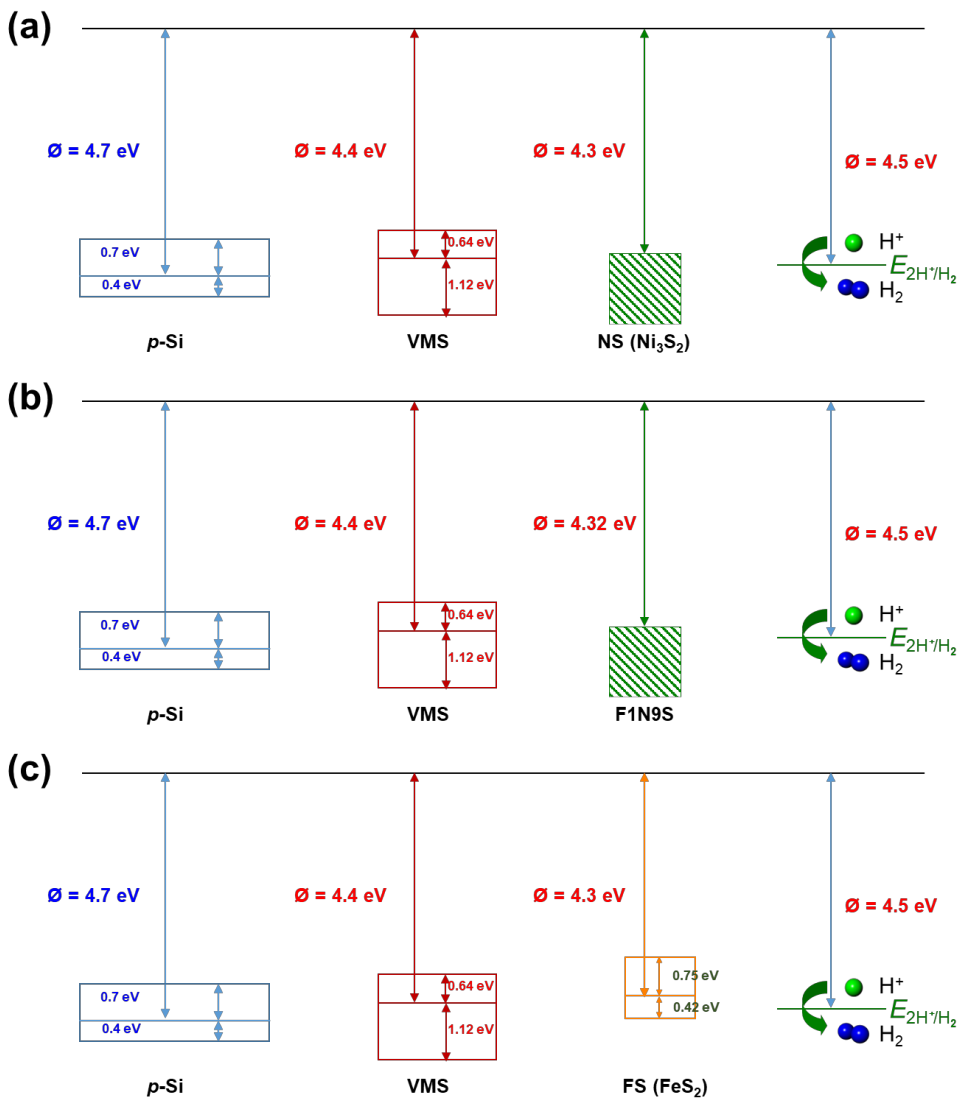

Figure 2. 13 . (a) Flat band diagram of NS/VMS/*p*-Si. (b) Flat band diagram of F1N9S/VMS/*p*-Si. (c) Flat band diagram of FS/VMS thin film photocathodes.

Based on these results, the flat band (Figure 2.13) and band bending diagrams (Figure 2.10(c-d)) for the FNS NPs/VMS/*p*-Si heterostructure were obtained. The *p*-Si and VMS form a *p*-*n* junction, inducing downward band bending in *p*-Si. Because the work function of VMS is slightly higher than that of other FNS NPs, downward band bending is induced when the VMS thin film is in equilibrium with the FNS NPs. For the Ni_3S_2 and F1N9S NPs as shown in Figure 2.10(c, e), thanks to their metallic nature, the band bending diagram clearly shows that the photogenerated electrons from *p*-Si could be easily transported to the NPs/electrolyte interface without an electronic potential barrier. However, as illustrated Figure 2.10(d, f), the FeS_2 NPs/VMS junction introduced the electronic potential barrier at the interface that blocked the photogenerated electrons back to the VMS layer and prevented the HER.

PEC measurements were carried out with a standard three-electrode configuration using a 0.5 M H_2SO_4 solution as the electrolyte. Figure 2.14(a) shows the photocurrent densities of the samples plotted as a function of potential vs. reversible hydrogen electrode (RHE) under a simulated air mass (AM) 1.5 G condition. The dark currents are shown as horizontal lines. The onset potential in the *J-V* curve was defined as the potential where the photocurrent density reaches -1 mA cm^{-2}. Even though Si is a promising candidate material for photocathodes because it has a narrow band gap, which enables effective absorption of a wide portion of the incident solar spectrum, the bare *p*-Si photocathode showed a large negative onset potential of -0.35 V. To drive HER on the *p*-Si photocathode, additional potential must be required because of the carrier concentration and kinetic overpotential issues.[42] The kinetic overpotential could be overcome by applying the PMS thin film catalyst on the *p*-Si photocathode, which shows the anodic shift in the polarization curve (Figure 2.14(a)). Compared with the PMS/*p*-Si photocathode, the onset potential of VMS/*p*-Si photocathode slightly enhanced to 125 mV. While the PMS exposes the catalytically inert basal planes as the terminating surface, VMS has the edge-terminated surface, which is the catalytic active site.[43] Therefore, the HER is more active on the VMS/*p*-Si photocathode than on the PMS/*p*-Si, and it leads to a lower onset potential for the HER. The catalytic activity of the metal precursor is extremely enhanced with the introduction of Ni because metallic Ni_3S_2 nanoparticles induce a downward band bending and the resultant built-in potential at the VMS/Ni_3S_2 interface, consequently facilitating the electron transfer to the electrolyte, as mentioned in Figure 2.10(c). Among the synthesized thin film catalysts/*p*-Si photocathodes, the

F1N9S/VMS/*p*-Si photocathode exhibited the highest catalytic activity for HER. The onset potentials of this photocathode markedly shifted toward the anodic direction to 280 mV, and the photocurrent density at 0 V was -25.4 mA cm^{-2}. This value is even higher than the maximum photocurrent density (24.6 mA cm^{-2}) of MoS_2/*p*-Si photocathodes in our previous study.[17] However, the cathodic shift in the onset potential is observed when the Fe ratio increases. This is because of the metal (Ni_3S_2) to semiconductor (FeS_2) transition of FNS NPs inducing the electronic potential barriers at the NPs/VMS interface. The incident-photon-to-current conversion efficiency (IPCE) spectra (Figure 2.14(b)) of the thin film catalysts/*p*-Si were recorded at an applied potential of 0 V vs. RHE. Among the synthesized thin films, the F1N9S/VMS thin film on the *p*-Si photocathode showed the highest efficiency of above 60% in the wavelength range of 400–800 nm. The IPCE increased until the Ni/Fe ratio reached 9, and IPCE decreased with the increased amount of Fe, corresponding to the photocurrent density at 0 V vs. RHE.

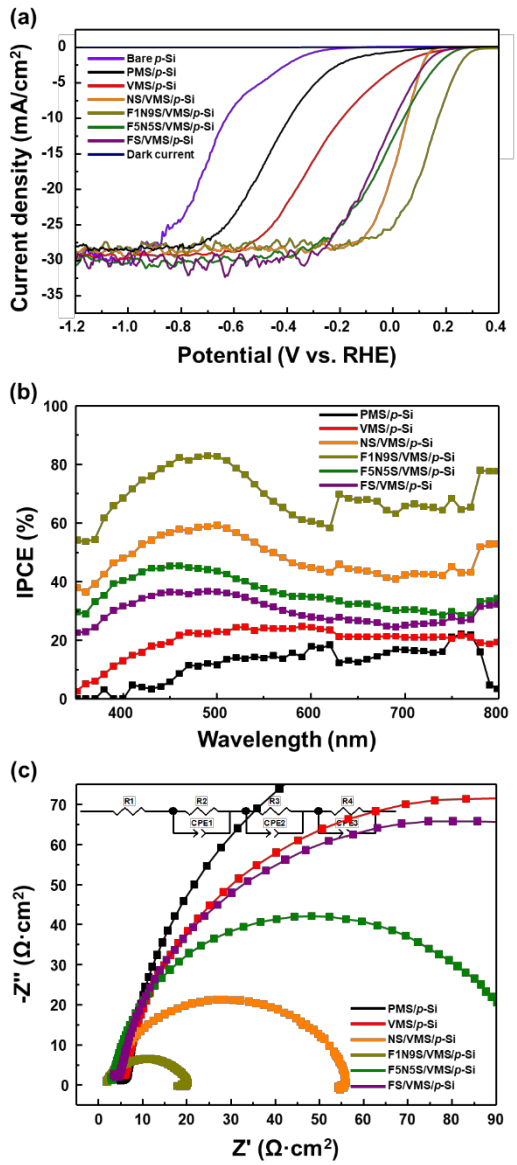

Figure 2.14. (a) Polarization curves of the synthesized photocathodes. (b) Incident photon-to-current efficiency (IPCE) measurement of the synthesized photocathodes. (c) Electrochemical impedance spectroscopy (EIS) analysis of the synthesized photocathodes at 0 V vs. RHE.

The electrochemical (EC) HER performance of the synthesized thin film catalysts with various Ni/Fe ratios with iR-correction in 0.5 M H_2SO_4 was investigated. For the electrochemical measurement, the synthesized thin films were transferred to the Au substrate. For comparison, we also plotted the linear sweep voltammetry (LSV) curve of the Pt electrode. As shown in Figure 2.15, the EC HER performance of the synthesized thin film showed the same trend as the PEC HER performance. The introduction of Ni causes significant enhancement of catalytic activity for the HER. The F1N9S/VMS thin film displays the highest catalytic activity also in electrochemical measurement, which is a low overpotential of 106 mV at a current density of 10 mA cm^{-2}, as shown in Figure 2.15(a). Furthermore, we displayed the Tafel plots of the samples in Figure 2.15(b). The reaction mechanism of HER can be explained by the Tafel slope, which involves three steps: discharge (Volmer reaction, Tafel slope of 120 mV dec^{-1}), desorption (Heyrovsky reaction, Tafel slope of 40 mV dec^{-1}) and recombination steps (Tafel reaction, Tafel slope of 30 mV dec^{-1}).[44] In Figure 2.15(b), the F1N9S/VMS on the Au electrode showed the lowest Tafel slope of 68.5 mV dec^{-1}. On this cathode, HER most likely occurs via the Volmer-Heyrovsky mechanism, which indicates that the rate-limiting step is the electrochemical desorption of H_{ads} and H_3O^+ to form hydrogen.[44] Considering that this catalyst has the form of a flat thin film, which has a much lower surface area than other nanostructured catalysts, this catalyst has a superior catalytic activity compared with the reported MoS_2-based catalysts, as shown in Table 2.2.

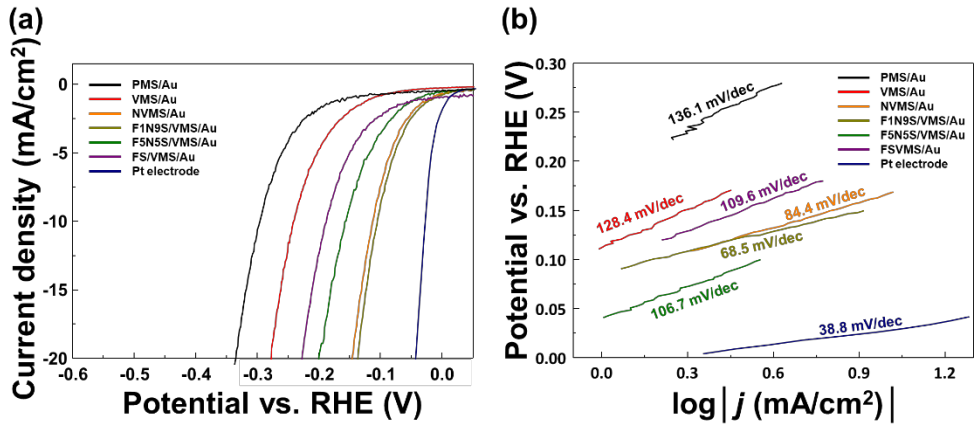

Figure 2.15. (a) The polarization curves of the synthesized thin films on Au electrode. (b) Tafel slopes of the synthesized thin films plotted as log (j) against potential *vs*. RHE

Table 2.2. Comparison of experimental results with previously reported transition metal sulfide catalysts.

Electrocatalyst	Type	Overpotential (mV) @ 10 mA cm^{-2}	Tafel slope (mV dec^{-1})	Ref	Electrolyte
F1N9S/VMS	Thin film	**106**	**68.5**	**This study**	**0.5 M H_2SO_4**
Defective-rich MoS_2		208	160	[45]	0.5 M H_2SO_4
Au nanorods on MoS_2 nanosheet		220	71	[46]	0.5 M H_2SO_4
Vertically aligned MoS_2 nanosheets with graphene		421	84	[47]	0.5 M H_2SO_4
Core-shell MoO_3-MoS_2 nanowires	Nanostructure	~175	~55	[48]	0.5 M H_2SO_4
Ni-Co-MoS_2 nanoboxes		155	51	[25]	0.5 M H_2SO_4
P, Se-co-doped MoS_2 nanosheets on CNTs		110	49	[49]	0.5 M H_2SO_4
MoS_2 nanosheets on TiN nanorods		146-195	44.8-65.6	[50]	0.5 M H_2SO_4
CoS_2-MoS_2/CNTs		70	67	[51]	0.5 M H_2SO_4
Co-doped MoS_2 nanosheets on Carbon		90	50	[52]	0.5 M H_2SO_4
Cu nanoparticle deposited MoS_2 nanoflowers on GO sheet		126	90	[53]	0.5 M H_2SO_4
N-doped Cu_2S/MoS_2 nanorod arrays		91	41	[54]	1 M KOH
Ni_xS_y-MoS_2 hybrid microspheres	Microstructure	~290	55.6	[55]	0.5 M H_2SO_4

Furthermore, electrochemical impedance spectroscopy (EIS) measurements using a simplified equivalent circuit were conducted to investigate the surface kinetics, as shown in Figure 2.14(c). The simplified equivalent circuit consisted of constant phase elements (CPE) and charge-transfer resistance (R_{ct}). The impedance spectra were measured at 0 V vs. RHE under the AM 1.5 G condition. The smallest semicircular arc showed in the F1N9S/VMS/*p*-Si thin film catalyst, which indicates that the electrode-to-electrolyte shuttling of electrons on this catalyst is faster when compared with the other catalysts. This notable decrease in the overall impedance is attributed to the appropriate bend bending and a built-in potential that formed at each junction (VMS/*p*-Si, F1N9S/VMS). The overall sizes of the semicircular arc for each synthesized photocathode correspond well with that of photocurrents at 0 V in Figure 2.14(a), as shown in Table 2.3. The charge-transfer resistance at the *p*-Si/MoS_2 interfaces ($R_{ct,1}$) showed a remarkable difference between the VMS and PMS layers on *p*-Si. This is because the vertically aligned domains in the VMS thin film act as conductive channels between *p*-Si and the electrolyte.[56] For the PMS thin film, the photoelectron should go through the out-of-plane direction of layered MoS_2, which has intrinsically low conductivity.[17] In addition, the $R_{ct,2}$ of the metal sulfide decorated VMS/*p*-Si photocathodes increased as the thickness of the Fe precursor layer increased. This tendency is due to FeS_2 NPs, which cause electron barriers and hinder the transfer of electrons, as mentioned earlier.

Table 2.3. Charge transport resistance of synthesized photocathodes.

***p*-Si photocathode**	R_s **(Ω cm^2)**	$R_{ct,1}$ **(Ω cm^2)**	$R_{ct,2}$ **(Ω cm^2)**	$R_{ct,3}$ **(Ω cm^2)**
PMS	2.10	161.50	143.69[a]	N/A
VMS	5.51	88.82	87.40[a]	N/A
NVMS	2.32	51.28	0.25	2.86
F1N9S/VMS	1.44	18.42	0.42	0.41
F5N5S/VMS	2.92	14.71	77.51	5.26
FS/VMS	4.32	55.84	113.42	0.55

R_s: The charge transport resistance at contact/*p*-Si.
$R_{ct,1}$: The charge transport resistance at *p*-Si/MoS_2.
$R_{ct,2}$: The charge transport resistance at MoS_2/FNS
$R_{ct,3}$: The charge transport resistance at FNS/electrolyte.
[a]: The charge transport resistance at MoS_2/electrolyte.

Chronoamperometric experiments were performed on PMS/*p*-Si, VMS/*p*-Si and F1N9S/VMS/*p*-Si photocathodes to evaluate the passivation effect of the synthesized thin film catalysts, as shown in Figure 2.16. For the PMS/*p*-Si photocathode, the current was improved for 30 min during the measurement. This is probably due to a self-optimizing effect by morphological changes (Figure 2.17), because the hydrogen gas that evolved between the MoS_2 layers caused exfoliation and fracture of the thin film and made it more porous.[57] Subsequently, the current gradually decreased to only 43% of the initial current after 10 h. This is attributed to the weak adhesion between PMS and Si via van der Waals force, resulting in the PMS layer further peeling off from silicon. It is also because MoS_2 is oxidized to oxide materials such as MoO_3, which are catalytically inactive for the hydrogen evolution reaction, thereby decreasing the number of catalytic active sites.[58] For VMS/*p*-Si, stability was improved more than that of the PMS/*p*-Si. It is believed that the edge-terminated surface of the VMS on silicon with the dangling bond at the edge site strengthened the adhesion to silicon and prevents its peeling off.[56] However, as on PMS, the oxidation of MoS_2 occurred on VMS and the performance deteriorated, leading to only 75% of the initial current remaining after 10 h.

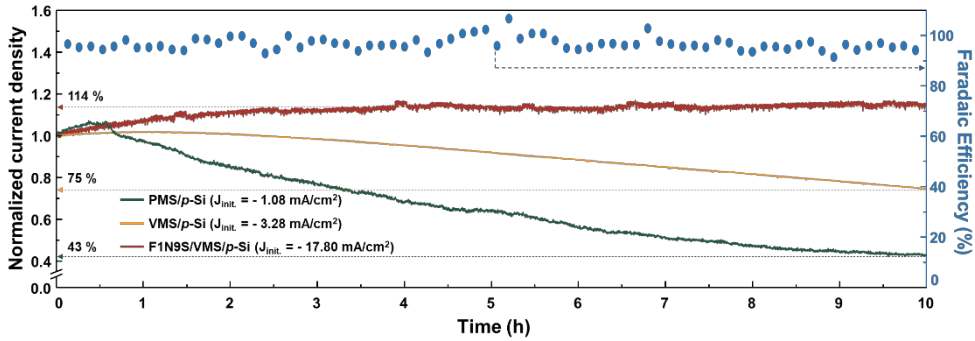

Figure 2. 16 . Hydrogen evolution and Faradaic efficiency vs. time for the TMD/*p*-Si heterostructure photocathodes to test stability for approximately 10 h.

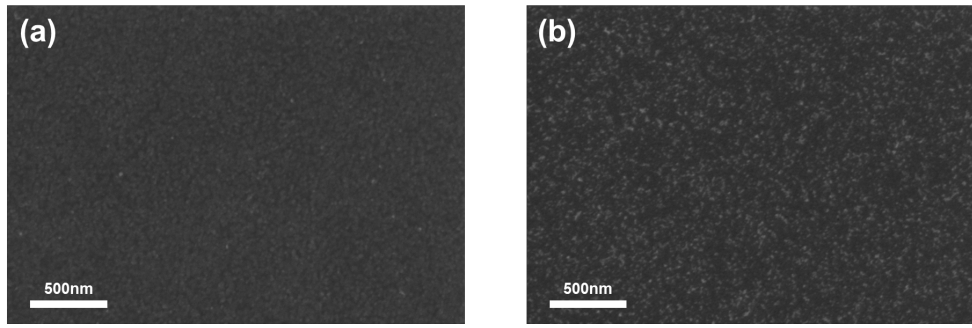

Figure 2.17. SEM images of PMS/*p*-Si photocathode (a) before and (b) after morphological changes.

For F1N9S/VMS/*p*-Si, highly stable performance was observed. No degradation in photocurrent was observed even after 10 h. This is attributed to the band structure, as shown in Figure 2.10(c). Because the photogenerated electrons are concentrated on metal sulfides with lower energy states than that of VMS, the oxidation of MoS_2 is suppressed. In this way, we can obtain high long-term stability, up to 10 h, due to the effect of vertically aligned MoS_2 and metal sulfide particles. Through the SEM, TEM, Raman spectra, XRD, and XPS analysis measured after the stability test shown in Figure 2.18-19, it was confirmed that there were no noticeable changes in the morphology and crystal structure of F1N9S/VMS/*p*-Si photocathode. The Ni_2FeS_4 phase, which was present in a very small amount before the stability test was not found in the TEM analysis conducted after the stability test. The Ni_2FeS_4 might have been reduced to the catalytically active Ni_3S_2, probably leading to the improved current density of the F1N9S/VMS/*p*-Si photocathode during operation. Furthermore, the Faradaic efficiency was measured by analyzing the gas evolved during the chronoamperometric experiment for the F1N9S/VMS/*p*-Si photocathode using gas chromatography to confirm if the current flowed on the photocathode was actually used for HER. As shown in Figure 2.16, the Faradaic efficiency was close to 100%, confirming that all the current flowing through the photocathode participated in HER.

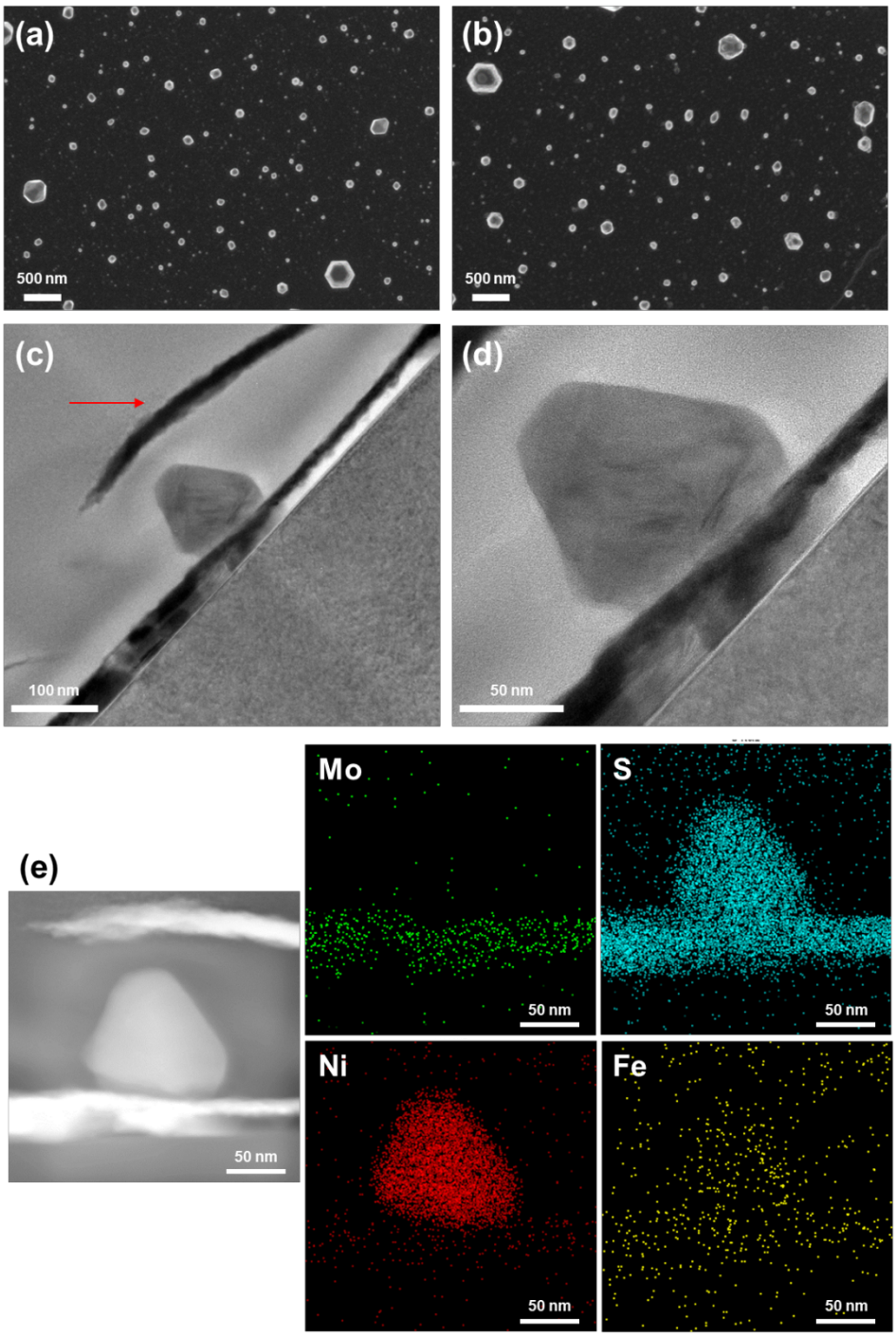

Figure 2.18. SEM images of F1N9S/VMS/*p*-Si photocathode (a) before and (b) after the stability test. (c-d) TEM images of the F1N9S/VMS/*p*-Si photocathode after the stability test. Red arrow: deposited Ga layer during TEM sample preparation using focused ion beam (FIB) instrument. (e) Cross-sectional HAADF-STEM image and EDS mapping of F1N9S/VMS/*p*-Si photocathode after the stability test.

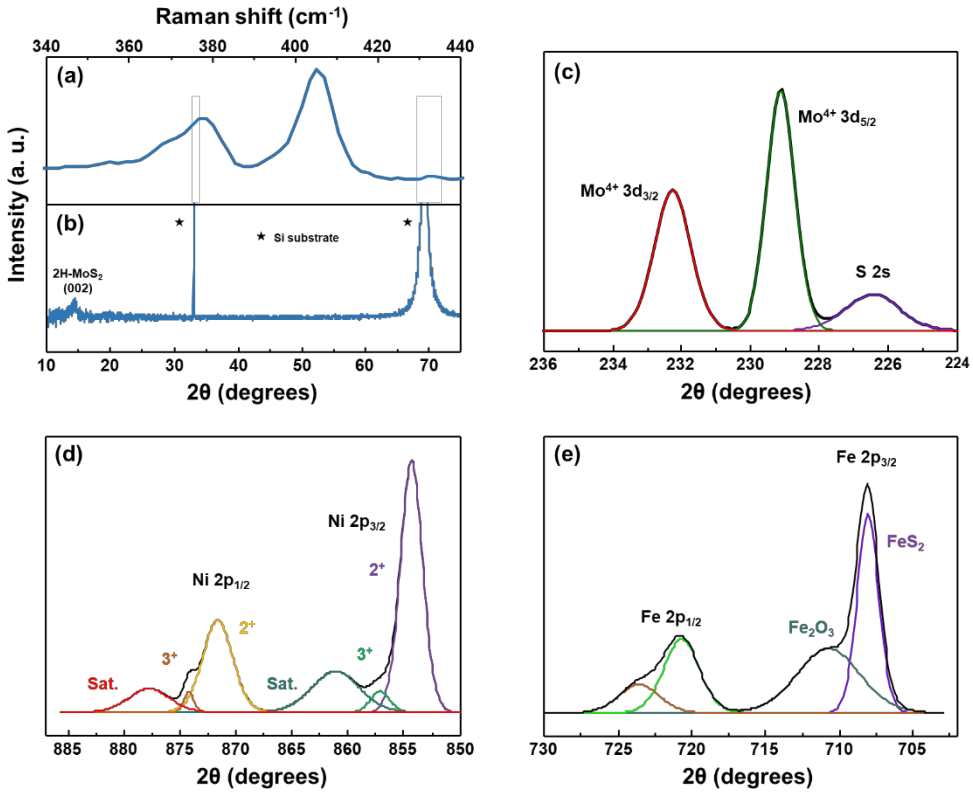

Figure 2. 19 . (a) Raman spectra and (b) XRD patterns of the F1N9S/VMS/*p*-Si photocathode after the stability test. XPS analysis of the F1N9S/VMS/*p*-Si photocathode after the stability test for (c) Mo 3*d*, (d) Ni 2*p*, and (e) Fe 2*p*.

In most photocathodes, the accumulation of photogenerated charge carriers could occur with a sufficient lifetime at both the heterointerface inside the photocathode and the electrolyte/photoelectrode interface. The PEC performance of the photoelectrode is determined by the competition between photogenerated charge transfer and recombination. Therefore, to investigate the kinetic behaviors of photogenerated charges at heterointerfaces, we conducted intensity modulated photocurrent spectroscopy (IMPS) by probing the periodic changes in the photocurrent in response to a sinusoidal intensity modulation of the incident light illumination.[59, 60] IMPS is a practical method to obtain the rate constants of charge transfer (k_{trans}) and recombination (k_{rec}) for photoelectrodes under constant applied bias. Figure 2.20(a) exhibits a Nyquist plot showing the complex photocurrent of PMS/*p*-Si, VMS/*p*-Si, NS/VMS/*p*-Si, F1N9S/VMS/*p*-Si, F5N5S/VMS/*p*-Si and FS/VMS/*p*-Si photocathodes resulting from light intensity modulation at 0 V vs. RHE. The charge transfer efficiency, defined as $k_{trans}/(k_{trans} + k_{rec})$, can be obtained from the ratio of the low frequency to high frequency intercepts on the real photocurrent axis. The apex of the semicircular arc, showing the maximum phase shift, indicates the combined rate constant of charge transfer and recombination ($k_{trans} + k_{rec}$). Therefore, k_{trans} and k_{rec} values can be calculated by using the intercept ratio on the real photocurrent axis and the frequency on the apex. The resulting k_{trans} and k_{rec} values of PMS/*p*-Si, VMS/*p*-Si, NS/VMS/*p*-Si, F1N9S/VMS/*p*-Si, F5N5S/VMS/*p*-Si and FS/VMS/*p*-Si photocathodes are summarized in Figure 2.20(b). It is worth noting that k_{trans} increased one order of magnitude for VMS/*p*-Si when compared with PMS/*p*-Si. This is another clear evidence that, when the photogenerated electrons are transported through MoS_2 thin film catalyst to the

electrolyte, it is significantly more efficient to pass through the vertically aligned domains of VMS than to hop layer by layer of PMS. Also, the k_{rec} value shows the minimum value at F1N9S/VMS/*p*-Si, the best sample, and increases rapidly as the proportion of Fe increases in the thin film catalyst. This is due to the formation of an electronic barrier on the F5N5S/VMS and FS/VMS interface with an increase in the Fe content, as shown in Figure 2.10(d and f).

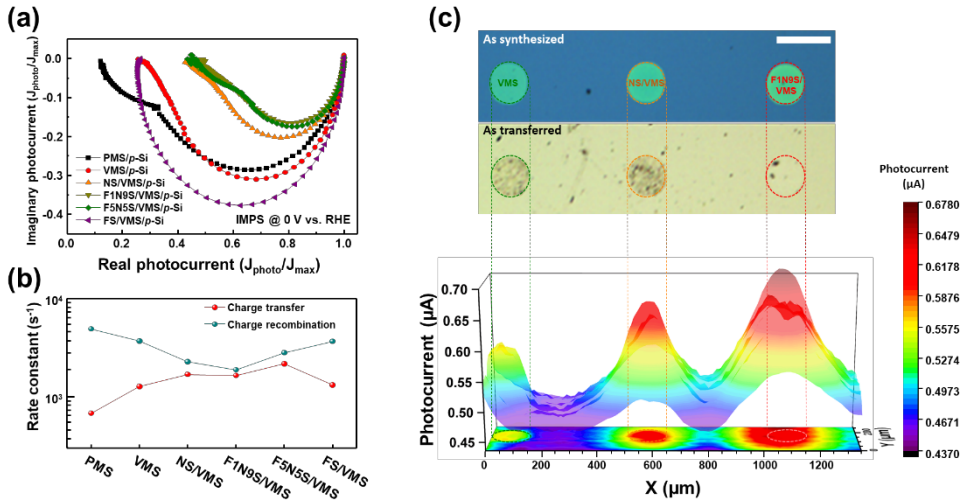

Figure 2.20. (a) IMPS Nyquist plot of fabricated photocathodes displaying the imaginary photocurrent vs. the normalized real photocurrent at 0 V vs. RHE. (b) Rate constants of charge transfer (k_{trans}) and recombination (k_{rec}) extracted from the IMPS Nyquist plot. (c) Optical image of as-synthesized patterned thin films and thin films transferred on *p*-Si with corresponding photocurrent mapping image of device at 0.1 V vs. RHE.

Spatially resolved PEC characterization was performed to directly evaluate and visualize the photocatalytic activity of the F1N9S/VMS with that of other catalysts on the same *p*-Si photocathode. SPECM is an in situ microscopic photocurrent mapping system combined with the standard three-electrode configuration in a home-designed reaction bath and a focused 532-nm laser by an optical objective (see Figure 2.21). While the focused laser scans over the catalyst area using a motorized microstage, the photocurrent corresponding to hydrogen generation is measured and mapped based on the position of the laser spot. The focused spot size is ~5.0 μm in diameter and the incident power is typically ~200 μW. Note that such an analysis allows us to investigate the photocatalytic activities on various catalytic surfaces without experimental sample-to-sample variations potentially existing in conventional PEC measurements.[61] For the SPECM measurement, we deposited Mo, Ni and Fe thin films using a patterning mask with 100 μm of holes through the e-beam evaporator deposition method, and sulfurized the thin films. The optical images of VMS, NS/VMS and F1N9S/VMS thin film catalysts on the SiO_2 and *p*-Si substrates are shown in Figure 2.20(c). We visualized the intensity of the photocurrent generated on each thin film catalyst into 3D mapping, as shown in Fig. 3.20(c). Based on previous PEC measurements, the intensity of the photocurrent of the F1N9S/VMS thin film catalyst on *p*-Si was the highest. It was confirmed that the photocurrent gradually decreased for NS/VMS and VMS thin film catalysts. Similarly, Figure 2.22(a) shows an optical image of the specially designed photocathode containing five spatially distinct regions, namely, F1N9S/VMS, NS/VMS, VMS, PMS and bare *p*-Si. The photocurrent mapping image and line profiles obtained at -0.1 V vs. RHE are shown in Figure 2.22(b-c), in which the

different catalytic surfaces are clearly distinguished in the photocurrent color map and line profiles. Compared with the photocurrent of ~0.84 μA on the bare *p*-Si area, the photocurrent values are increased by ~0.4, 0.3, 0.1 and 0.02 μA for F1N9S/VMS, NS/VMS, VMS and PMS on *p*-Si, respectively. This increasing trend in photocurrent based to various surface decorations is consistent with the above photocatalytic HER performances measured with typical PEC measurements. It is worth noting that a relatively higher photocurrent is observed from the edges of the transferred film presumably due to further catalytic enhancement by edges and local strains.

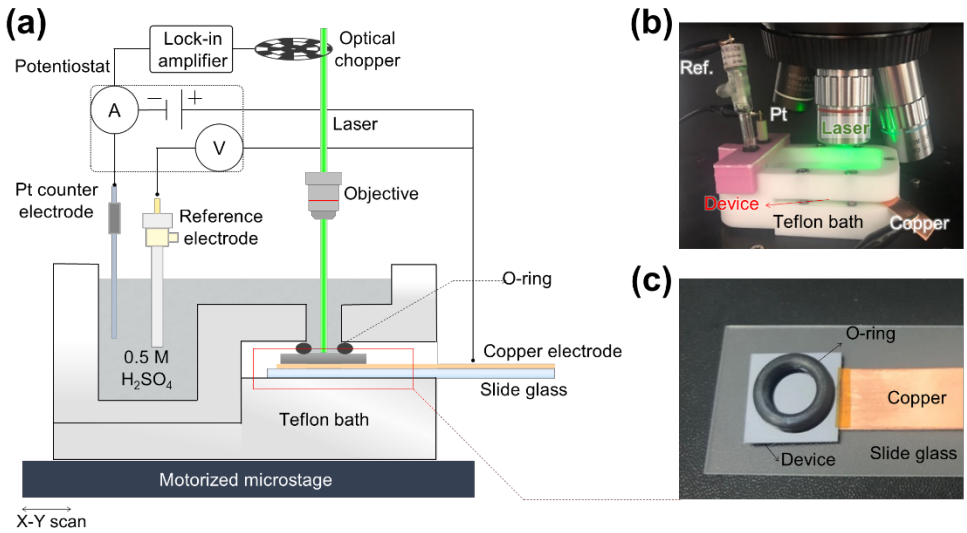

Figure 2. 21 . (a) Schematic of the SPECM measurement setup, combining scanning photocurrent microscopy with a standard three-electrode electrochemical measurement. A copper electrode contacting the device, Pt, and the saturated calomel electrode are used as the working, counter and reference electrodes, respectively. The home-designed reaction bath is illuminated by a 532-nm laser from above. (b) Photograph of the measurement with a 532-nm laser and mapping stage. (c) Photograph of the fabricated device on slide glass with O-ring. The device is electrically connected to a copper electrode through an InGa eutectic alloy and silver paste.

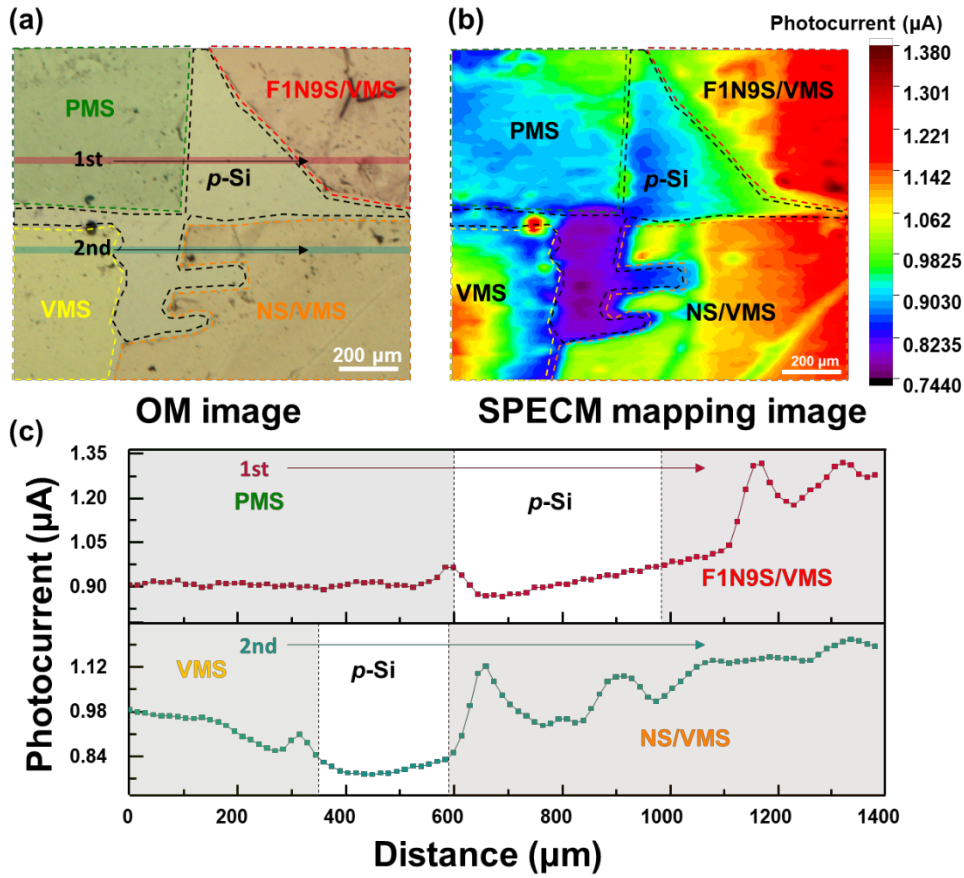

Figure 2.22. (a) Optical image of the fabricated device. (b) Photocurrent mapping image of the device at -0.1 V vs. RHE. Scale bars in (a) and (b) are 200 μm. (c) Corresponding line profiles of photocurrent along the solid lines in (a). Red (1st) and green (2nd) line profiles are obtained along the red (1st) and green (2nd) solid lines in (a), respectively. Red, green, orange and yellow shaded regions indicate F1N9S/VMS, PMS, NS/VMS and VMS, respectively.

Owing to the change in the domain orientation of MoS_2 and the atomic composition of 3D metal sulfide nanoparticles, we have suggested charge-transfer and surface degradation mechanisms. These are illustrated in Figure 2.10(e-f). As the downward band bending induced by F1N9S NPs enables rapid charge transfer along the out-of-plane direction of the thin film catalyst, the surface degradation of VMS is effectively suppressed over a 10 h operation. In contrast, as illustrated in Figure 2.10(f), the electronic barrier at the heterointerface of F5N5S/VMS and FS/VMS causes photogenerated electrons to accumulate at the heterointerface of 3D metal sulfide NPs/VMS, which is followed by rapid charge recombination. These results indicate that moderate amounts of Fe are beneficial for improving the electrocatalytic performance of thin film catalysts for HER, whereas excess Fe increases charge recombination at the 3D metal sulfide nanoparticles/VMS interface.

2.4. Conclusion

We have successfully demonstrated large scale (12 cm × 12 cm) and transferable FNS NPs decorated VMS thin film catalysts via one-step sulfurization method. The synthesized thin film catalyst exhibited remarkable PEC performance: high photocurrent density (25.44 mA cm^{-2} at 0 V vs. RHE), lower onset potential (280 mV at 1.0 mA cm^{-2}) and long-term stability (over 10 h). The heterojunction band diagram and DFT calculation further showed that the F1N9S NPs on VMS/*p*-Si photocathode not only induced the downward band bending of VMS but also improved the surface kinetics of the thin film catalyst. The proposed one-step sulfurization method paves a novel way for TMD-based 3D/2D heterojunctions, which were previously inaccessible in the form of large-scale transferable thin films. The 3D/2D heterojunction demonstrated here with conventional transition metal disulfides could also lead to the discovery of a new class of thin film materials with a versatile combination of both transition metals and chalcogen elements.

2.5. References

[1] G. Ingrosso, *Microchemical Journal* **2002**, *73*, 221.

[1] M. G. Walter, E. L. Warren, J. R. McKone, S. W. Boettcher, Q. Mi, E. A. Santori, N. S. Lewis, *Chemical Reviews* **2010**, 110, 6446.

[2] S. Hu, M. R. Shaner, J. A. Beardslee, M. Lichterman, B. S. Brunschwig, N. S. Lewis, *Science* **2014**, *344*, 1005.

[3] A. Paracchino, V. Laporte, K. Sivula, M. Grätzel, E. Thimsen, *Nature Materials* **2011**, *10*, 456.

[4] K. A. Brown, S. Dayal, X. Ai, G. Rumbles, P. W. King, *Journal of the American Chemical Society* **2010**, *132*, 9672.

[5] D. M. Andoshe, S. Choi, Y.-S. Shim, S. H. Lee, Y. Kim, C. W. Moon, D. H. Kim, S. Y. Lee, T. Kim, H. K. Park, M. G. Lee, J.-M. Jeon, K. T. Nam, M. Kim, J. K. Kim, J. Oh, H. W. Jang, *Journal of Materials Chemistry A* **2016**, *4*, 9477.

[6] C. Jiang, S. J. Moniz, A. Wang, T. Zhang, T. J. Tang, *Chemical Society Reviews* **2017**, *46*, 4645.

[7] J. Kye, M. Shin, B. Lim, J.-W. Jang, I. Oh, S. Hwang, *ACS Nano* **2013**, *7*, 6017.

[8] L. Zhu, H. Lin, Y. Li, F. Liao, Y. Lifshitz, M. Sheng, S.-T. Lee, M. Shao, *Nature Communications* **2016**, *7*, 1-7.

[9] X. Guo, P. Diao, D. Xu, S. Huang, Y. Yang, T. Jin, Q. Wu, M. Xiang, M. Zhang, *International Journal of Hydrogen Energy* **2014**, *39*, 7686.

[10] N. Takeno, Atlas of Eh-pH diagrams, Intercomparison of thermodynamic databases. (National Institute of Advanced Industrial Science and

Technology, Tokyo, 2005).

[11] K.-K. Liu, W. Zhang, Y.-H. Lee, Y.-C. Lin, M.-T. Chang, C.-Y. Su, C.-S. Chang, H. Li, Y. Shi, H. Zhang, *Nano Letters* **2012**, *12*, 1538.

[12] S. Z. Butler, S. M. Hollen, L. Cao, Y. Cui, J. A. Gupta, H. R. Gutiérrez, T. F. Heinz, S. S. Hong, J. Huang, A. F. Ismach, *ACS Nano* **2013**, *7*, 2898.

[13] D. Hu, J. Xiang, Q. Zhou, S. Su, Z. Zhang, X. Wang, M. Jin, L. Nian, R. Nözel, G. Zhou, *Nanoscale* **2018**, *10*, 3518.

[14] K. C. Kwon, S. Choi, J. Lee, K. Hong, W. Sohn, D. M. Andoshe, K. S. Choi, Y. Kim, S. Han, S. Y. Kim, H. W. Jang, *Journal of Materials Chemistry A* **2017**, *5*, 15534.

[15] Q. Ding, F. Meng, C. R. English, M. Cabán-Acevedo, M. J. Shearer, D. Liang, A. S. Daniel, R. J. Hamers, S. Jin, *Journal of the American Chemical Society* **2014**, *136*, 8504.

[16] S. Liu, L. Zhou, W. Zhang, J. Jin, X. Mu, S. Zhang, C. Chen, S. Mu, *Nanoscale* **2020**, *12*, 9943.

[17] K. C. Kwon, S. Choi, K. Hong, C. W. Moon, Y.-S. Shim, D. H. Kim, T. Kim, W. Sohn, J.-M. Jeon, C.-H. Lee, K. T. Nam, S. Han, S. Y. Kim, H. W. Jang, *Energy & Environmental Science* **2016**, *9*, 2240.

[18] I. S. Amiinu, Z. Pu, X. Liu, K. A. Owusu, H. G. R. Monestel, F. O. Boakye, H. Zhang, S. Mu, *Advanced Functional Materials* **2017**, *27*, 1702300.

[19] H. Li, Y. Li, A. Aljarb, Y. Shi, L.-J. Li, *Chemical Reviews* **2017**, *118*, 6134.

[20] X. Jia, Y. Zhao, G. Chen, L. Shang, R. Shi, X. Kang, G. I. Waterhouse, L. Z. Wu, C. H. Tung, T. Zhang, *Advanced Energy Materials* **2016**, *6*, 1502585.

[21] J. Liu, J. Wang, B. Zhang, Y. Ruan, L. Lv, X. Ji, K. Xu, L. Miao, J. Jiang,

ACS Applied Materials & Interfaces **2017**, *9*, 15364.

[22] X. Luo, P. Ji, P. Wang, R. Cheng, D. Chen, C. Lin, J. Zhang, J. He, Z. Shi, N. Li, *Advanced Energy Materials* **2020**, *10*, 1903891.

[23] P. Wang, H. He, Z. Pu, L. Chen, C. Zhang, Z. Wang, S. Mu, *Dalton Transactions* **2019**, *48*, 13466.

[24] J. Zhang, T. Wang, D. Pohl, B. Rellinghaus, R. Dong, S. Liu, X. Zhuang, X. Feng, *Angewandte Chemie* **2016**, *128*, 6814.

[25] X. Y. Yu, Y. Feng, Y. Jeon, B. Guan, X. W. Lou, U. Paik, *Advanced Materials* **2016**, *28*, 9006.

[26] Y. Yang, K. Zhang, H. Lin, X. Li, H. C. Chan, L. Yang, Q. Gao, *ACS Catalysis* **2017**, *7*, 2357.

[27] G. Kresse, J. Furthmüller, *Physical Review B* **1996**, *54*, 11169.

[28] J. P. Perdew, K. Burke, M. Ernzerhof, *Physical Review Letters* **1996**, *77*, 3865.

[29] Y. Wu, F. Li, W. Chen, Q. Xiang, Y. Ma, H. Zhu, P. Tao, C. Song, W. Shang, T. Deng, *Advanced Materials* **2018**, *30*, 1803151.

[30] Y. Zhan, Z. Liu, S. Najmaei, P. M. Ajayan, J. Lou, *Small* **2012**, *8*, 966.

[31] Y. Lee, J. Lee, H. Bark, I.-K. Oh, G. H. Ryu, Z. Lee, H. Kim, J. H. Cho, *Nanoscale* **2014**, *6*, 2821.

[32] H. Li, Q. Zhang, C. C. R. Yap, B. K. Tay, T. H. T. Edwin, A. Olivier, D. Baillargeat, *Advanced Functional Materials* **2012**, *22*, 1385.

[33] A. P. S. Gaur, S. Sahoo, M. Ahmadi, M. J.-F. Guinel, S. K. Gupta, R. Pandey, S. K. Dey, R. S. Katiyar, *The Journal of Physical Chemistry C* **2013**, *117*, 26262.

[34] N. Zhang, J. Lei, J. Xie, H. Huang, Y. Yu, *RSC Advances* **2017**, *7*, 46286.

[35] W. Qiu, J. Xia, H. Zhong, S. He, S. Lai, L. Chen, *Electrochimica Acta* **2014**, *137*, 197.

[36] H.-H. Fan, H.-H. Li, K.-C. Huang, C.-Y. Fan, X.-Y. Zhang, X.-L. Wu, J.-P. Zhang, *ACS Applied Materials& Interfaces* **2017**, *9*, 10708.

[37] H. Wang, Z. Lu, S. Xu, D. Kong, J. J. Cha, G. Zheng, P.-C. Hsu, K. Yan, D. Bradshaw, F. B. Prinz, Y. Cui, *Proceedings of the National Academy of Sciences* **2013**, *110*, 19701.

[38] G. Wang, J. Zhang, S. Yang, F. Wang, X. Zhuang, K. Müllen, X. Feng, *Advanced Energy Materials* **2018**, *8*, 1702254.

[39] M. A. Islam, J. Church, C. Han, H.-S. Chung, E. Ji, J. H. Kim, *Scientific reports* **2017**, *7*, 1.

[40] T. A. Ho, C. Bae, H. Nam, E. Kim, S.-Y. Lee, J. H. Park, H. Shin, *ACS Applied Materials & Interfaces* **2018**, *10*, 12807.

[41] L. Wu, N. Y. Dzade, L. Gao, D. O. Scanlon, Z. Öztürk, N. Hollingsworth, B. M. Weckhuysen, E. J. Hensen, N. H. De Leeuw, J. P. Hofmann, *Advanced Materials* **2016**, *28*, 9602.

[42] D. M. Andoshe, J.-M. Jeon, S. Y. Kim, H. W. Jang, *Electronic Materials Letters* **2015**, *11*, 323.

[43] D. Kong, H. Wang, J. J. Cha, M. Pasta, K. J. Koski, J. Yao, Y. Cui, *Nano Letters* **2013**, *13*, 1341.

[44] J. D. Benck, T. R. Hellstern, J. Kibsgaard, P. Chakthranont, T. F. Jaramillo, *ACS Catalysis* **2014**, *4*, 3957.

[45] Y. Li, K. Yin, L. Wang, X. Lu, Y. Zhang, Y. Liu, D. Yan, Y. Song, S. Luo,

Applied Catalysis B: Environmental **2018**, *239*, 537.

[46] Y. Shi, J. Wang, C. Wang, T.-T. Zhai, W.-J. Bao, J.-J. Xu, X.-H. Xia, H.-Y. Chen, *Journal of the American Chemical Society* **2015**, *137*, 7365.

[47] P. Gnanasekar, D. Periyanagounder, J. Kulandaivel, *Nanoscale* **2019**, *11*, 2439.

[48] Z. Chen, D. Cummins, B. N. Reinecke, E. Clark, M. K. Sunkara, T. F. Jaramillo, *Nano Letters* **2011**, *11*, 4168.

[49] T. Zhu, J. Ding, Q. Shao, Y. Qian, X. Huang, *ChemCatChem* **2019**, *11*, 689.

[50] M. Yu, S. Zhao, H. Feng, L. Hu, X. Zhang, Y. Zeng, Y. Tong, X. Lu, *ACS Energy Letters* **2017**, *2*, 1862.

[51] Y.-R. Liu, W.-H. Hu, X. Li, B. Dong, X. Shang, G.-Q. Han, Y.-M. Chai, Y.-Q. Liu, C.-G. Liu, *Applied Surface Science* **2016**, *384*, 51.

[52] X. Dai, K. Du, Z. Li, M. Liu, Y. Ma, H. Sun, X. Zhang, Y. Yang, *ACS Applied Materials& Interfaces* **2015**, *7*, 27242.

[53] F. Li, L. Zhang, J. Li, X. Lin, X. Li, Y. Fang, J. Huang, W. Li, M. Tian, J. Jin, R. Li, *Journal of Power Sources* **2015**, *292*, 15.

[54] X. Wang, J. Wang, X. Zhang, Q. Tian, M. Liu, N. Cai, Y. Xue, W. Chen, W. Li, F. Yu, *ChemCatChem* **2019**, *11*, 1354.

[55] W. Cui, C. Ge, Z. Xing, A.M. Asiri, X. Sun, *Electrochimica Acta* **2014**, *137*, 504.

[56] Z. Zhang, W. Li, M. F. Yuen, T.-W. Ng, Y. Tang, C.-S. Lee, X. Chen, W. Zhang, *Nano Energy* **2015**, *18*, 196.

[57] Y. Liu, J. Wu, K. P. Hackenberg, J. Zhang, Y. M. Wang, Y. Yang, K. Keyshar, J. Gu, T. Ogitsu, R. Vajtai, J. Lou, P. M. Ajayan, B. C. Wood, B. I.

Yakobson, *Nature Energy* **2017**, *2*, 1.

[58] Y. Li, Y. Yu, Y. Huang, R. A. Nielsen, W. A. Goddard III, Y. Li, L. Cao, *ACS Catalysis* **2015**, *5*, 448.

[59] J. E. Thorne, J.-W. Jang, E. Y. Liu, D. Wang, *Chemical Science* **2016**, *7*, 3347.

[60] J. E. Thorne, Y. Zhao, D. He, S. Fan, S. Vanka, Z. Mi, D. Wang, *Physical Chemistry Chemical Physics* **2017**, *19*, 29653.

[61] J. Y. Lee, S. Kang, D. Lee, S. Choi, S. Yang, K. Kim, Y. S. Kim, K. C. Kwon, S. H. Choi, S. M. Kim, J. Kim, J. Park, H. Park, W. Huh, H. S. Kang, S. W. Lee, H.-G. Park, M. J. Ko, H. Cheng, S. Han, H. W. Jang, C.-H. Lee, *Nano Energy* **2019**, *65*, 104053.

Chapter 3

CO_2 utilization on

3D nanostructured Ag catalysts

3.1. Introduction

The uncontrollable increase of CO_2 in the atmosphere by the excessive consumption of fossil fuels has become an urgent environmental issue in the world, as it has been considered a primary cause of global warming.[1-4] Because of this reason, the conversion of CO_2 to useful low carbon fuels has attracted considerable research interest.[5-7] Among the various methods, photoelectrochemical (PEC) reduction of CO_2 has been regarded as a promising strategy, because it utilizes the solar energy and water to reduce CO_2, which mimics natural photosynthesis.[8, 9] Depending on the catalysts and conditions, diverse chemicals such as carbon monoxide, formic acid, or hydrocarbons can be produced.[10-15] In aqueous electrolytes, the competitive hydrogen evolution reaction, which produces hydrogen gas, may occur together with the CO_2 reduction reaction. Therefore, syngas (synthesis gas, CO and H_2 mixtures) can be obtained in aqueous electrolytes, which is a critical C1 feedstock for practical applications including Fischer-Tropsch synthesis, methanol synthesis, syngas fermentation.[16, 17]

In the PEC system, many kinds of semiconductors, such as Si, oxide, nitride, and sulfide, have been studied for high efficient PEC CO_2 reduction reactions.[8, 18-23] Among the semiconductors, *p*-Si has been known as one of the most promising materials for photocathodes because of its narrow bandgap of 1.1 eV, earth abundance, and high-level processing technique. However, unfortunately, since the catalytic activity of Si for CO_2 reduction reaction is poor a high over-potential is needed to reduce CO_2 on Si photocathodes.[18, 24] Therefore, for high efficient syngas production using Si photocathode, catalysts that have high catalytic activity for CO_2 reduction reaction are essential. Metals such as Au and Ag have been

known to promote the conversion of CO_2 to CO by electrochemical reduction in aqueous electrolytes.[11, 25-27] Furthermore, the catalytic activity of these metals varies depending on the size of catalysts, morphology, crystallinity, oxidation states of metal catalysts.[11, 28-31] Especially, Kanan group firstly demonstrated the enhancement of catalytic activity for CO_2 reduction reaction of metal catalysts by tuning the nanostructure and the oxidation states of metals through electrochemical reduction of metal oxides in 2012.[11, 32-33] The oxide derived Au electrode exhibited remarkable performances, a very low over-potential of 140 mV, and high selectivity for CO production of 98%. However, although Au electrodes have better catalytic activity than Ag electrodes, their application on the industrial scale is difficult because of the high cost of Au metal. For this reason, many kinds of electrochemical treatments on Ag electrodes have been studied as replacement of Au electrodes, such as oxide-derived Ag,[34] Ag_2CO_3-derived Ag,[35-36] AgCl-derived Ag,[37] and AgBr-derived Ag.[38] With these Ag catalysts, efficient and low-cost PEC CO_2 reduction to syngas using Si photocathodes could be realized. However, because Ag catalysts inhibit the light absorption onto Si photocathode, there is a trade-off between the selectivity for CO and the light absorption. Therefore, an appropriate structure for photocathodes is needed.[8, 18]

In this chapter, we demonstrate the enhancement of Ag catalysts by reducing anodic (RA) treatment applied on *p*-Si photocathodes for efficient PEC CO_2 reduction to produce syngas in aqueous electrolyte. Through the RA treatment, the properties of Ag catalysts, such as morphology, active sites, and electronic structure, are tuned to achieve high catalytic activity for the CO_2 reduction reaction. Furthermore, we propose a new structure for photocathode using SiO_2 patterning,

which balances between the catalytic activity for CO_2 reduction reaction and light absorption onto Si photocathode. Figure 3.1(a) shows the schematic of the proposed photoelectrochemical reduction of CO_2 into syngas on the reduced Ag (R-Ag)/TiO_2/*p*-Si photocathode. The R-Ag/TiO_2/*p*-Si photocathode provides a low onset potential of -0.16 V vs. RHE (reversible hydrogen electrode), a large saturated photocurrent density of -9 mA/cm^2 at -1.23 V vs. RHE. Finally, the syngas in ratio from 1:1 to 1:3 that can be used to practical application is produced depending on the various applied potentials.

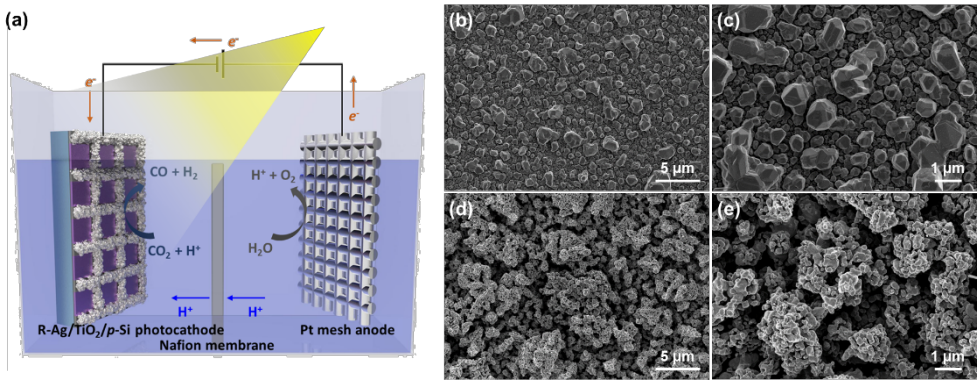

Figure 3.1. (a) Schematic of the proposed photoelectrochemical reduction of CO_2 into syngas on R-Ag/TiO_2/*p*-Si photocathode. Scanning electron microscopic (SEM) images of (b,c) Ag catalysts on TiO_2/*p*-Si photocathode and (d,e) R-Ag catalysts on TiO_2/*p*-Si photocathode.

3.2. Experimental procedures

Fabrication of Ag/TiO2/p-Si and SiO2 patterned Ag/TiO2/p-Si photocathode. A *p*-Si wafer (0.01-0.1 Ω-m, <100> plane, DASOMRMS Co., Ltd) was cleaned in acetone, isopropyl alcohol, and deionized (DI) water, using ultrasonication. The water was purified by a water purification system (Human Power, Human Co, Ltd., 183 KΩ-m) for DI water. The cleaned *p*-Si wafer was soaked for 1 min in 5% hydrofluoric acid (HF) to etch the native SiO_2 layers. Then a 5 nm-thick TiO_2 thin film was deposited using an electron-beam evaporator (KVE-E2004L). Subsequent heat treatment was conducted for TiO_2/*p*-Si substrates in a tube furnace at 350 °C for 30 min under N_2. For SiO_2 patterned Ag/TiO_2/*p*-Si photocathode, after deposition of TiO_2 thin film, a patterned 500 nm-thick SiO_2 was deposited using the electron-beam evaporator, using a patterning mask (Figure 3.2(a)). The patterning mask has square holes of 500 μm in length, and their total area is 50% of the total area of the mask. Before the electrodeposition, a Cu wire was connected to the scratched backside of the TiO_2/*p*-Si substrate using an In-Ga alloy (Sigma Aldrich) and silver paste. Then, except for the active area of 1 cm × 1 cm, the whole surface of the TiO_2/*p*-Si surface was covered with an adhesive Kapton tape to preven contact with the electrolyte.

The solution for the deposition of Ag is prepared from 5 mM $AgNO_3$, 50 mM $NaNO_3$, which were dissolved in DI water. The Ag catalysts were electrodeposited on the TiO_2/*p*-Si electrodes in a standard three-electrode system with a Pt mesh as a counter electrode and Ag/AgCl (*sat*. KCl) as a reference electrode. The deposition of Ag was performed by applying -0.1 V vs. Ag/AgCl on the working electrode for 15 min. Then, the electrodeposited samples were rinsed with DI water.

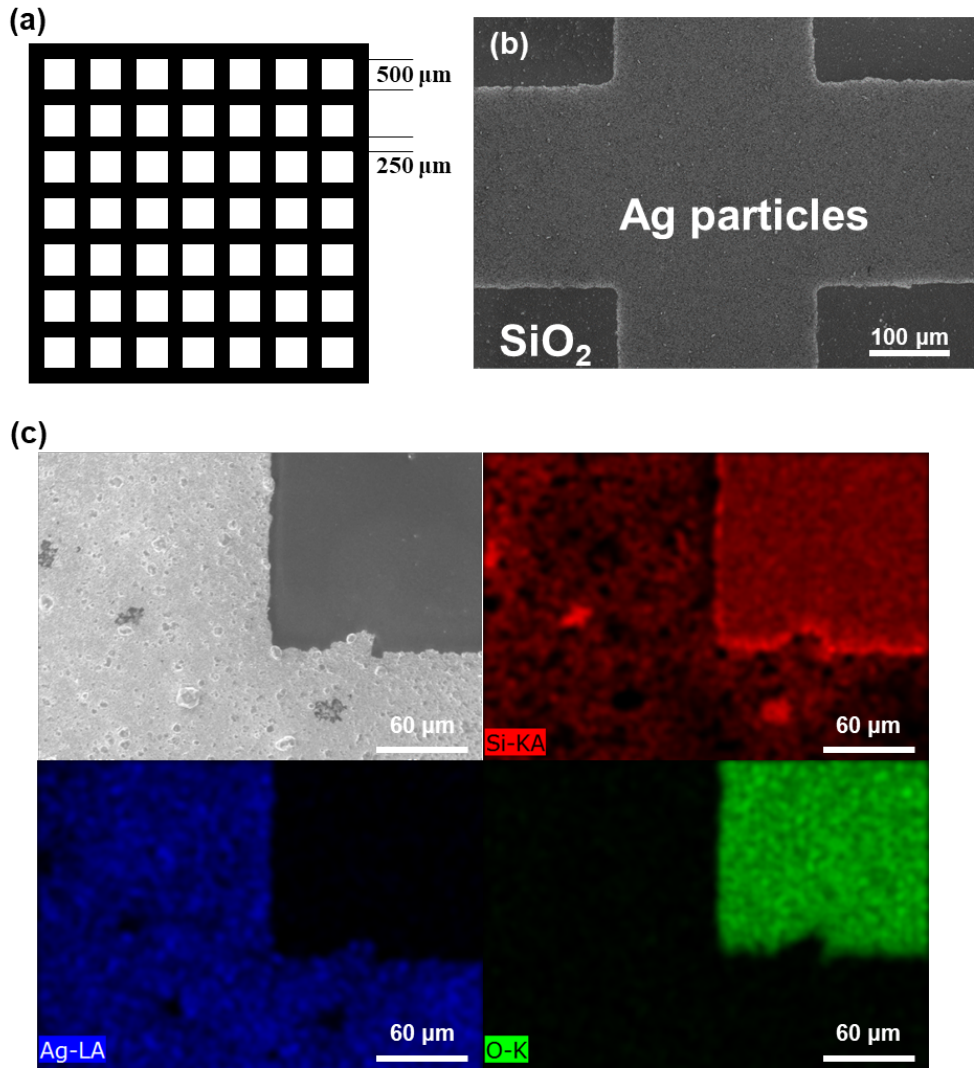

Figure 3.2. (a) Patterning mask used for deposition of SiO_2 layer. (b-c) SEM images and EDS spectrum of partially electrodeposited Ag particles on SiO_2-free region on Ag/TiO_2/*p*-Si photocathode.

RA treatment for R-Ag/TiO_2/*p*-Si and SiO_2 patterned R-Ag/TiO_2/*p*-Si photocathode. The RA treatment was performed on (SiO_2 patterned) Ag/TiO_2/*p*-Si photocathodes in CO_2-saturated 0.1 M $KHCO_3$ electrolyte (pH 6.7) in a two-compartment H-type electrochemical cell with a Pt mesh counter electrode and an Ag/AgCl (*sat*. KCl) reference electrode. Symmetric 50 Hz square-wave pulses between 1.3 V and 0.1 V were applied for 60 min. After pulsed anodization, the reduction of Ag catalysts was conducted at -0.6 V vs. RHE for 10 min.

Characterization. The morphology of the fabricated photocathodes was studied using FE-SEM (SUPRA 55VP), with an acceleration voltage of 2 kV and the working distance of 3.5 mm. The structural study of Ag and R-Ag on a TiO_2/*p*-Si photocathode was confirmed by a Bruker D8 advance diffractometer, equipped with a Cu Kα source. XPS analysis was carried out using an instrument (SIGMA PROBE ThermoFisher Scientific) at a base pressure of 5×10^{-10} mbar at 300K using monochromatic Al Kα radiation (1486.6 eV) generated from an electron beam operated at 15 kV. The binding energy (BE) scale was calibrated with the C 1*s* peak being at 284.5 eV. The spot size was about 400 μm.

Electrochemical measurement. The PEC measurements (Ivium Technologies, Nstat) were carried out with a three-electrode system with a Pt mesh as a counter electrode and an Ag/AgCl (*sat*. KCl) reference electrode in a CO_2 saturated $KHCO_3$ electrolyte. All measurements are conducted in the two-compartment H-type electrochemical cell with a piece of proton exchange membrane (Nafion® 117) as the separator. Before measurement, the electrolytes in the H-type cell were purged with CO_2 gas for at least 30 min. A Xe arc lamp used as a light source was

calibrated to 1 sun (100 mW/cm^2, AM 1.5G) using a reference photodiode. For the linear sweep with a cathodic direction, a scan rate of 20 mV/s was used. The measured current density was normalized to the electrode geometrical area. The measured potential vs. Ag/AgCl was converted to the RHE scale according to the Nernst equation:

$$E_{RHE} = E_{Ag/AgCl} + 0.059 \times pH + E^{0}_{Ag/AgCl} \quad \text{--- (1)}$$

where E_{RHE} is the potential vs. RHE, $E^0_{Ag/AgCl}$ = 0.198 V at 25 °C, and $E_{Ag/AgCl}$ is the measured potential vs. the Ag/AgCl reference electrode.

The evolved gas was analyzed using gas chromatography (Agilent GC 7890B) connected to the cathodic compartment of H-type electrochemical cell while a constant potential was applied. A 20.0 sccm rate of CO_2 gas was delivered into the cathodic compartment and vented into the gas sampling loop of the GC. The GC was equipped with a micropacked column (ShinCarbon ST 100/120), a thermal conductivity detector (TCD), and a flame ionization detector (FID), with argon as the carrier gas. The Faradaic efficiency was calculated according to the following equations:

$$j_{CO} = \frac{peak\ area\ of\ CO}{\alpha} \times flow\ rate \times \frac{2Fp_0}{RT} \times (electrode\ area)^{-1} \quad \text{--- (2)}$$

$$j_{H_2} = \frac{peak\ area\ of\ CO}{\beta} \times flow\ rate \times \frac{2Fp_0}{RT} \times (electrode\ area)^{-1} \quad \text{--- (3)}$$

$$F.E._{CO} = j_{CO}/j_{measured} \quad \text{---(4)}$$

$$F.E._{H_2} = j_{H_2}/j_{measured} \quad \text{---(5)}$$

where α and β are conversion factors for CO and H_2 respectively based on calibrations of the GC with a standard sample, p_0 = 101.325 kPa, and T = 298.15 K.

To compare the electrochemical surface area, double layer capacitance of R-Ag and Ag catalysts was measured on TiO_2/*p*-Si substrate in 0.1 M $KHCO_3$ electrolytes according to previously published method.[39] The charging current was measured from the CVs at different scan rates (10 – 100 mV s^{-1}). The relation between the double layer capacitance, the charging current, and the scan rate was given eq 6.

$$i_c = vC_{DL} \quad \text{---(6)}$$

Where i_c, v, and C_{DL} are charging current, scan rate, and double layer capacitance, respectively.

3.3. Results and discussion

The Ag/TiO_2/*p*-Si photocathode is synthesized by using the combination of electron-beam deposition and electrodeposition method. At first, a TiO_2 thin-film was deposited on *p*-Si substrate with 5 nm thickness using an electron-beam evaporator. The obtained TiO_2/*p*-Si substrate was annealed in a tube furnace at 350 °C for 30 min under N_2 atmosphere. After that, Ag catalysts are deposited on the TiO_2/*p*-Si substrate through the electrodeposition method. For the fabrication of R-Ag/TiO_2/*p*-Si, electrochemical RA treatment was conducted on the Ag/TiO_2/*p*-Si substrate. A Field-emission scanning electron microscopy (FE-SEM) was conducted to investigate the surface morphology changes induced by the RA treatment. Figure 3.1(b-e) shows the SEM images of fabricated Ag/TiO_2/*p*-Si photocathode and R-Ag/TiO_2/*p*-Si photocathode. Figure 3.1(b-c) shows the morphology of Ag/TiO_2/*p*-Si photocathode, which presented Ag particles of several hundred nanometers to micrometers in size have polygonal shapes. After pulsed anodization, the particles are merged into bigger particles randomly shaped (Figure 3.3). However, as shown in Figure 3.1(d-e), the reduction of Ag particles turned the Ag particles to change into the porous-like nanostructures on R-Ag/TiO_2/*p*-Si photocathode. Compared with the Ag/TiO_2/*p*-Si photocathode, the surface area of R-Ag/TiO_2/*p*-Si photocathode was enlarged, and the flat surface of Ag particles was changed into the rough surface. To estimate the change of surface area, the double layer capacitance (C_{dl}) at the solid/liquid interface for R-Ag/TiO_2/*p*-Si and Ag/TiO_2/*p*-Si photocathodes was measured by the cyclic voltammetry technique using different scan rates as shown in Figure 3.4(a-b). Figure 3.4(c) displays that R-Ag/TiO_2/*p*-Si photocathode exhibited a higher C_{dl} of

0.18 mF cm^{-2} than the Ag/TiO_2/*p*-Si photocathode of 0.018 mF cm^{-2}, indicating that more active surface area has increased through the RA treatment.

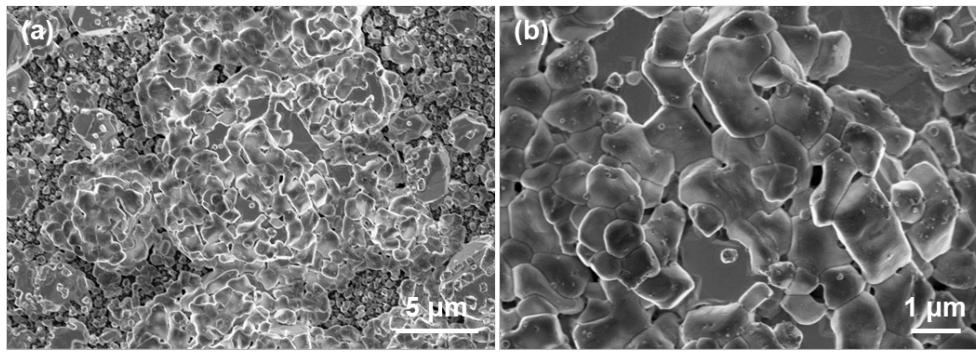

Figure 3.3 . Scanning electron microscopic (SEM) images of anodized Ag catalysts on TiO_2/*p*-Si photocathodes in (a) low and (b) high magnification.

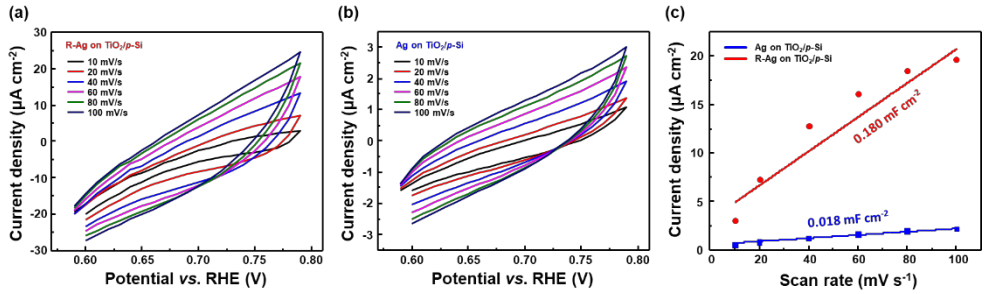

Figure 3.4. CV curves for (a) R-Ag/TiO_2/*p*-Si and (b) Ag/TiO_2/*p*-Si photocathodes at scan rate of 10, 20, 40, 60, 80, and 100 mV s^{-1} in 0.1 M $KHCO_3$ electrolytes. (c) Corresponding capacitive currents at 0.7 V vs. RHE plotted against the scan rate for R-Ag/TiO_2/*p*-Si and Ag/TiO_2/*p*-Si photocathodes.

To investigate the changes of the crystalline structure after RA treatment, the Ag/TiO_2/*p*-Si photocathode and the R-Ag/TiO_2/*p*-Si photocathode were analyzed by X-ray diffraction (XRD). Figure 3.5(a) displays the XRD patterns of the Ag and R-Ag catalysts on TiO_2/*p*-Si photocathodes. XRD patterns for these two photocathodes show 2θ reflection peaks at 38.2°, 44.5°, 64.5°, and 77.5° which all correspond to diffractions along the (111), (200), (220), and (311) planes of the face-centered cubic Ag crystal structure. The Ag/TiO_2/*p*-Si photocathode has the intense (111) peak, suggesting a preferred crystal orientation. However, XRD patterns for R-Ag/TiO_2/*p*-Si photocathode became more randomly powder-like Ag reference peaks with relative increase of (200), (220), and (311) peaks compared to the Ag/TiO_2/*p*-Si photocathode. Therefore, it was confirmed that not only the morphology was changed but also the crystallinity of the Ag catalysts through RA treatment. Previously, the catalytic activity for electrochemical CO_2 reduction to CO was higher on the (110) plane than on (111) or (100) planes, because of higher density of undercoordinated active sites.[31, 40] For face-centered cubic structures, (110) plane cannot be observable in XRD patterns because the (110) reflection does not occur. Assuming that the amount of the (110) plane exists in proportion to that of the (220) plane, it can be deduced that the amount of the (110) plane is increased in the R-Ag/TiO_2/*p*-Si photocathode after RA treatment. Therefore, it is expected that the electrochemical reduction of CO_2 efficiency can be enhanced by RA treatment due to increase of the active sites on (220) planes.

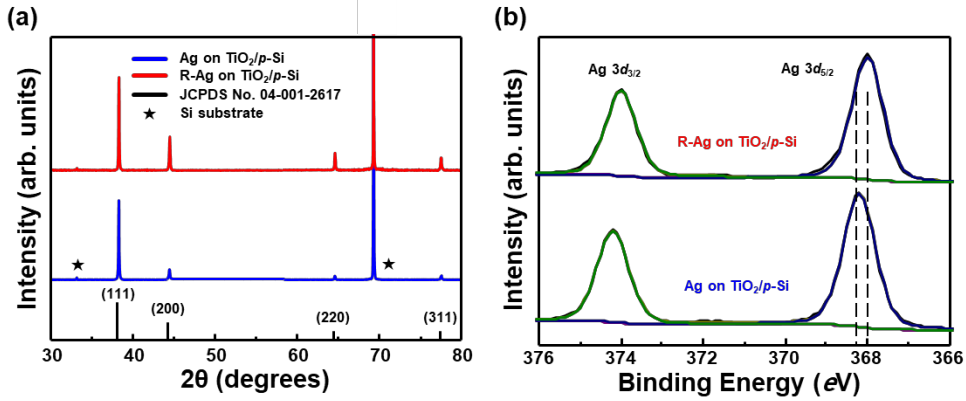

Figure 3.5. Characterization of Ag and R-Ag catalysts on TiO_2/*p*-Si photocathodes. (a) XRD patterns and (b) XPS spectrum of the Ag catalysts (blue) and R-Ag catalysts (red) on TiO_2/*p*-Si photocathode.

Furthermore, the electronic structures of the Ag and R-Ag on TiO_2/*p*-Si photocathode were analyzed through X-ray photoelectron spectroscopy (XPS). XPS survey spectra for Ag and R-Ag on TiO_2/*p*-Si photocathode was shown in Figure 3.6. In Figure 3.5(b), for Ag/TiO_2/*p*-Si photocathode, the Ag $3d_{5/2}$ peak and Ag $3d_{3/2}$ peak were observed at 368.2 eV and 374.2 eV, respectively. Also, R-Ag/TiO_2/*p*-Si photocathode has Ag 3*d* peaks at 368 eV and 374 eV, which are assigned to Ag $3d_{5/2}$ and Ag $3d_{3/2}$ peaks, respectively. The Ag 3*d* peaks could be deconvoluted into one main peak, which shows there is only metallic Ag. However, the Ag 3*d* peaks of R-Ag/TiO_2/*p*-Si photocathode were slightly shifted to lower binding energy than that of the Ag/TiO_2/*p*-Si photocathode. The negative shifts of core-level binding energy are induced by increased electron density on the Ag surface by intermetallic electron transfer, which is reported to improve the catalytic activity for electrochemical CO_2 reduction to CO on Ag catalysts.[36, 41] Rodriguez and co-worker have shown that a decrease in core-level binding energy cause strong chemisorption of CO because the high electron density of host metal facilitates π-backdonation into adsorbed CO.[42] As a result, the negative shift in core-level binding energy stabilizes the most important reaction intermediate ($COOH^*$) on Ag catalysts due to the scaling relation. Therefore, due to the downshift of the binding energy by the RA treatment, the performance improvement of electrochemical CO_2 reduction to CO can occur on the R-Ag catalysts compared to Ag catalysts on TiO_2/*p*-Si photocathodes.

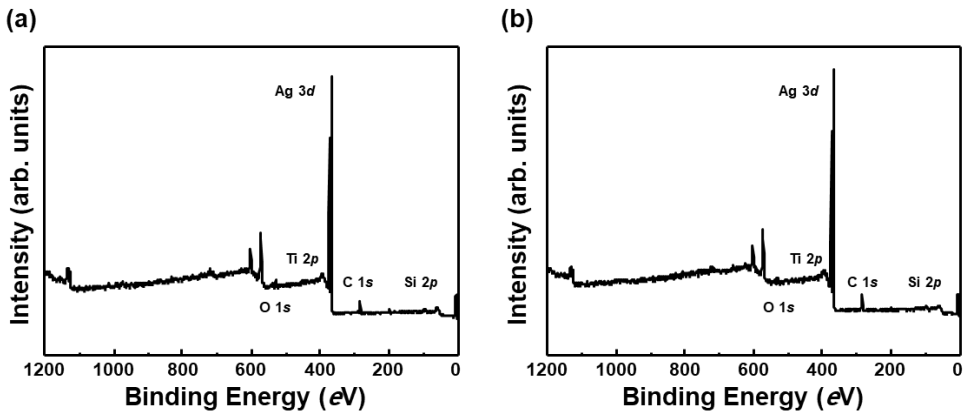

Figure 3. 6 . XPS survey spectrum for (a) Ag/TiO_2/*p*-Si and (b) R-Ag/TiO_2/*p*-Si photocathode.

For PEC measurement, the 500 nm thick patterned SiO_2 layer was deposited on TiO_2/*p*-Si substrates using a patterning mask (Figure 3.2(a)), followed by electrodeposition of Ag catalysts in the same procedure mentioned earlier. In Figure 3.2(b-c), Ag catalysts were electrodeposited only on the SiO_2-free surface of the TiO_2/*p*-Si substrate, allowing light absorption to Si through the SiO_2 portion. The high electronic potential barrier is formed at the TiO_2/SiO_2 interface due to the high band gap of SiO_2, so electrons for electrodeposition of Ag^+ ion to Ag cannot be move to the electrolyte. Therefore, Ag catalysts are only deposited on the SiO_2-free surface.

The PEC properties of the R-Ag on TiO_2/*p*-Si, Ag on TiO_2/*p*-Si, TiO_2/*p*-Si, and *p*-Si photocathodes were measured with a three-electrode system in CO_2 saturated 0.1 M $KHCO_3$ electrolytes under AM 1.5G illumination. Figure 3.7(a) displays the PEC current densities of the photocathodes plotted as a function of potential vs. RHE. The black lines indicate the dark current, which show negligible currents flows in the dark condition. As in the previous report.[43] when the onset potential means a voltage generating a photocurrent of -0.6 mA/cm^2, the *p*-Si photocathode is found to have the largest onset potential of -0.54 V vs. RHE. The TiO_2/*p*-Si photocathode has a slightly enhanced onset potential of -0.42 V vs. RHE and larger photocurrent, which is attributed to a heterojunction formed with *p*-Si and *n*-TiO_2.[44] On the other hand, the two Ag-electrodeposited photocathodes exhibit the significantly lowered onset potential, and the R-Ag/TiO_2/*p*-Si photocathode exhibits the lowest onset potential of -0.16 V vs. RHE, which is 100 mV lower than that of the Ag/TiO_2/*p*-Si photocathode. After the onset potential, the photocurrent density of the R-Ag/TiO_2/*p*-Si photocathode gradually rises with the applied

potential and is saturated to -9 mA/cm^2 at -1.23 V vs. RHE, which is superior to that of the Ag/TiO_2/*p*-Si photocathode. Compared to the *p*-Si and TiO_2/*p*-Si photocathodes, the photocurrent density of Ag catalysts electrodeposited photocathodes is reduced due to the Ag particles that inhibited the light absorption by the light absorber, but an enhancement of the catalytic activity occurs on the Ag catalysts.

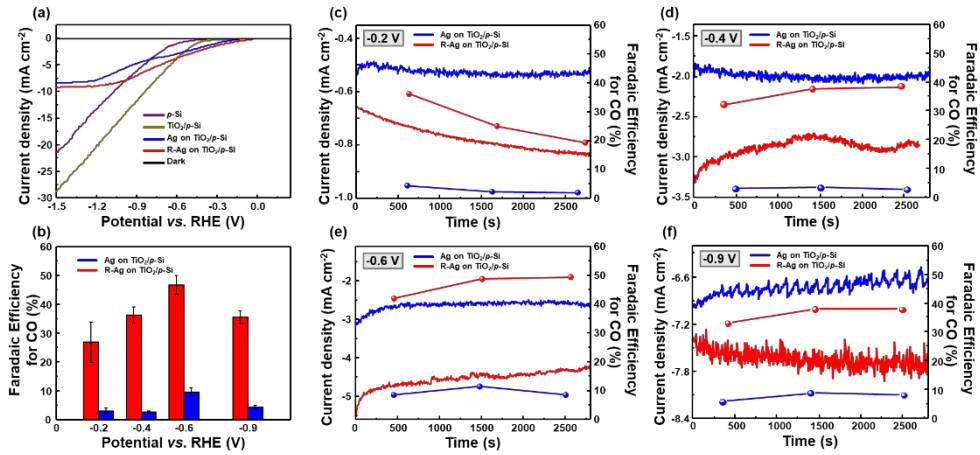

Figure 3.7. Performances of photoelectrochemical CO_2 reduction of Ag and R-Ag catalysts on SiO_2 patterned TiO_2/*p*-Si photocathodes under 1 sun illumination (AM 1.5 G) in CO_2-saturated 0.1 M $KHCO_3$ electrolytes. (a) Polarization curves and (b) Faradaic efficiency of the fabricated photocathodes. The current density (— left axis) and faradaic efficiency for CO (● right axis) vs. time on the Ag catalysts (blue) and the R-Ag catalysts (red) on SiO_2 patterned TiO_2/*p*-Si photocathodes at (c) −0.2 V, (d) −0.4 V, (e) −0.6 V, and (f) −0.9 V.

To obtain faradaic efficiency, chronoamperometric measurements were conducted at potentials between -0.4 and -0.9 V vs. RHE while gas products are analyzed three times at each potential using gas chromatography (GC). The faradaic efficiency is calculated based on the eq. (2-5) using the corresponding chronoamperometry (*i-t*) curves in Figure 3.7(c-f). The average values of calculated faradaic efficiency for CO was plotted against the potential as shown in Figure 3.7(b). The *p*-Si and TiO_2/*p*-Si photocathodes have a very low faradaic efficiency of less than 5% at all the measured potentials in Figure 3.8, because Si has poor CO_2 reduction reaction catalytic activity and TiO_2 has catalytic properties for hydrogen evolution reaction.[18, 44] Although Ag catalysts were introduced, it is confirmed that the Ag/TiO_2/*p*-Si photocathode still exhibit a low selectivity. However, with the RA treatment of Ag catalysts, the selectivity for CO is considerably improved at R-Ag/TiO_2/*p*-Si photocathode, as shown in Figure 3.7(b). At the low potential of -0.2 V vs. RHE, the R-Ag/TiO_2/*p*-Si photocathode has a faradaic efficiency of 27%. With the increasing applied potential, the CO selectivity gradually rose and reached 47% at -0.6 V vs. RHE, and decreased beyond the peak potential. Before the potential region of -0.6 V vs. RHE, the hydrogen evolution reaction is suppressed by CO adsorbed on Ag catalysts, causing the faradaic efficiency for CO to increase.[31] However, beyond the -0.6 V vs. RHE, the faradaic efficiency for CO decreased. This is because of reaching the mass transport limitation of CO_2 by the low concentration of CO_2 in the aqueous electrolyte at higher over-potential.[45] In Figure 3.7(c-f), the photocurrent density on the R-Ag/TiO_2/*p*-Si photocathode is larger than that on the Ag/TiO_2/*p*-Si photocathode over all measured potential. This is due to the enlarged active sites by

morphology changes. Furthermore, the enhancement of faradaic efficiency for CO is attributed to the increased (110) planes and lower binding energy of R-Ag catalysts as mentioned before. The undercoordinated surface atom on (110) planes and lowered binding energy of R-Ag could facilitate to stabilize the key reaction intermediate ($COOH^*$).

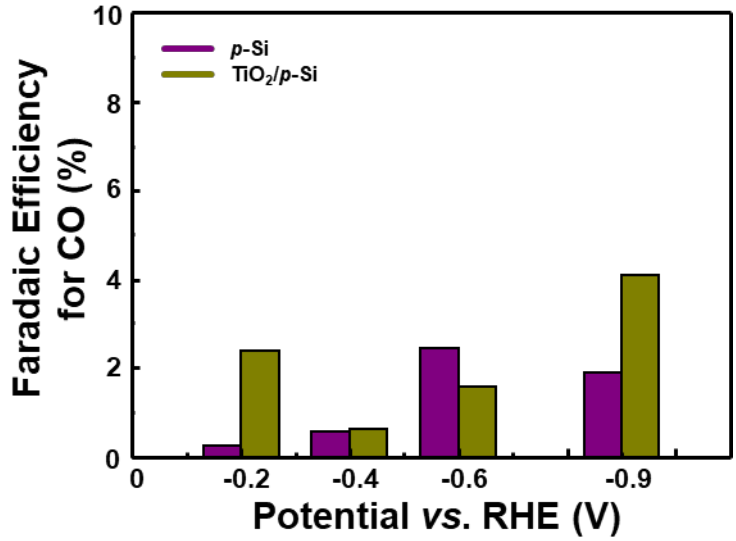

Figure 3. 8 . The faradaic efficiency of the *p*-Si and TiO_2/*p*-Si photocathodes in CO_2-saturated 0.1 M $KHCO_3$ electrolytes.

The best-performing R-Ag/TiO_2/*p*-Si photocathode can synthesis syngas with ratios from 1:3 to 1:1 depends on the applied potentials, as shown in Figure 3.9(a). At –0.4 V vs. RHE, the photocathode produces 10.1 mol/s·cm^2 of syngas at a ratio of 1:2, which is suitable feedstock for the process of methanol production.[46] Also, the syngas with a ratio of 1:1 is produced at a rate of 18.6 mol/s·cm^2 at -0.6 V vs. RHE, which can be used for the Fischer-Tropsch synthesis.[47] Furthermore, the stability test was conducted at -0.4 V vs. RHE for the R-Ag/TiO_2/*p*-Si photocathode. Figure 3.10 shows the excellent stability for the R-Ag/TiO_2/*p*-Si photocathode indicating no significant decreases in both current density and faradaic efficiency for CO.

This PEC performance for syngas production on Ag catalysts is realized by using the model proposed here. Figure 3.9(b) shows the schematic of our proposed model of photocathode for CO_2 reduction. This model, patterning SiO_2 layer and filling the remaining region with Ag catalysts using the electrodeposition method, can allow the light absorption through the SiO_2 layer and promote the CO_2 reduction reaction on Ag catalysts.

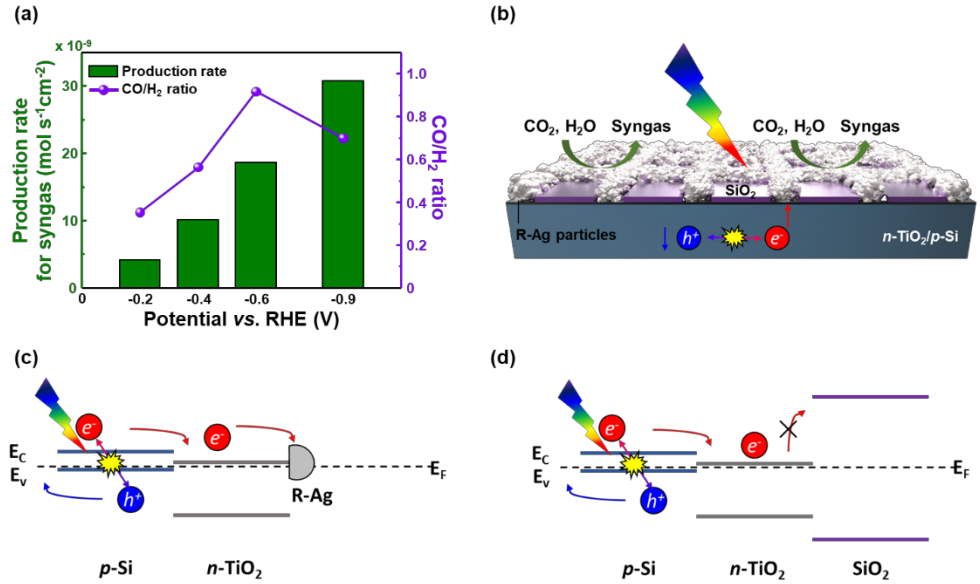

Figure 3.9. (a) Production rates for syngas and CO/H_2 ratio for photoelectrochemical CO_2 reduction on R-Ag catalysts on SiO_2 patterned TiO_2/*p*-Si photocathodes at each potential. (b) Schematic of photoelectrochemical reduction of CO_2 on R-Ag catalysts on SiO_2 patterned TiO_2/*p*-Si photocathode. Energy band diagrams of (c) R-Ag/*n*-TiO_2/*p*-Si and (d) SiO_2/*n*-TiO_2/*p*-Si photocathodes.

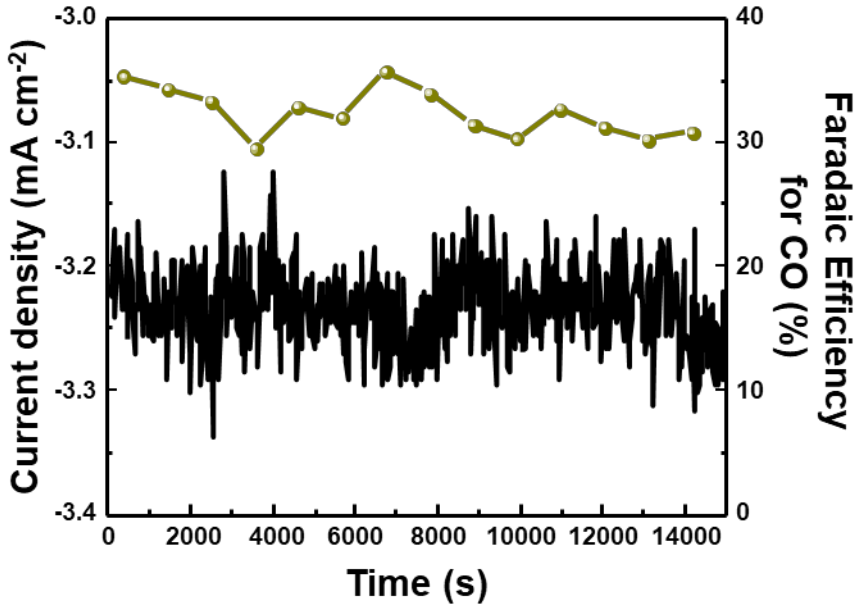

Figure 3.10. Stability test of current density and CO faradaic efficiency for R-Ag/TiO_2/*p*-Si photocathode at -0.4 V vs. RHE under 1 sun illumination (AM 1.5G) in CO_2-saturated 0.1 M $KHCO_3$ electrolytes.

This is attributed to the energy band structure of the photocathode, as shown in Figure 3.9(c-d). The band diagrams were drawn, based on the previously reported flat band diagrams (Figure 3.11).[44, 48-50] SiO_2 is an insulating materials, so has high band gap. Due to the intrinsic energy band property of SiO_2, the high electronic potential barrier is formed at the Ag/SiO_2 interface, which blocked transportation of the electrons to electrolyte for reaction. On the other hand, since Ag particles have metallic properties, the electrons are easily transferred through Ag particles to electrolyte. Therefore, the electrochemical reaction only occurs at the R-Ag catalysts, which improves the efficiency of CO_2 reduction reaction. Furthermore, this model can be adapted to other catalysts, so it can be seen as a promising model for photocathode on PEC CO_2 reduction study.

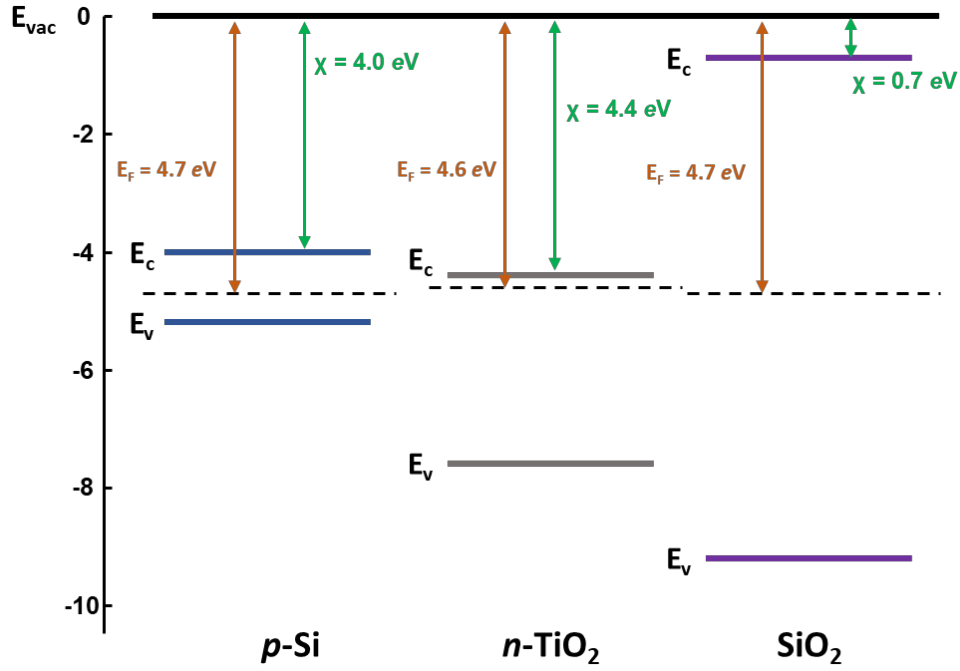

Figure 3.11. Flat band diagram of (a) *p*-Si,[44, 48] (b) *n*-TiO_2,[49, 50] and (c) SiO_2.[48]

3.4. Conclusion

In this chapter, we report for the reduced Ag catalysts on TiO_2/*p*-Si photocathodes for PEC CO_2 reduction to produce syngas. The R-Ag/TiO_2/*p*-Si photocathode has been synthesized by using the combination of electron-beam deposition method, electrodeposition, and electrochemical anodization/reduction treatment. The morphology, active sites, and electronic structure of Ag catalysts are modified by the RA treatment to achieve the high catalytic activity for the CO_2 reduction reaction. The new model using a patterned SiO_2 layer can allow the light absorption onto light absorber and facilitate the CO_2 reduction reaction on Ag catalysts. The best performing photocathode provided the lowest onset potential of -0.16 V vs. RHE, a large saturated photocurrent density of -9 mA/cm^2 at -1.23 V vs. RHE. Furthermore, the faradaic efficiency for CO of 47% was achieved at -0.6 V vs. RHE. At this potential, the photocathode could produce the syngas ratio of 1:1 with the rate in 18.6 mol/s·cm^2, which is a suitable proportion for the Fischer-Tropsch synthesis. Although this study focused on *p*-Si photocathode with Ag catalysts for PEC CO_2 reduction, our proposed new model for photocathode could be useful in various PEC applications, such as hydrogen evolution reaction, oxygen evolution reaction, or N_2 reduction reaction.

3.5. References

[1] S. J. Davis, K. Caldeira, H. D. Matthews, *Science* **2010**, *329*, 1330.

[2] D. R. Feldman, W. D. Collins, P. J. Gero, M. S. Torn, E. J. Mlawer, T. R. Shippert, *Nature* **2015**, *519*, 339.

[3] J. H. Montoya, L. C. Seitz, P. Chakthranont, A. Vojvodic, T. F. Jaramillo, J. K. Nørskov, *Nature Materials* **2017**, *16*, 70.

[4] M. G. Lee, K. Jin, K. C. Kwon, W. Sohn, H. Park, K. S. Choi, Y. K. Go, H. Seo, J. S. Hong, K. T. Nam, H. W. Jang, *Advanced Science* **2018**, *5*, 1800727.

[5] E. V. Kondratenko, G. Mul, J. Baltrusaitis, G. O. Larrazábal, J. Pérez-Ramírez, *Energy & Environmental Science* **2013**, *6*, 3112.

[6] S. Kim, W. J. Dong, S. Gim, W. Sohn, J. Y. Park, C. J. Yoo, H. W. Jang, J.-L. Lee, *Nano Energy* **2017**, *39*, 44.

[7] K. C. Kwon, J. M. Suh, R. S. Varma, M. Shokouhimehr, H. W. Jang, *Small Methods* **2019**, *3*, 1800492.

[8] P. Ding, Y. Hu, J. Deng, J. Chen, C. Zha, H. Yang, N. Han, Q. Gong, L. Li, T. Wang, *Materials Today Chemistry* **2019**, *11*, 80.

[9] Q. Kong, D. Kim, C. Liu, Y. Yu, Y. Su, Y. Li, P. Yang, *Nano Letters* **2016**, *16*, 5675.

[10] Y. Hori, H. Wakebe, T. Tsukamoto, O. Koga, *Electrochimica Acta* **1994**, *39*, 1833.

[11] Y. Chen, C. W. Li, M. W. Kanan, *Journal of the American Chemical Society* **2012**, *134*, 19969.

[12] Y. Zhang, F. Li, X. Zhang, T. Williams, C. D. Easton, A. M. Bond, J. Zhang, *Journal of Materials Chemistry A* **2018**, *6*, 4714.

[13] M. Le, M. Ren, Z. Zhang, P. T. Sprunger, R. L. Kurtz, J. C. Flake, *Journal of the Electrochemical Society* **2011**, *158*, E45.

[14] E. E. Barton, D. M. Rampulla, A. B. Bocarsly, *Journal of the American Chemical Society* **2008**, *130*, 6342.

[15] S. Choi, C. Kim, J. M. Suh, H. W. Jang, *Carbon Energy* **2019**, *1*, 85.

[16] A. Y. Khodakov, W. Chu, P. Fongarland, *Chemical reviews* **2007**, *107*, 1692.

[17] S. R. Foit, I. C. Vinke, L. G. de Haart, R. A. Eichel, *Angewandte Chemie International Edition* **2017**, *56*, 5402.

[18] J. T. Song, H. Ryoo, M. Cho, J. Kim, J. G. Kim, S. Y. Chung, J. Oh, *Advanced Energy Materials* **2017**, *7*, 1601103.

[19] H.-Y. Kang, D.-H. Nam, K. D. Yang, W. Joo, H. Kwak, H.-H. Kim, S.-H. Hong, K. T. Nam, Y.-C. Joo, *ACS Nano* **2018**, *12*, 8187.

[20] X. Yang, E. A. Fugate,Y. Mueanngern, L. R. Baker, *ACS Catalysis* **2017**, *7*, 177.

[21] J. S. DuChene, G. Tagliabue, A. J. Welch, W.-H. Cheng, H. A. Atwater, *Nano Letters* **2018**, *18*, 2545.

[22] M. Asadi, M. H. Motevaselian, A. Moradzadeh, L. Majidi, M. Esmaeilirad, T. V. Sun, C. Liu, R. Bose, P. Abbasi, P. Zapol, A. P. Khodadoust, L. A. Curtiss, N. R. Aluru, A. Salehi-Khojin, *Advanced Energy Materials* **2019**, *9*, 1803536.

[23] T. L. Kim, M.-J. Choi, T. H. Lee, W. Sohn, H. W. Jang, *Nano letters* **2019**, *19*, 5897.

[24] R. Hinogami, Y. Nakamura, S. Yae, Y. Nakato, *The Journal of Physical Chemistry B* **1998**, *102*, 974.

[25] C. Rogers, W. S. Perkins, G. Veber, T. E. Williams, R. R. Cloke, F. R. Fischer, *Journal of the American Chemical Society* **2017**, *139*, 4052.

[26] L. Zhang, Z. Wang, N. Mehio, X. Jin, S. Dai, *ChemSusChem* **2016**, *9*, 428.

[27] R. Daiyan, X. Lu, Y. H. Ng, R. Amal, *ChemistrySelect* **2017**, *2*, 879.

[28] W. Zhu, R. Michalsky, O. n. Metin, H. Lv, S. Guo, C. J. Wright, X. Sun, A. A. Peterson, S. Sun, *Journal of the American Chemical Society* **2013**, *135*, 16833.

[29] W. Zhu, Y.-J. Zhang, H. Zhang, H. Lv, Q. Li, R. Michalsky, A. A. Peterson, S. Sun, *Journal of the American Chemical Society* **2014**, *136*, 16132.

[30] C. Kim, H. S. Jeon, T. Eom, M. S. Jee, H. Kim, C. M. Friend, B. K. Min, J. Y. Hwang, *Journal of the American Chemical Society* **2015**, *137*, 13844.

[31] E. L. Clark, S. Ringe, M. Tang, A. Walton, C. Hahn, T. F. Jaramillo, K. Chan, A. T. Bell, *ACS catalysis* **2019**, *9*, 4006.

[32] Y. Chen, M. W. Kanan, *Journal of the American Chemical Society* **2012**, *134*, 1986.

[33] C. W. Li, M. W. Kanan, *Journal of the American Chemical Society* **2012**, *134*, 7231.

[34] M. S. Jee, H. Kim, H. S. Jeon, K. H. Chae, J. Cho, B. K. Min, Y. J. Hwang, *Catalysis Today* **2017**, *288*, 48.

[35] M. Ma, K. Liu, J. Shen, R. Kas, W. A. Smith, *ACS Energy Letters* **2018**, *3*, 1301.

[36] X. Peng, S. G. Karakalos, W. E. Mustain, *ACS applied Materials & Interfaces* **2018**, *10*, 1734.

[37] Y.-C. Hsieh, S. D. Senanayake, Y. Zhang, W. Xu, D. E. Polyansky, *ACS Catalysis* **2015**, *5*, 5349.

[38] W. Qiu, R. Liang, Y. Luo, G. Cui, J. Qiu, X. Sun, *Inorganic Chemistry Frontiers* **2018**, *5*, 2238.

[39] C. C. McCrory, S. Jung, J. C. Peters, T. F. Jaramillo, *Journal of the American Chemical Society* **2013**, *135*, 16977.

[40] S. Back, M .S. Yeom, Y. Jung, *ACS Catalysis* **2015**, *5*, 5089.

[41] Y. S. Ham, S. Choe, M. J. Kim, T. Lim, S.-K. Kim, J. J. Kim, *Applied Catalysis B: Environmental* **2017**, *208*, 35.

[42] J. A. Rodriguez, D. W. Goodman, *Science* **1992**, *257*, 897.

[43] W. Lu, B. Jia, B. Cui, Y. Zhang, K. Yao, Y. Zhao, J. Wang, *Angewandte Chemie International Edition* **2017**, *56*, 11851.

[44] D. M. Andoshe, S. Choi, Y.-S. Shim, S. H. Lee, Y. Kim, C. W. Moon, D. H. Kim, S. Y. Lee, T. Kim, H. K. Park, M. G. Lee, J.-M. Jeon, K. T. Nam, M. Kim, J. K. Kim, J. Oh, H. W. Jang, *Journal of Materials Chemistry A* **2016**, *4*, 9477.

[45] F. Li, L. Chen, G. P. Knowles, D. R. MacFarlane, J. Zhang, *Angewandte chemie international edition* **2017**, *56*, 505.

[46] M. Farkhondehfal, S. Hernández, M. Rattalino, M. Makkee, A. Lamberti, A. Chiodoni, K. Bejtka, A. Sacco, F. Pirri, N. Russo, *International Journal of Hydrogen Energy* **2019**, *45*, 26458.

[47] C. Li, T. Wang, B. Liu, M. Chen, A. Li, G. Zhang, M. Du, H. Wang, S. F. Liu, J. Gong, *Energy & Environmental Science* **2019**, *12*, 923.

[48] S. M. Sze, Semiconductor devices: physics and technology. John wiley & sons: 2008.

[49] D. Tashmukhamedova, M. Yusupjanova, *X-ray, Synchrotron Neutron Techniques* **2016**, *10*, 1273.

[50] D. O. Scanlon, C. W. Dunnill, J. Buckeridge, S. A. Shevlin, A. J. Logsdail, S. M. Woodley, C. R. A. Catlow, M. J. Powell, R. G. Palgrave, I. P. Parkin, G. W. Watson, T. W. Keal, P. Sherwood, A. Walsh, A. A. Sokol, A. A., *Nature Materials* **2013**, *12*, 798.

Chapter 4

Summary

In this thesis, the following strategies for improving photoelectrochemical properties in solar fuel production. Photocathodes decorated with nanostructured catalysts were fabricated using strategies suitable for solar water splitting and CO_2 conversion reactions, respectively. Each reaction has a different mechanism, requiring different strategies to apply nanocatalysts to silicon photocathodes.

In chapter 2, large scale (12 cm × 12 cm) and transferable FNS NPs decorated VMS thin film catalysts were synthesized via one-step sulfurization method. The synthesized thin film catalyst exhibited remarkable PEC performance: high photocurrent density (25.44 mA cm^{-2} at 0 V vs. RHE), lower onset potential (280 mV at 1.0 mA cm^{-2}) and long-term stability (over 10 h). The heterojunction band diagram and DFT calculation further showed that the F1N9S NPs on VMS/*p*-Si photocathode not only induced the downward band bending of VMS but also improved the surface kinetics of the thin film catalyst. The proposed one-step sulfurization method paves a novel way for TMD-based 3D/2D heterojunctions, which were previously inaccessible in the form of large-scale transferable thin films. The 3D/2D heterojunction demonstrated here with conventional transition metal disulfides could also lead to the discovery of a new class of thin film materials with a versatile combination of both transition metals and chalcogen elements.

In chapter 3, the reduced Ag catalysts on TiO_2/*p*-Si photocathodes for PEC CO_2

reduction to produce syngas were demonstrated. The R-Ag/TiO_2/*p*-Si photocathode has been synthesized by using the combination of electron-beam deposition method, electrodeposition, and electrochemical anodization/reduction treatment. The morphology, active sites, and electronic structure of Ag catalysts are modified by the RA treatment to achieve the high catalytic activity for the CO_2 reduction reaction. The new model using a patterned SiO_2 layer can allow the light absorption onto light absorber and facilitate the CO_2 reduction reaction on Ag catalysts. The best performing photocathode provided the lowest onset potential of -0.16 V vs. RHE, a large saturated photocurrent density of -9 mA/cm^2 at -1.23 V vs. RHE. Furthermore, the faradaic efficiency for CO of 47% was achieved at -0.6 V vs. RHE. At this potential, the photocathode could produce the syngas ratio of 1:1 with the rate in 18.6 mol/s·cm^2, which is a suitable proportion for the Fischer-Tropsch synthesis. Although this study focused on *p*-Si photocathode with Ag catalysts for PEC CO_2 reduction, our proposed new model for photocathode could be useful in various PEC applications, such as hydrogen evolution reaction, oxygen evolution reaction, or N_2 reduction reaction.

List of Publications

[1] Kwon, Ki Chang, Seokhoon Choi, Kootak Hong, Dinsefa Mensur Andoshe, Jun Min Suh, **Changyeon Kim**, Kyoung Soon Choi, Jeong Hyeon Oh, Soo Young Kim, and Ho Won Jang. "Tungsten disulfide thin film/p-type Si heterojunction photocathode for efficient photochemical hydrogen production." *MRS Communications* 7, no. 2 (2017): 272-279.

[2] Andoshe, Dinsefa Mensur†, Gangtae Jin†, Chang-Soo Lee†, **Changyeon Kim**†, Ki Chang Kwon, Seokhoon Choi, Woonbae Sohn et al. "Directly assembled 3D molybdenum disulfide on silicon wafer for efficient photoelectrochemical water reduction." *Advanced Sustainable Systems* 2, no. 3 (2018): 1700142.

[3] Bhat, Swetha SM, Jun Min Suh, Seokhoon Choi, Seung-Pyo Hong, Sol A. Lee, **Changyeon Kim**, Cheon Woo Moon, Mi Gyoung Lee, and Ho Won Jang. "Substantially enhanced front illumination photocurrent in porous SnO 2 nanorods/networked BiVO 4 heterojunction photoanodes." *Journal of Materials Chemistry A* 6, no. 30 (2018): 14633-14643.

[4] Andoshe, Dinsefa M., Kanghoon Yim, Woonbae Sohn, **Changyeon Kim**, Taemin Ludvic Kim, Ki Chang Kwon, Kootak Hong et al. "One-pot synthesis of sulfur and nitrogen codoped titanium dioxide nanorod arrays for superior photoelectrochemical water oxidation." *Applied Catalysis B: Environmental* 234 (2018): 213-222.

[5] Lee, Sol A., Tae Hyung Lee, **Changyeon Kim**, Mi Gyoung Lee, Min-Ju Choi, Hoonkee Park, Seokhoon Choi, Jihun Oh, and Ho Won Jang. "Tailored NiO x/Ni cocatalysts on silicon for highly efficient water splitting photoanodes via pulsed electrodeposition." *ACS Catalysis* 8, no. 8 (2018): 7261-7269.

[6] Choi, Seokhoon†, **Changyeon Kim**†, Jun Min Suh, and Ho Won Jang.

"Reduced graphene oxide-based materials for electrochemical energy conversion reactions." *Carbon Energy* 1, no. 1 (2019): 85-108.

[7] Lee, Bo Reum, Mi Gyoung Lee, Hoonkee Park, Tae Hyung Lee, Sol A. Lee, Swetha SM Bhat, **Changyeon Kim**, Sanghan Lee, and Ho Won Jang. "All-Solution-Processed WO3/BiVO4 Core–Shell Nanorod Arrays for Highly Stable Photoanodes." *ACS applied materials & interfaces* 11, no. 22 (2019): 20004-20012.

[8] Lee, Yubin, Seungkyu Kim, Sang Yun Jeong, Sehun Seo, **Changyeon Kim**, Hongji Yoon, Ho Won Jang, and Sanghan Lee. "Surface-modified co-doped ZnO photoanode for photoelectrochemical oxidation of glycerol." *Catalysis Today* (2019).

[9] Bhat, Swetha SM, Sachin A. Pawar, Darshna Potphode, Chang-Ki Moon, Jun Min Suh, **Changyeon Kim**, Seokhoon Choi et al. "Substantially enhanced photoelectrochemical performance of TiO2 nanorods/CdS nanocrystals heterojunction photoanode decorated with MoS2 nanosheets." *Applied Catalysis B: Environmental* 259 (2019): 118102.

[10] Park, Hoonkee, Ik Jae Park, Mi Gyoung Lee, Ki Chang Kwon, Seung-Pyo Hong, Do Hong Kim, Sol A. Lee et al. "Water splitting exceeding 17% solar-to-hydrogen conversion efficiency using solution-processed Ni-based electrocatalysts and perovskite/Si tandem solar cell." *ACS applied materials & interfaces* 11, no. 37 (2019): 33835-33843.

[11] Kim, Yeonhoo, Ki Chang Kwon, Sungwoo Kang, **Changyeon Kim**, Tae Hoon Kim, Seung-Pyo Hong, Seo Yun Park et al. "Two-dimensional NbS2 gas sensors for selective and reversible NO2 detection at room temperature." *ACS sensors* 4, no. 9 (2019): 2395-2402.

[12] Lee, Sol A., Seokhoon Choi, **Changyeon Kim**, Jin Wook Yang, Soo Young Kim, and Ho Won Jang. "Si-Based water oxidation photoanodes conjugated with earth-abundant transition metal-based catalysts." *ACS Materials*

Letters 2, no. 1 (2019): 107-126.

[13] Lee, Sol A., Tae Hyung Lee, **Changyeon Kim**, Min-Ju Choi, Hoonkee Park, Seokhoon Choi, Jinwoo Lee, Jihun Oh, Soo Young Kim, and Ho Won Jang. "Amorphous cobalt oxide nanowalls as catalyst and protection layers on n-type silicon for efficient photoelectrochemical water oxidation." *ACS Catalysis* 10, no. 1 (2019): 420-429.

[14] Bhat, Swetha SM, Sol A. Lee, Tae Hyung Lee, **Changyeon Kim**, Jinwoo Park, Tae-Woo Lee, Soo Young Kim, and Ho Won Jang. "All-Solution-Processed BiVO4/TiO2 Photoanode with NiCo2O4 Nanofiber Cocatalyst for Enhanced Solar Water Oxidation." *ACS Applied Energy Materials* 3, no. 6 (2020): 5646-5656.

[15] Choi, Seokhoon, Jeongwoo Hwang, Tae Hyung Lee, Hyung-Ho Kim, Seung-Pyo Hong, **Changyeon Kim**, Min-Ju Choi et al. "Photoelectrochemical hydrogen production at neutral pH phosphate buffer solution using TiO2 passivated InAs Nanowire/p-Si heterostructure photocathode." *Chemical Engineering Journal* 392 (2020): 123688.

[16] Lee, Sol A., Ik Jae Park, Jin Wook Yang, Jaemin Park, Tae Hyung Lee, **Changyeon Kim**, Jooho Moon, Jin Young Kim, and Ho Won Jang. "Electrodeposited Heterogeneous Nickel-Based Catalysts on Silicon for Efficient Sunlight-Assisted Water Splitting." *Cell Reports Physical Science* 1, no. 10 (2020): 100219.

[17] Choi, Min-Ju, Taemin Ludvic Kim, Jeong Kyu Kim, Tae Hyung Lee, Sol A. Lee, **Changyeon Kim**, Kootak Hong, Chung Wung Bark, Kyung-Tae Ko, and Ho Won Jang. "Enhanced Oxygen Evolution Electrocatalysis in Strained A-Site Cation Deficient LaNiO3 Perovskite Thin Films." *Nano Letters* 20, no. 11 (2020): 8040-8045.

[18] **Kim, Changyeon**, Seokhoon Choi, Min-Ju Choi, Sol A. Lee, Sang Hyun Ahn, Soo Young Kim, and Ho Won Jang. "Photoelectrochemical Reduction

of CO2 to Syngas by Reduced Ag Catalysts on Si Photocathodes." *Applied Sciences* 10, no. 10 (2020): 3487.

[19] Choi, Seokhoon†, **Changyeon Kim**†, Jae Yoon Lee†, Tae Hyung Lee, Ki Chang Kwon, Sungwoo Kang, Sol A. Lee et al. "Vertically aligned MoS2 thin film catalysts with Fe-Ni sulfide nanoparticles by one-step sulfurization for efficient solar water reduction." *Chemical Engineering Journal* 418 (2021): 129369.

[20] Yoon, Ji-Won†, Jae-Hyeok Kim†, **Changyeon Kim**†, Ho Won Jang, and Jong-Heun Lee. "MOF-Based Hybrids for Solar Fuel Production." *Advanced Energy Materials*: 2003052.

[21] Bera, Susanta, Sol A. Lee, Woo-Jae Lee, Ji-Hee Kim, **Changyeon Kim**, Hyun Gu Kim, Hasmat Khan, Sunirmal Jana, Ho Won Jang, and Se-Hun Kwon. "Hierarchical Nanoporous BiVO4 Photoanodes with High Charge Separation and Transport Efficiency for Water Oxidation." *ACS Applied Materials & Interfaces* 13, no. 12 (2021): 14291-14301.

[22] Yang, Jin Wook, Ik Jae Park, Sol A. Lee, Mi Gyoung Lee, Tae Hyung Lee, Hoonkee Park, **Changyeon Kim**, Jaemin Park, Jooho Moon, Jin Young Kim, Ho Won Jang. "Near-complete charge separation in tailored BiVO4-based heterostructure photoanodes toward artificial leaf." *Applied Catalysis B: Environmental* 293 (2021): 120217.

[23] Jun, Sang Eon, Seokhoon Choi, Shinyoung Choi, Tae Hyung Lee, **Changyeon Kim**, Jin Wook Yang, Woon-Oh Choe, In-Hyuk Im, Cheol-Joo Kim, and Ho Won Jang. "Direct Synthesis of Molybdenum Phosphide Nanorods on Silicon Using Graphene at the Heterointerface for Efficient Photoelectrochemical Water Reduction." *Nano-Micro Letters* 13, no. 1 (2021): 1-16.

[24] Park, Jongseong, Tae Hyung Lee, **Changyeon Kim**, Sol A. Lee, Min-Ju Choi, Hwiho Kim, Jin Wook Yang, Jongwoo Lim, and Ho Won Jang.

"Hydrothermally obtained type-II heterojunction nanostructures of In2S3/TiO2 for remarkably enhanced photoelectrochemical water splitting." *Applied Catalysis B: Environmental* 295 (2021): 120276.

[25] Suh, Jun Min, Ki Chang Kwon, Tae Hyung Lee, **Changyeon Kim**, Chung Won Lee, Young Geun Song, Min-Ju Choi et al. "Edge-exposed WS2 on 1D nanostructures for highly selective NO2 sensor at room temperature." *Sensors and Actuators B: Chemical* 333 (2021): 129566.

국문 초록

전 세계적으로 에너지 소비가 증가함에 따라 과도한 화석 연료 사용으로 인한 기후 변화, 해수의 산성화 등 다양한 환경 문제가 제기되고 있다. 이러한 화석 연료 기반 에너지 사회에서 친환경 에너지 사회로의 전환이 필수적인 상황에서, 재생 가능하고 지속 가능한 에너지 생산 기술의 개발은 오늘날 가장 시급한 과제이다. 이런 관점에서, 무궁무진한 태양 에너지를 화학에너지로 전환시키는 태양 연료 생산은 친환경 에너지 사회로의 전환에 가장 유망한 후보 에너지원으로 알려져 있다. 태양 에너지를 이용하여 물을 분해해 수소 연료를 생산하거나, 이산화탄소를 탄소기반 연료로 전환 시키는 태양 연료 생산 기술은 많은 관심을 받고 있다. 이 과정은 반도체 재료로 이루어진 광전극에서 광전기화학적 반응을 통해 발생하기 때문에, 태양 연료 생산의 효율을 높이고자 광전극에 대한 많은 연구가 진행되고 있다. 다양한 반도체 후보 물질 중, 실리콘은 좁은 밴드갭을 갖고 있어 넓은 스펙트럼의 태양 에너지를 흡수할 수 있고, 긴 전하 확산 거리를 가지며, 지구 상에 풍부한 원소로써, 태양 에너지 활용에 유리하기 때문에 광전극 물질로 유망하다고 알려져 있다. 하지만 실리콘은 광전기화학 반응에 대한 열악한 키네틱 및 촉매 활성과, 광전기화학적 시스템에서 전해질과 접촉 시에 안정성이 떨어진다는 몇 가지 한계점이 있다. 효율적인 태양 연료 생산을 위해서는 이러한 한계가 개선된 실리콘 광전극을 제작하는 것이

필수적이다.

본 논문에서는 태양 연료 생산을 위한 광전극에 실리콘을 활용하기 위한 다양한 공학 전략을 적용한 연구에 대한 이야기를 다룬다. 태양 연료 생산 방법인, 수소 연료 생산을 위한 태양광 물 분해 및 탄소 기반 연료 생산을 위한 이산화탄소 전환을 위해 각 반응에 적합한 나노 구조 촉매를 이용한 공학 전략을 적용시켜 실리콘 광전극을 제작하고 연구하였다. 효율적인 광전극을 설계하려면 광전기화학 반응의 원리를 이해하는 것이 중요하기 때문에, 먼저, 태양광 물 분해 및 이산화탄소 전환에 대한 원리가 2장에서 설명된다.

3장에서는 태양광 물 분해를 위한 3차원/2차원 나노 구조 전이금속 황화물 촉매가 적용된 실리콘 광음극이 소개된다. 나노 구조를 갖는 전이금속 황화물은 높은 표면적 대 부피 비율과 촉매 활성이 높은 엣지 부위가 많이 노출되기 때문에 수소 발생 반응 촉매로 연구되고 있다. 그중 MoS_2는 뛰어난 촉매 특성으로 인해 특히 많이 연구되고 있다. 본 연구에서는 MoS2의 촉매 활성이 높은 엣지 부위 노출을 극대화하기 위해, MoS2 층이 수직 배향된 MoS2 박막 촉매를 합성하였다. 또한, 제일 원리 계산을 통해 Ni-Fe 황화물이 촉매 활성이 높다는 것을 알아내어, 이 Ni-Fe 황화물 3차원 나노입자를 수직 배향된 MoS2 박막에 장식하였다. 화학 기상 증착법을 사용하여 전사 가능한 박막 촉매를 합성하였고, 이를 실리콘 광음극에 전사하여 광전기화학적 수소 발생

반응 특성을 측정하였다. 제작된 광전극은 높은 광전류 밀도(0 V에서 25.44 mA/cm^2)와 낮은 개시 전위(280 mV) 및 10시간의 장기 안정성을 갖는 높은 특성을 나타냈다. 이 높은 광전기화학적 특성은 Ni-Fe 황화물 나노 입자 도입에 따라 반도체 내부의 밴드가 반응에 유리하게 휘어지기 때문임을 분광 분석을 통해 밝혀냈다. 이는 전하 수송을 촉진하고 전해질 계면에서 전하가 축적되는 것을 억제하는 효과를 나타냈다. 이 연구는 다양한 광전기화학적 에너지 변환 공정에서 전이금속 황화물 기반 촉매를 개발하는 데에 유망한 전략을 제시한다.

4장에서는 이산화탄소 전환을 위한 3차원 나노 구조를 갖는 은 촉매가 적용된 실리콘 광음극이 소개된다. 이산화탄소 환원 반응은 원하는 생성물로의 반응을 선택적으로 이끌어내는 촉매를 제작하는 것이 필수적이다. 전기화학적 이산화탄소 환원 반응을 위한 전기 촉매에 대한 대부분의 연구는 금속 촉매에 초점을 맞추고 있는데, 다양한 금속 촉매 중, 은은 이산화탄소를 선택적으로 일산화탄소로 환원시킬 수 있다고 알려져 있다. 본 연구에서는 합성 가스를 생산하기 위해, 일산화탄소 선택적인 은 촉매의 특성을 극대화하고자 나노 구조화 전략을 수행하였다. 전기화학적 산화-환원 공정을 통해 입자 형태의 은 촉매를 형상, 활성 부위 및 전자 구조가 조정된 나노 구조 은 촉매로 변환하였다. 하지만, 이 은 촉매를 실리콘 광음극에 장식하게 되면, 실리콘 광음극의 빛 흡수를 막게 되기 때문에 적절한 광전극 구조를 설계하는 것이 필요하다. 이를 위하여 SiO2 층을 패터닝한 새로운

실리콘 광전극 제작 전략을 제시하였고, 이를 이용하여 합성된 은 촉매가 장식된 실리콘 광전극은 낮은 개시 전위(-0.16 V vs. RHE) 및 높은 광전류 밀도(-9 mA/cm^2)를 나타냈다. 그리고 이 광음극은 작용 전압에 따라 1:1부터 1:3의 다양한 비율을 갖는 합성 가스 생산이 가능하였다. 이 연구에서 제시된 전략은 광전기화학적 반응을 향상시키기 위한 금속-반도체 광전극 설계에 새로운 접근 방식을 제시하였다.

학번: 2016-23688

김 창 연